Evaluating the Behaviour of Rock Discontinuities in Direct Shear Under Constant Normal Load and Constant Normal Stiffness Boundary Conditions Using Additive Manufacturing Technology

by

Marzieh Salami

A thesis submitted in partial fulfillment of the requirements for the degree of

Doctor of Philosophy

in

Geotechnical Engineering

Department of Civil and Environmental Engineering
University of Alberta

© Marzieh Salami, 2021

Abstract

The inherent heterogeneity of natural rock and the variance in the surface roughness of discontinuities limit the repeatability of rock joint sampling and testing. One way to overcome this challenge is by using additive manufacturing (AM) techniques. AM, also referred to as 3D printing, has shown promise in producing complex geometries rapidly, however its use in geo-sciences is preliminary. Specifically, the rock prototypes fabricated with sand-powder material have shown low compressive strength. Through this research program the feasibility of using 3D printing to replicate rocks and to investigate the shear behaviour of rock discontinuities was explored. The settings that effected the print properties were studied and higher compressive strength of rock analogues were achieved. Single asperity joints and standard roughness profiles were fabricated with a sand 3D printer and tested in direct shear under constant normal load (CNL) boundary conditions. It was concluded that it is feasible to use 3D printing to produce rock replicas and joint analogues for direct shear testing.

Discontinuities affect the mechanical and hydraulic properties of rock mass and thus understanding their behaviour better informs design schemes in geotechnical engineering projects. Surface roughness is one of the complex features of rock joints that causes dilation and contributes to its shear resistance and therefore needs to be properly assessed. Furthermore, boundary conditions influence the resistance of rock joints to shear. While previous studies have typically focused on constant normal load (CNL) conditions where there is no constraint on joint dilation such as rock slopes, however these conditions do not appropriately capture the behaviour of discontinuities in rock blocks in tunnels, reinforced rock slopes and underground CO_2 sequestration sites. In these situations, constant normal stiffness (CNS) boundary conditions are prevalent. Thus, the influence of fracture geometry on the shear behaviour of joints in both boundary conditions needs to be investigated further.

Using 3D printing, the geometrical components that contribute to fracture surface anisotropy and therefore effect shear strength and deformation of discontinuities were studied. This was done with a focus on two methods that are frequently adopted to quantify surface roughness, i.e., statistical parameters and the joint roughness coefficient (JRC). First, a set of 7 triangular profiles differed from one-another in shape, height and directionality of joint asperities were selected. Then Barton's standard joint profiles with JRC=6-8 and JRC=18-20 were divided into 5 and 10 segments and rearranged to create 9 new geometry configurations. All the joints were printed and tested in direct shear under CNL and CNS conditions. For triangular joints, it was demonstrated that based solely on one statistical parameter, a clear correlation between that parameter and peak shear strength didn't exist. It was concluded that even though statistical parameters are good indicators for defining the anisotropy in roughness of the profiles, they are not adequate. Other factors such as contact area and edge effects that results in local stress concentrations should be considered. For the new configured JRC profiles, it was revealed that when the profile with JRC=18-20 was rearranged, the new profiles had more significant difference in terms of geometric properties compared with the original profile and thus their shear response, especially in CNS conditions differed from the original joint. However, for profiles with JRC=6-8, the shear response of the new joint configurations was close to the original joint. Consequently, the empirical method of JRC may be adequate for determining the joint roughness of smoother joints, however for rougher joints, other factors such as distribution of stress on the asperities are essential and should be considered.

Lastly, through discrete element method (DEM) modelling, synthetic rock specimens were generated. Three 3D printed joint profiles with standard JRC values were simulated numerically and tested in direct shear under various applied normal stresses. The simulations captured the trend of the shear behavior of laboratory tests, however there were some discrepancies that were

attributed to the calibration of the intact material, direct shear setup, and implementation of smooth-joints contacts.

To my family. Thank you for everything.

Acknowledgments

First and foremost, I would like to thank my supervisor, Dr. Rick Chalaturnyk, for his guidance and encouragement during the many ups and downs of working on this research. Without his support, this thesis would not be possible.

Also, I would like to thank Dr. Derek Martin for his valuable suggestions and advice. I would like to acknowledge my committee members, Dr. Nicholas Beier, Dr. F. Albert Liu, Dr. Wei Victor Liu and Dr. Giovanni Grasselli from the University of Toronto, for reviewing my research and giving valuable insights and recommendations.

During my time, I was fortunate to engage in many conversations and receive research assistance from many bright minds across the globe. In particular, I am grateful to the Itasca IEP Research Program and Dr. Jim Hazzard for his time and support, to Dr. Navid Bahrani and Dr. Mojtaba Bahaaddini.

Further I would like to thank the RG², especially the GeoREF and GeoPRINT research groups and their technical staff, particularly Gilbert Wong, Keivan Khaleghi and Jakob Brandl for their support. In addition, Victor Zhao and Les Dean are acknowledged. Without their assistance, the laboratory testing could not be accomplished.

A special thanks is due to Dr. Nathan Deisman and to Hope Walls, for their ongoing support in all aspects, from technical to non-technical matters and everything in between.

To my parents and sisters, your support, understanding and love kept me going. Thank you for your presence, comfort and care.

Last, and most important, I would like to thank my love, Mehdi, for taking every step of this journey alongside me. We are the lucky ones, and I am grateful. Forever.

Contents

List of Figures

List of Tables

1 Introduction

1.1 Problem statement

Rock mass is constituted of intact rock and discontinuities. Discontinuities include bedding planes, cleavage, foliation, faults, joints, etc. They form planes of weaknesses and their presence greatly influences the mechanical and hydraulic behaviours of rock mass. Thus, a clear understanding of the properties and behaviour of discontinuities is imperative in understanding the behavior of rock mass and optimizing design schemes to control stability, deformation and fluid flow in geotechnical and reservoir geomechanics engineering projects.

To study the behaviour of rock mass experimentally, obtaining identical specimens of the intact rock or of the discontinuities is required, however because of the inherent heterogeneity of geological formations, this task becomes very difficult. For natural rock joint specimens there is variability in grain size and shape, grain minerology, joint wall strength and boundary conditions (Tatone, 2009). Further, often geomechanical and hydraulic behaviour of rock mass is complex, and simplification is needed to understand a single phenomenon. For example, to comprehend the contribution of joint roughness to dilation and shear strength, initially simple geometry such as saw-tooth joints are investigated. To overcome these challenges, researchers have conventionally created replicas of rocks and discontinuities using molds and rock-like material such as cement-based mortar (e.g., Benmokrane and Ballivy, 1989, Asadi et al., 2013, Li et al., 2016b). However, there are disadvantages with creating replicas using this method which include limitations in the number of molds produced, the arduous task of removing entrapped air bubbles from the mortar and excessive curing times. Recent advances in additive manufacturing (AM) technologies, which is also referred to as 3D printing has allowed for on-demand production and flexibility in building techniques (Gao et al., 2015). Specifically, in geotechnical and

geomechanical fields, the ability to replicate complex geometries of rock structures rapidly, is appealing. Several researchers have explored the use of AM in rock mechanics by either fabricating molds or replicating rock structures directly. The raw material adopted were polylactic acid (PLA) filaments (e.g., Jiang and Zhao, 2015, Jiang et al., 2016), powder-based material such as sand, ceramics and gypsum (e.g., Jiang et al., 2016, Zhou and Zhu, 2018, Perras and Vogler, 2019) and resin (e.g., Zhu et al., 2018). For specimens fabricated with powder-based material, even though the general stress-strain behaviour was similar to rock analogues, however, the compressive strength values were generally low (e.g., Jiang et al., 2016, Zhou and Zhu, 2018, Perras and Vogler, 2019). Further, there have been less focus on using AM technology in studying the shear behaviour of rock joints.

The shear strength, deformation and fluid flow properties of discontinuities has been the subject of research for several decades (e.g., Barton, 1973, Archambault et al., 1997, Grasselli and Egger, 2003, Li et al., 2017, among others). This is indicative of the significance of discontinuity behaviour in the field of rock mechanics, while revealing its complex nature. Surface roughness is one aspect of discontinuities which is responsible for such complexity. Roughness generates dilation and is an important factor in joint shear resistance, thus should be properly assessed and quantified. Empirical, statistical and fractal methods are used to quantify joint roughness (Tatone, 2009). Barton and Choubey (1977) proposed a parameter called the joint roughness coefficient (JRC) to classify joint roughness and to be used in their shear strength criterion and because the Barton-Bandis shear criterion (Barton, 1973, Barton and Bandis, 1990) is so widely used, the JRC quantification method is important. However, the shortcoming of JRC quantification method is that it is subjective (Beer et al., 2002) and requires further assessment.

Moreover, most experimental studies on the shear behaviour of joints are undertaken in constant normal load (CNL) boundary conditions where the normal load acting on the joint surface is constant and there is no constraint on its dilation. This is because of easier experimental

setup and conduct (Li et al., 2018). However, in field conditions such as rock blocks in tunnels, reinforced rock slopes and underground CO_2 sequestration sites, constant normal stiffness (CNS) boundary conditions are prominent (e.g., Jiang et al., 2006, Indraratna et al., 2015). Nonetheless the number of studies that have evaluated direct shear tests under CNS conditions is limited and this area has received lesser attention. Furthermore, although there have been many studies recognizing the importance of joint geometry, the influence of fracture geometry on the shear behaviour of joints in CNS boundary conditions requires more investigation.

Lastly, numerical modeling of shear behaviour of rock joints has shown promise to override the difficulties of experimental and analytical approaches, however the quality of results depends largely on the computer program and still requires considerable improvement (Li et al., 2016a). Discrete element method (DEM) models such as PFC are capable of explicitly simulating crack nucleation, propagation and asperity damage. Although many numerical studies investigating the shear strength and deformation of rock joints have been carried out, and some show that these programs have the capacity to capture discontinuity behaviour qualitatively (Bayona et al., 2018), more research is needed to decrease the discrepancy between measured and modeled results. Therefore, a more comprehensive investigation of the shear response of rock joints is granted.

1.2 Research objectives and hypothesis

The principal objective of this research program is to investigate the use of additive manufacturing technology in enhancing the understanding of the effect of joint geometry components on the shear behaviour of rock discontinuities under boundary conditions that correctly resemble field conditions. To obtain this goal, the specific research objectives are as follows:

- Investigate the feasibility of additive manufacturing in replicating rock analogues and enhance the properties of 3D printed rock proxies to obtain higher compressive strengths.

- Investigate specifically the ability of AM technology in producing fracture surface geometry and explore their performance in direct shear.
- Examine which components of joint geometry are important in defining surface roughness and therefore effect the shear behaviour of rock joints under CNL and CNS boundary conditions in direct shear tests using 3D printed sand proxies. In particular, analyze the effectiveness of statistical methods and empirical method (JRC) in quantifying surface roughness anisotropy.
- Further the knowledge of the discrepancies that exist between the shear stress-shear displacement and normal displacement-shear displacement response of rock joint profiles in a DEM numerical model and measured results. The knowledge gained from this section can then be used in models where the micro-parameters of the intact material are inserted directly from the 3D printed material properties to obtain the macro behaviour of the rock analogues, and thus resulting in better match between simulations and lab results.

To obtain these purposes, it is hypothesized that AM technology, specifically the binder jetting process, is able to produce fracture surface geometry that could be used to investigate the shear strength and deformation response of these discontinuities in CNL and CNS boundary conditions.

This is to say that geometrical components of surface roughness and the existing boundary conditions greatly influence the peak shear strength and dilation of rock discontinuities and this will be demonstrated using 3D printed sand proxies.

1.3 Methodology and scope

The scope of this research is 1) to investigate the capability of additive manufacturing technology using the binder jetting process to replicate rock proxies and fracture geometry; 2)

examine the effect of joint geometry components on the shear behaviour of joints in prevalent boundary conditions.

To satisfy the research objectives, a laboratory and numerical approach is adopted. For the laboratory section, a 3D printer capable of printing sand proxies is used. The settings of the 3D printer are altered, and post-processing techniques are tested to enhance the properties of the fabricated samples. UCS and Brazilian tests are carried out to obtain the strength and deformation properties of the printed sand proxies. Briefly, the fused deposition modeling (FDM) process for printing molds to replicate joint geometries is explored.

To observe the feasibility of the AM technology to replicate natural rock joints, single-asperity and standard JRC joints are chosen and their geometries are constructed using a CAD software. The samples are 3D printed and tested in direct shear under CNL conditions. Moreover, the GCTS direct shear machine was modified to incorporate CNS boundary conditions. To investigate the effect of fracture roughness components on shear behaviour of joints, several triangular joints, also new configured joint geometries based on the rotation of standard JRC profiles were designed, 3D printed and tested in direct shear in CNL and CNS conditions.

Of note is that the experiments are conducted on samples with width of approximately 10 cm, and larger discontinuities and scale is not studied as part of this research program. Also, the upper and lower joint surfaces are mated. Mismatch and mechanical aperture between the joint surfaces is not part of the scope of this thesis.

Finally, the discrete element method (DEM) incorporated in the commercially available PFC software, which can simulate the interaction of discrete bodies with rough and intricate surfaces, is used to generate the synthetic rock specimen and simulate the stress-deformation response of the printed sand samples. The simulations are carried out for three standard geometries and in two dimensions, and thus, the influence of out-of-plane heterogeneities is not considered. Also,

for this research program, for the numerical simulations, only CNL conditions are studied. The aim is to understand the shortcomings of the simulation process for modelling different geometries and understanding the underlying mechanisms at work. It is postulated that the knowledge gained from these simulations can contribute to recognizing the gap between laboratory and simulations and then be used for models where the micro-parameters of the 3D prints are inserted directly from parameters measured in the laboratory and in more complex environments such as CNS boundary conditions.

1.4 Thesis organization

This thesis consists of 6 chapters. *Chapter 1* states the objectives, hypothesis, scope and approach applied to obtain the goals of the research. *Chapter 2* gives a background on the state of AM technology in rock mechanics, methods used to quantify surface roughness in fractures and research done in CNS boundary conditions. Numerical investigations using DEM on rock discontinuities in direct shear is also reviewed. In *chapter 3*, the binder jetting process to fabricate 3D printed rock proxies is explained and the different print configurations and curing techniques are explored. The results of the strength tests used to define the properties of the printed specimens are given and the fabricated samples are compared to natural rock. Some additional post-processing techniques to enhance the properties of the printed samples are discussed. Then, rock joints with simple geometry are printed and tested in direct shear to evaluate the feasibility of replicating rock joints with the 3D sand printer. For completeness, briefly, the fused deposition modeling (FDM) technique to fabricate molds and to cast rock joints using conventional material is reviewed. Following chapter 3, in *chapter 4*, the effect of joint roughness components on direct shear behaviour is explored by testing 7 triangular joints along with the new geometries that were created by rotating two standard JRC profiles. The direct shear apparatus was modified, and tests were carried out in CNL and CNS conditions. In *chapter 5*, the results of direct shear tests

simulated with PFC on three standard profiles in CNL conditions are presented and discussed. At last, in *chapter 6*, conclusions and recommendations for future research are provided.

2 Background

2.1 Introduction

In this research the use of additive manufacturing technology in creating rock analogues to observe the role of geometry on the shear behavior of joints in constant normal load (CNL) and constant normal stress (CNS) boundary conditions is investigated. The stress–displacement curves are then analyzed using a discrete element method (DEM). In this chapter, an overview of these segments and the investigations done by previous researchers are presented.

2.2 Additive Manufacturing

Additive manufacturing (AM) also referred to as 3D printing is becoming more widespread in public, industry and research. Most AM processes include constructing a 3D object based on a digital CAD file in layers; however, this process can be layerless (Chen et al., 2011). The advantages of AM compared to conventional manufacturing techniques include flexibility and low cost in complex geometry design, dimensional accuracy, no need for assembly of parts, on-demand production and the reduction in wasted material (Gao et al., 2015). Although, in general, 3D printing is feasible where volume of production is low, geometries have complex design and the specimens are small in size (Berman, 2012).

The AM processes include material extrusion, powder bed fusion, binder jetting, material jetting, directed energy deposition, sheet lamination and vat photopolymerization (ASTM F2792 - 12a, 2012). Material extrusion is a process where material is dispensed through a nozzle and binder jetting is a technique where a liquid agent is deposited to join powder materials. In this thesis these two methods are used. Descriptions for other methods can be found elsewhere (ASTM

F2792 - 12a, 2012). Binder jetting was first invented in MIT and has been used with materials such as metal, ceramic, sand and polymers (Gao et al., 2015).

The attractiveness of AM in soil, rock mechanics and reservoir geomechanics is the ability to construct complex geometry replicas rapidly as opposed to traditional fabrication methods. Incorporating additive manufacturing in these fields is new but steadily gaining traction. Jiang and Zhao (2015) explored the use of fused deposition modeling (FDM) process in rock mechanics. They printed cylindrical samples for UCS tests, specimens for direct tensile tests, specimens with different microstructures, a lattice model and a rock from a CT image. They concluded that the parts printed with polylactic acid (PLA) filaments mostly demonstrated plastic behavior and were not suitable for replicating rock, however the AM technology could be useful using other techniques and material. In another study, Jiang et al. (2016) examined the use of 3D printers in creating rock and joint replicas. They incorporated two types of 3D printers: 1) FDM printers with biodegradable PLA as raw material and 2) powder-ink binder (PIB) printer with sand powder as raw material. They printed cylindrical and cuboid specimens and some samples had pre-existing cracks. The sand printed samples replicated natural rock and samples printed with PLA were used as molds for creating rock joints. UCS tests conducted on sand printed samples achieved general stress-strain behavior similar to natural rock. Also, direct shear tests performed on concrete samples cast in molds for a standard Barton's joint with JRC=6-8 generated accurate surface geometries and repeatable results, confirming the suitability of AM technology in producing repeatable rock replicas. One limitation they encountered was the low values for maximum stress (approximately 10 MPa) and elastic modulus (approximately 2 GPa).

Zhou and Zhu (2018) investigated the suitability of different raw material for replicating brittle and hard rock behavior. They used FDM, stereolithography (SLA) and powder-based methods with ceramics, PMMA (poly (methyl methacrylate)), gypsum, SR20 (acrylic copolymer) and resin to print samples and conducted UCS tests on them. In their results, powder-based

specimens exhibited very low compressive strengths and ductile behavior, while specimens made with resin and constructed with the SLA method reflected the strength and stress evolution processes of hard rock. In order to improve the brittleness of resin samples, they added macro-cracks and micro-defects to the samples and used post-processing techniques such as freezing. Zhu et al. (2018) further explored replicating a volcanic rock with its internal defects by using X-ray micro-CT and printing with transparent resin with SLA technique. They successfully replicated the microstructure of the natural rock and the compressive strength and Poisson's ratio agreed with the natural rock. However, the Brazilian disk tensile strength was about 35% higher and the strain at peak tensile stress was approximately 3 times larger compared to the volcanic rock. Also, the Young's modulus was significantly lower.

Furthermore Suzuki et al. (2017) used a multijet modelling method to create fracture networks and conducted flow tests. Head and Vanorio (2016) 3D printed a model of a carbonate pore space and measured its transport properties. Ishutov and Hasiuk (2017) used CT scanning to replicate the pore-network of Berea sandstone using a 3D printer with polyjet technology that used liquid polymer and was cured with UV light. Some discrepancies were reported on the desired pore size in the printed proxies. Hanaor et al. (2016) investigated the effect of grain morphology on bulk material properties. Different morphologies were generated in MATLAB, converted into .STL files and printed with a polyjet type 3D printer. Triaxial tests on these grains demonstrated that they can reproduce aspects of shear behavior and that grain shapes effect material behavior.

Perras and Vogler (2019) compared the mechanical characteristics of four different groups of 3D printed samples with natural sandstones. The natural sandstones were acquired from three quarries in Switzerland namely, Baerloch, Buchs, and Massongex.

The 3D printed rock specimens were constructed using Voxeljet and ExOne printers. For the Voxeljet, sand with grain size of 190 μm was mixed with acid prior to print. During the print,

the sand was deposited in layers and the furan resin was added building the specified geometry of the rock sample. The printed samples were placed in the furnace to dry at 90°C. The ExOne utilizes a binder jetting process where silicate binder and furan binder were used for the print and sand or ceramic beads were chosen as the binding material. The specimens were built in layers, and if the furan binder was used, then the samples were cured naturally, while with the silicate binder, microwaving was used to cure the prints. The 4 groups of fabricated specimens were as follows:

1- Voxeljet: silica sand and furan resin with binder catalyst (VJ-SF)
2- ExOne: silica sand and furan resin with binder catalyst (Ex1-SF)
3- ExOne: ceramic beads and silicate binder (Ex1-CS)
4- ExOne: silica sand and silicate binder (Ex1-SS)

Thin sections of the fabricated rocks showed that they had lesser grain-to-grain contact. The results of the UCS and Brazilian strength tests are given in Table 2.1. The results of the tensile tests showed that the mean values were in the range of 1.15 MPa to 1.38 MPa (the authors noted that failure patterns for Brazilian tests of the specimens made with ceramic beads were invalid, therefore the tensile strength results were not reliable). Based on these results, Perras and Vogler (2019) stated that the sand analogues had tensile strength similar to Buchs specimens, and slightly lower than specimens from Baerloch. They concluded that the sand-furan prints' behaviour was nearest to natural sandstone. The UCS tests showed that the natural sandstones had a wide range of strengths, while the printed samples were in the range of 2.26-6.91 MPa, with the sand-furan samples having the highest strength. The fabricated samples resembled the compressive strength of the Buchs sandstones. Comparing the modulus, the ExOne sand-silicate prints were the softest and the ceramic-silicate were the stiffest (within the range of 1.2-3.8 GPa), closest to the Baerloch sandstones. The ratio of UCS/BTS of the 3D printed aligned with the UCS/5 line based on the data by Perras & Diederichs (2014) and were closer to the Buchs sandstones.

Table 2.1. UCS and Brazilian test results of 3D printed samples and natural rock, from Perras and Vogler (2019)

3D printed	**VJ-SF**	**Ex1-SF**	**Ex1-CS**	**Ex1 -SS**
UCS-mean (MPa)	3.47	6.91	4.90	2.26
E_{50}-mean (GPa)	1.31	1.70	3.81	1.24
Brazilian test-mean (MPa)	1.38	1.35	1.20	1.15
Natural rock	**Massongex**	**Baerloch**	**Buchs**	
UCS-mean (MPa)	174.98	53.11	3.74	
E_{50}-mean (GPa)	40.57	4.66	0.13	
Brazilian test-mean (MPa)	19.68	5.26	1.02	

For the modulus ratio, Perras and Vogler (2019) mentioned that most of their data lies within the bounds for sandstones. Overall, they concluded that the sand-furan specimens were closer to natural rocks based on geomechanical procedures and relationships.

There are a number of ways to enhance the mechanical and physical properties of printed components. Maleksaeedi et al. (2014) used a vacuum infiltration process for enriching 3D printed alumina samples. An inkjet 3D printer was employed where alumina powder was spread onto a build platform and Poly Vinyl alcohol binder was deposited using nozzles, creating the specimen in layers. After the specimens were printed, they were kept in the print bed overnight, dried in the oven at 650°c for 2 hours and then pre-sintered at 1000°C for another 2 hours. The infiltration was carried out with alumina slurries. After the infiltration process, the spheres were sintered again for 2 hours at 1650°C. Results showed that after the infiltration process, the

porosity of the parts decreased, while the density increased (from 37% to 86%) and so did the strength (up to 15 times the original strength).

Parallel to the current thesis study, investigation took place on samples printed with silica sand using the binder jetting process. Hodder (2017) investigated the properties of 3D printed sand analogues on a microstructural level while Gomez (2017) examined their macro-mechanical properties and investigated the effect of layer orientation, layer thickness and binder saturation on the printed sample properties. Furthermore, Ardila (2018) explored the hydraulic properties of these rock replicas and studied their properties under different print configurations. Primkulov et al. (2017) studied the effect of curing temperatures on the strength of printed sand analogues. In the following chapter, these studies are discussed further.

2.3 Factors that affect joint shear behaviour

There are several factors which contribute to the shear strength of rock joints. They include basic friction, joint roughness, which causes interlocking between the joint surfaces and leads to dilation (Hencher and Richards, 2015), asperity strength and joint surface matching state (Zhao, 1997). Rock joints that are open and have zero tensile strength, do not have true cohesion. However, in incipient joints or joints where there is cementation between the joint surfaces, true cohesion contributes to the shear strength of the discontinuities (Hencher and Richards, 2015).

Friction is defined as the resistance to motion when two bodies slide tangentially against one another (Scholz, 2002). Amontons (1699) described friction with two laws that were first discovered by Leonardo da Vinci in the fifteenth century (Scholz, 2002):

1) Friction force is independent of the size of surface area of the bodies in contact.

2) Friction is in proportion to the applied normal load.

Basic friction is defined as the frictional element of shear strength of a planar joint. The basic friction angle is usually assessed by testing of saw-cut samples in direct shear or tilt tests, however factors such as surface texture, mineral coating of the joint surface, and weathering affect it and therefore based on the preparation and testing method, basic friction can be highly variable (Hencher and Richards, 2015). These authors proposed a method to obtain basic friction from dilation-corrected shear curves and then to add the field-scale roughness to assess the shear strength of joints in practice.

Roughness is defined as a measure of surface waviness (larger-scale undulations) and unevenness (small-scale undulations) relative to its mean plane. The roughness of the joint impacts its shear strength, especially when the walls are displaced. However, as the joint aperture or the thickness of the joint filling, or previous shear displacement increases, this effect is weakened (Brady and Brown, 2013). Roughness causes dilation to occur when joints are sheared and effects friction angle and peak shear strength (Grasselli et al., 2002). In direct shear tests conducted on laboratory samples, the measured damaged asperities were on the scale of millimeters (Grasselli et al., 2002). The joint roughness is the hardest to quantify and therefore is studied extensively (Tian et al., 2018).

2.4 Shear strength criterion

Many researchers have investigated the shear behavior of closed joints. Li et al. (2016b) presented a comprehensive list of those researchers (e.g., Patton (1966), Ladanyi and Archambault (1969), Barton (1973), Barton and Choubey (1977), Saeb and Amadei (1992), Grasselli and Egger (2003), Oh et al. (2015)). Some are mentioned below.

Patton (1966) proposed a bilinear strength envelope. He stated that under low normal stresses, the shear strength is controlled by a sliding mechanism (2.1); once the normal stress surpasses a transition stress, shearing through the asperities takes place (2.2).

$$\tau = \sigma_n tan[\emptyset_\mu + i] \quad (2.1)$$

$$\tau = c_j + \sigma_n tan\ \emptyset_r \quad (2.2)$$

where τ is shear strength, σ_n is normal stress, $\emptyset_\mu$ is sliding friction angle, i is asperity inclination angle, c_j is apparent joint cohesion and $\emptyset_r$ is residual friction angle. The shortcoming of this approach is that in rough joints, sliding and shearing occur concurrently (Bahaaddini et al., 2016).

Based on joint roughness coefficient (JRC), the Barton-Bandis empirical shear model (Barton, 1973, Barton and Choubey, 1977, Barton and Bandis, 1990) was formed:

$$\tau = \sigma_n\, tan\left[\emptyset_r + JRClog\left(\frac{JCS}{\sigma_n}\right)\right] \quad (2.3)$$

where σ_n is the normal stress, $\emptyset_r$ is the residual friction angle and JCS is the joint wall compressive strength. Determining the JRC coefficient is the most challenging aspect of this model (Bahaaddini et al., 2016).

Grasselli and Egger (2003) noticed the relationship between peak shear strength and potential contact area. This was based on observations by Grasselli et al. (2002) that when the joint shears, the stress is redistributed on the asperities beginning with the steepest asperity. Therefore, the potential damage area would involve asperities that are facing the shear direction and are steeper than a critical inclination angle. Based on the above assumptions, the following equation was devised to describe the relationship between the potential contact area (A_{θ^*}) and the angular threshold (θ^*) (Grasselli et al., 2002):

$$A_{\theta^*} = A_0 \left(\frac{\theta^*_{max} - \theta^*}{\theta^*_{max}}\right)^C \quad (2.4)$$

where A_0 is the maximum possible contact surface area, which corresponds to $\theta^* = 0$, θ^*_{max} is the maximum apparent dip angle in the direction that the surface is sheared and C is a fitting

parameter, which shows the "roughness", and is achieved by using a best-fit regression function. This parameter represents the distribution of the apparent dip angles on the shear surface. Tian et al. (2018) mentioned a few drawbacks regarding Equation (2.4) which included: there was no reasonable explanation for the way A_0, θ^*_{max} and C were combined; A_0 is not suitable for quantifying surface roughness; and θ^*_{max} is very sensitive to sampling interval when scanning the surface.

Grasselli and Egger (2003) developed an equation for the peak shear strength of rock joint:

$$\tau = \sigma_n \tan\left[\emptyset_b + \left(\frac{\theta^*_{max}}{C}\right)^{1.18cos\propto}\right] \times \left[1 + e^{-\left(\frac{\theta^*_{max}}{9A_0C}\right)\left(\frac{\sigma_n}{\sigma_t}\right)}\right] \quad (2.5)$$

where σ_n is the normal stress, $\emptyset_b$ is the basic friction angle, $\propto$ is the angle between the schistosity plane and the plane normal to the joint and σ_t is the tensile strength.

A few other researchers (e.g., Tatone, 2009, Xia et al., 2014, Yang et al., 2016) modified Grasselli's model for peak shear stress. However Tian et al. (2018) mentioned a few shortcomings with these models: for Grasselli and Tatone's models, the forms of the equations are complex; for flat joints, the models don't follow Mohr-Coulomb's criteria; and the combination of the morphological indexes is unclear. For Xia et al.'s model, there isn't a clear relationship between joint morphology and the maximum possible contact surface area (A_0) and the computing accuracy is low. As for Yang et al.'s model, there is no reasonable explanation for the combination of parameters C and θ^*_{max}. Tian et al. (2018) updated Grasselli's model and developed a new shear criterion based on a new morphological parameter and although the computation is feasible for engineering applications, there were some discrepancies between the lab results and the model which Tian et al. (2018) contributed to not taking into account the size/shape of the specimens, the degree of the joint matching between the two surfaces of the joint, and sampling intervals.

Also, other than the apparent dip angle, the joint roughness might be affected by other factors, which were not considered in their study.

In another study, Li et al. (2016a) proposed a constitutive model based on critical laboratory scaled waviness and unevenness and defined different degradation constants for each of them. They mentioned that among the small- scale asperities, the unevenness with large wavelength is a key contributor to shear strength.

2.5 Quantifying surface roughness

There are several ways to quantify surface roughness and although characterizing the entire 3D surface is preferred, however, quantifying 2D profiles is beneficial for applications of empirical equations of shear strength (Rasouli and Harrison, 2010). To quantify the roughness of the surface of the joints certain methods and parameters are used which are categorized into three groups, namely empirical methods, fractal methods and statistical parameters (Tatone, 2009). The most significant empirical method is the joint roughness coefficient (JRC) (Barton, 1973, Barton and Choubey, 1977, Barton and Bandis, 1990). A set of 10 standard profiles were developed by Barton and Choubey (1977), shown in Figure 2.1, to compare with a given joint to determine its roughness. JRC values range from 0 for smooth joints to 20 for rough joints. Since the comparison is done visually, it is subjective in nature (Beer et al., 2002).

Tatone and Grasselli (2010) introduced a 2D roughness metric (Equation (2.6)) based on the 3D roughness metric. To obtain this roughness, first the direction of shear is selected, and the inclination angle of the segments making up the profile in that direction are obtained. Then the normalized length, L_{θ^*}, which is the accumulation of line segments that are steeper than a threshold value, θ^* divided by total profile length is calculated. The cumulative distribution of L_{θ^*} versus $\theta^*$are drawn, and the 2D roughness metric is obtained from a curved fitting method:

$$\frac{\theta^*_{max}}{(C+1)_{2D}} \tag{2.6}$$

where θ^*_{max} is the maximum inclination of the joint in the chosen shear direction, and C is an empirical fitting parameter, that represents the shape of the cumulative distribution.

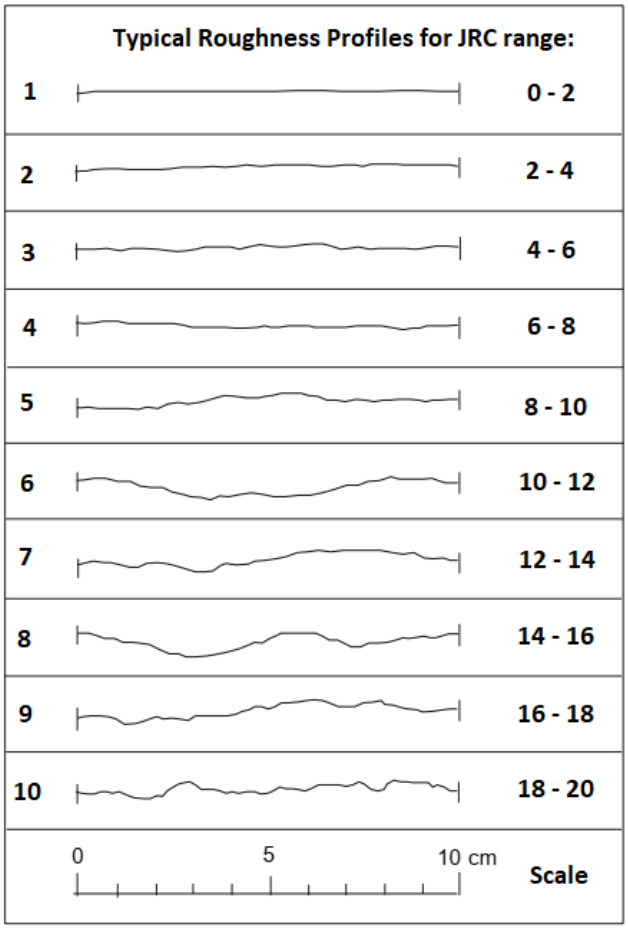

Figure 2.1. Standard JRC profiles (After Barton and Choubey, 1977). Figure modified from (Palmström, 2001).

Another method to define surface roughness is the use of fractals. The investigations of Mandelbrot (1967, 1983, 1985) popularized fractals, that are used to describe patterns in nature where because of their irregularity cannot be readily described by Euclidian geometry. Each portion of the fractal geometry is a reduced image of the whole in a way. Fractals can be self-similar or self-affine. Self–similar fractals will keep their statistical properties when scaled isotropically, however, self-affine fractals must be scaled in an anisotropic manner to maintain

statistical similarity (Mandelbrot, 1985). Many studies noted joint surfaces to be self-affine (e.g., Seidel and Haberfield, 1995, Fardin et al., 2001) and attempted to quantify surface roughness using fractal methods. In a recent study, Li et al. (2017) mentioned that fractals are suitable for interpreting surface roughness and because they can recognize surface geometry at all sizes, they are attractive for quantifying roughness at different scales. They proposed a shear model where the roughness of a joint was described using the amplitude parameter and fractal dimension, however it was applicable for joint lengths lower than a stationary value.

Finally, Statistical parameters are used to describe and quantify surface texture in the field of tribology (e.g., Menezes et al., 2013, ASME B46.1, 2009). They have made their way into rock engineering practices and are commonly used to quantify joint geometry. They are investigated further in the next section.

2.5.1 Statistical parameters

Statistical parameters include those that describe the magnitude (amplitude) of surface roughness and those that describe the texture of surface roughness (e.g., Seidel and Haberfield, 1995). Maerz et al. (1990) mentioned that the parameters chosen to described surface roughness should have low intercorrelation, and Hong et al. (2008) stated that both types of parameters (i.e., amplitude and inclination angle) are needed to quantify joint roughness. Examples of amplitude parameters are maximum profile peak height (R_p), defined as the distance between the highest asperity and mean line; maximum profile valley depth (R_v) which is the distance between the lowest height and mean line; and maximum height of the profile (R_t), defined as the vertical distance between the highest and lowest height of the profile, i.e., $R_t = R_p + R_v$, shown in Figure 2.2 (ASME B46.1, 2009). Some more refined amplitude parameters are centerline average asperity height (CLA) or roughness average (R_a) (ASME B46.1, 2009), root mean square asperity

height (RMS) or rms roughness (R_q) (ASME B46.1, 2009) and mean square value roughness index (MSV). Definitions are as follows (Tse and Cruden, 1979, Maerz et al., 1990):

$$CLA = R_a = \frac{1}{L}\int_{x=0}^{x=L} |y| dx \approx \frac{1}{N}\sum_{i=1}^{N} |y_i| \tag{2.7}$$

where y is the height of the profile, measured from a mean reference line, L is the length of the profile, and N is the number of discrete measurements of height.

$$RMS = R_q = \sqrt{\frac{1}{L}\int_{x=0}^{x=L} y^2 dx} \approx \sqrt{\frac{1}{N}\sum_{i=1}^{N} y_i^2} \tag{2.8}$$

$$MSV = \frac{1}{L}\int_{x=0}^{x=L} y^2 dx \approx \frac{1}{N}\sum_{i=1}^{N} y_i^2 \tag{2.9}$$

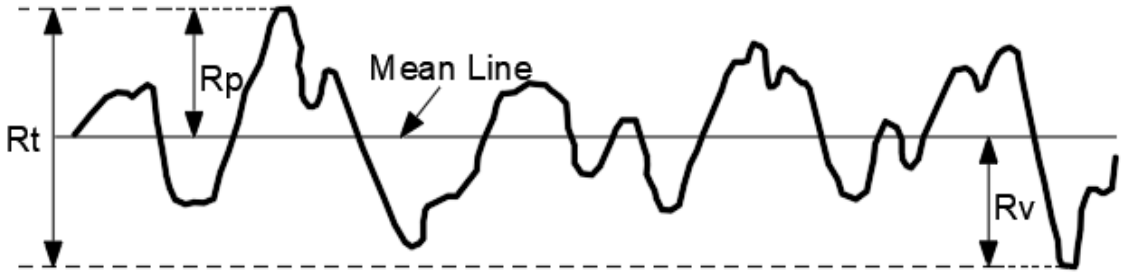

Figure 2.2. Examples of amplitude statistical parameters R_p, R_v and R_t, redrawn from ASME B46.1, 2009.

Example of texture parameters are the root mean squares of the first derivative of the surface profile (Z_2) (Myers, 1962), standard deviation of the angle i (SD_i) (Yu and Vayssade, 1991), roughness profile index (R_p) (El-Soudani, 1978) which is the ratio of total length of the profile to its projected length. These parameters are defined as follows:

$$Z_2 = \sqrt{\frac{1}{L}\int_{x=0}^{x=L}\left(\frac{dy}{dx}\right)^2 dx} \approx \sqrt{\frac{1}{L}\sum_{i=1}^{N-1}\left(\frac{(y_{i+1}-y_i)^2}{(x_{i+1}-x_i)}\right)} \tag{2.10}$$

where y is profile amplitude, N is the number of discrete measurements and L is the length of a profile.

$$SD_i = tan^{-1}\sqrt{\frac{1}{L}\int_{x=0}^{x=L}\left(\frac{dy}{dx} - \tan\left(i_{ave}\right)\right)^2 dx} \tag{2.11}$$

$$i_{iave} = \frac{1}{L}\int_{x=0}^{x=L} tan^{-1}\left(\frac{dy}{dx}\right)dx \tag{2.12}$$

Directionality of surface roughness is also important in determining the shear response of joints (e.g., Grasselli and Egger (2003) mentioned that the size and location of the asperities that are involved in the shearing process depend on shearing direction). As such, some parameters are defined to measure the directionality of profiles. Myers (1962) defined the Z_4 parameter:

$$Z_4 = \frac{\sum(dx_i)_p - \sum(dx_i)_n}{L} \tag{2.13}$$

where $(dx_i)_p$ is the distance where the slope is positive, $(dx_i)_n$ is the distance where the slope is negative, and L is the total profile length.

Zongqi and Ming (1990) mentioned a 'forward' and 'backward' RMS-slope parameter (which is the same as the Z_2 parameter), where in the forward parameter, the data points which $y_{i+1} > y_i$ are considered and for the backward parameter, data points which $y_{i+1} < y_i$ are taken into account. Zhang et al. (2014) called this the modified root mean square (Z'_2) and defined it as follows:

$$Z_2' = \sqrt{\frac{1}{L}\int_{x=0}^{x=L}\left[\max\left(0,\frac{dy}{dx}\right)\right]^2 dx} \approx \sqrt{\frac{1}{L}\sum_{i=1}^{N-1}\left(\frac{(max(0,y_{i+1}-y_i))^2}{(x_{i+1}-x_i)}\right)} \tag{2.14}$$

2.5.2 Relationship between JRC and statistical parameters

To determine the JRC values of surface roughness, it is quite possible for different practitioners to assign different values of JRC for the same profile based on visual inspections. To overcome this bias, attempts have been made to correlate JRC values with other objective parameters. JRC has been correlated with Z_2, CLA, RMS, MSV (e.g., Tse and Cruden, 1979), roughness profile index (R_p) (Maerz et al., 1990), standard deviation of angle i (SDi) (Yu and Vayssade, 1991), fractal dimension (Li and Huang, 2015) and the 2D roughness matric (Tatone and Grasselli, 2010).

The existing empirical relationships between statistical parameters and JRC coefficients are summarized in Li and Zhang (2015). The Z_2 parameter is common among the mentioned parameters and some of the more frequently used relationships between Z_2 and JRC are listed herein. They include equations by Yang et al. (2001) (Equation (2.15)), Yu and Vayssade (1991) (Equation (2.16) and Equation (2.17)) and Tse and Cruden (1979) (Equation (2.18)).

$$JRC = 32.69 + 32.98 \log(Z_2) \tag{2.15}$$

$$JRC = 61.79 Z_2 - 3.47 \tag{2.16}$$

$$JRC = 54.42 \sqrt{Z_2} - 14.83 \tag{2.17}$$

$$JRC = 32.2 + 32.47 \log(Z_2) \tag{2.18}$$

Tatone and Grasselli (2010) also derived empirical relations:

$$JRC = 51.85 (Z_2)^{0.60} - 10.37 \tag{2.19}$$

Liu et al. (2017) proposed a weighted fitting equation:

$$JRC = 16.09 log\, {Z_2}^{1st} + 12.70 \log {Z_2}^{2nd} \tag{2.20}$$

where ${Z_2}^{1st}$ is for sampling interval of 5.0 mm and ${Z_2}^{2st}$ is for sampling interval of 0.5 mm.

The above relationships resulted from the digitization and analysis of the ten standard profiles proposed by Barton and Choubey (1977). To include a larger set of joints, Li and Zhang (2015) extracted data on 112 joint profiles of various rock types from literature and derived new empirical equations. They correlated JRC to parameters such as SD_i, Z_2, MSV, CLA and R_p. SD_i and Z_2 were found to have the highest correlation with JRC. Equation (2.21) displays the relationship of Z_2 to JRC based on their work.

$$JRC = 55.7376Z_2 - 4.1166 \tag{2.21}$$

Equations (2.15) to (2.19) were derived based on 0.5 mm sampling interval, however, the equations of Li and Zhang (2015) were derived on the digitization of the profiles at every 0.4 mm.

Zhang et al. (2014) proposed an equation to estimate JRC based on a new roughness index (λ) which considers the directional slope (Z'_2) and height (amplitude) of the profiles. This way, the roughness of the profile is more adequately captured. The equations for JRC were developed based on the digitization of 64 profiles from Bandis (1980). An average JRC and an upper bound and lower bound is calculated according to Equations (2.23), (2.24) and (2.25).

$$\lambda = \left(\frac{h}{L}\right)^{\alpha} (Z_2')^{1-\alpha} \tag{2.22}$$

$$JRC = \left(\frac{40}{1 + e^{-20\lambda}}\right) - 20 \tag{2.23}$$

$$JRC_{upper} = \left(\frac{40}{1 + e^{-30\lambda}}\right) - 20 \tag{2.24}$$

$$JRC_{lower} = \left(\frac{40}{1 + e^{-15\lambda}}\right) - 20 \tag{2.25}$$

where $\alpha = 1/3$.

2.6 Overview of CNL and CNS boundary conditions

In practice, rock joints may be sheared under conditions where they are confined and therefore dilation is constraint and the normal stress varies. In this case, the constant normal load (CNL) boundary condition is no longer applicable and constant normal stiffness (CNS) better represents field conditions. While CNL boundary conditions appropriately present unreinforced slopes where the rock block moves freely during shear, CNS conditions become more prominent in the movement of blocks in the roof or walls of tunnels, underground carbon dioxide sequestration and waste disposal sites, and in anchor reinforced rock slopes (e.g. Jiang et al., 2006). In these situations, CNS test results are economically favorable (Indraratna et al., 1998). Normal to the joint, the stiffness of the surrounding rock mass is assumed constant (Indraratna and Haque, 2000) . A schematic diagram of CNL and CNS conditions is drawn in Figure 2.3.

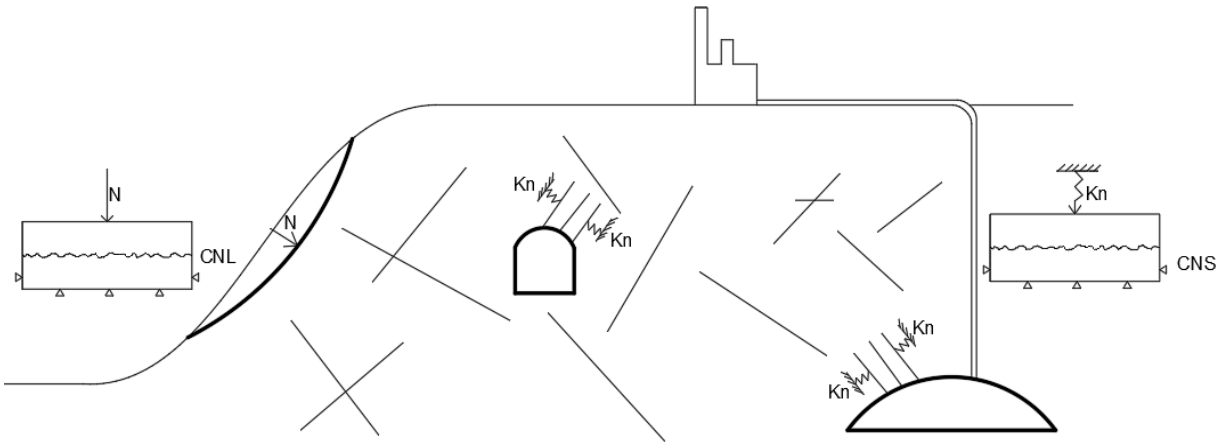

Figure 2.3. Schematic of CNL and CNS boundary conditions.

A significant body of literature exists on direct shear tests carried out under CNL conditions (e.g., Gentier et al., 2000, Asadi et al., 2013, Johansson, 2016). Some researchers studied single asperities (e.g., Huang et al., 2002), while others studied idealized asperity geometry for example saw-tooth patterns (e.g., Asadi et al., 2013) and JRC profiles (e.g., Ueng et al., 2010). However, there have been less investigations completed under CNS conditions. Among these, most studies

were done on joint replicas using conventional material (e.g., Seidel and Haberfield, 2002, Indraratna et al., 2015). Replicated material allow for identical specimens to be tested multiple times and under different test conditions. Some experiments were conducted on triangular profiles or standard JRC profiles (Kodikara and Johnston, 1994, Seidel and Haberfield, 2002, Jiang et al., 2004b) or using the joint geometry from natural rock (Jiang et al., 2004b, Indraratna et al., 2015). A few infilled joints were also studied (Indraratna et al., 1999).

Although in situ large-scale shear tests are often cited as the most favorable method to study the shear behaviour of rock fractures (e.g., Muralha et al., 2014), however they have their limitations. Such tests are conducted on joints with a limited dimension of a few square meters (Tatone and Grasselli, 2012), are prohibitively costly and difficult to execute and the interpretation of results is challenging compared to laboratory direct shear tests (Hencher and Richards, 2015). Therefore, most of the tests in literature were carried out in the laboratory.

Figure 2.4 shows typical shear stress, normal displacement and normal stress versus shear displacement curves for joints under CNL and CNS conditions where dilatancy is suppressed (after Goodman and John, 1977). In CNL conditions during the shearing of the joint, the force that is normal to the shearing plane is constant, but in constant normal stiffness conditions, the normal force on the shearing plane increases with increasing dilation (Benmokrane and Ballivy, 1989). Li et al. (2018) mentioned that the shear stress- shear displacement plots in CNL and CNS have the same four stages, namely the elastic stage, followed by the pre-peak asperity sliding stage, then continued to the progressive asperity damage stage and finally, the residual stage is reached. In CNS, when sliding of the asperities begins, dilation occurs, and consequently normal stress is increased. At the damage stage, as the asperities degrade, the dilation rate declines and therefore the increment of normal stress decreases. When asperities are mostly worn off, the stress reaches the residual stage. Of note is that Hencher and Richards (2015) mentioned that for natural joints,

the strength at the end of a shear test depends on the roughness and texture, shear direction and applied normal stress and is not a fundamental property of the joint.

In laboratory tests, the normal stiffness (K_n) may be simulated by a spring (e.g., Indraratna et al., 2015) or using a feedback system that modifies the normal load applied on the joint (e.g., Porcino et al., 2003, Jiang et al., 2004b). The value of K_n is controlled by the surrounding rock mass or the rock reinforcement (Indraratna et al., 2015). Normal stiffness has great influence on the shear strength, mechanical and hydraulic aperture. Jiang et al. (2004b) also reported that the change in mechanical aperture is affected by the JRC value of the joints and is smaller in CNS compared to CNL tests.

Not all shear stress-shear displacement CNS tests in the laboratory reported having a distinct peak shear stress. Indraratna et al. (2015) did not notice a peak and said this might be due to the compaction of the gouge that was created by asperity damage, therefore lessening the effect of other asperities. One other reason stated was that the rolling friction of the gauge

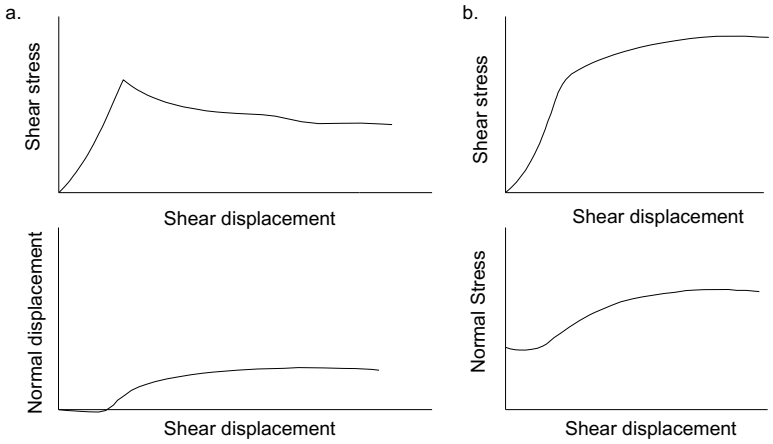

Figure 2.4. Shear stress, normal displacement and normal stress versus shear displacement for a. CNL b. CNS when the dilation is constrained (modified from Goodman and John, 1977)

becomes more prominent compared to sliding friction. Jiang et al. (2004b) also reported strain hardening behavior in CNS for some of their tests based on standard JRC joints. Rim et al. (2005) studied CNS tests on cement replicated triangular saw-tooth and natural roughness joint profiles

under various initial normal stresses and stiffnesses. The shear stress-shear displacement tests revealed two distinct peak shear stresses: the initial peak was defined as the sudden change in shear stress, where shear displacement was under 3 mm, and the second peak shear stress was identified as the maximum shear stress in the entire test. Results indicated that the initial peak stress was correlated with the initial normal stress however the second peak stress correlated with the normal stiffness.

Poturovic et al. (2015) emphasized the role of dilation capacity on shear strength in CNL and CNS conditions. They conducted 15 tests on replicas of natural joints and subtracted the measured and fictitious dilation angle from the total friction angle. They concluded that the coefficient of friction for CNL and CNS conditions corresponded well with each other and therefore using only one CNS test was enough for determining the failure criterion. Also, they mentioned that in CNL conditions the maximum shear resistance and maximum coefficient of friction correspond together, whereas in CNS conditions, the normal stress and shear stress continued to increase after maximum coefficient of friction was reached. The dilation capacity continued to decrease until the maximum shear stress was reached, as well.

Lindenbach and Bearce (2018) performed direct shear tests on sawtooth hydrostone cement specimens and concrete samples which were first sheared as intact samples, then sliding tests were performed on the joints created immediately afterward. They were tested under various normal stiffnesses. The results showed that the stress paths for the saw-toot joints were below the CNL failure envelope, however for the concrete samples, they tended to follow the failure envelope. Mouchaorab and Benmokrane (1994) conducted shear tests on triangular joints with angles of 15, 25 and 45 degrees on cement replicas in CNS conditions. Their results showed a damping periodic behavior in the shear stress-shear displacement curve for 15- and 25- degree angle profiles and abrupt decrease in shear strength for 45 degrees asperities due to loss of cohesion at asperity level.

Thirukumaran and Indraratna (2016) reviewed the models proposed for CNS conditions and noted that studies such as Leichnitz (1985), Skinas et al. (1990), Saeb and Amadei (1990) and Saeb and Amadei (1992) proposed models where stress history was not considered. However, they argued that because the increase in normal stress during shearing may lead to various levels of asperity damage, this assumption is not always correct. Others did consider stress paths, but those models were validated for regular shaped asperities (e.g., Heuze, 1979) or required a lot of calculations (Indraratna et al., 2010). Indraratna et al. (2015) proposed an analytical model for shear behavior of joints in CNS by modeling the dilation of the asperities and validated them using gypsum-based rock replicas with three different roughness profiles. They considered asperity damage during shear. Further validation is needed for a larger group of joints. Li et al. (2018) proposed an analytical model based on critical asperities in lab-scale direct shear tests based on evaluable parameters. The progressive degradation of asperities was considered, but the role of potential gouge produced during shear needs further investigation. Wang et al. (2018) also modeled the shear-displacement curves in a stepwise fashion based on plasticity theory.

2.7 Overview of Discrete Element Method

The nature of rock failure is complex and for jointed rock mass, evaluating the shear strength requires formidable experimental and theoretical understanding (Hoek, 1983). This makes the application of numerical simulations to rock mechanics problems appealing and at the same time challenging. Numerical methods have been extensively applied to simulate rock fractures, and typically numerical methods are categorized into continuum methods and discrete methods. Some simulations use a hybrid of both methods. Continuum methods include the finite difference method (FDM), the finite element method (FEM) and the boundary element method (BEM) (Jing and Hudson, 2002). Discrete methods on the other hand include implicit and explicit methods (Lisjak and Grasselli, 2014).

The principle assumption of continuum methods is that the domain is a continuous body and the presence of discontinuities is accounted for using two main approaches (Lisjak and Grasselli, 2014):

1- When the number of fractures is relatively large, homogenization of the domain is used meaning the strength parameters and the rock mass deformation modulus is reduced.
2- When the number of discrete discontinuities is limited, these features can be adopted into the continuum formulation.

The disadvantages of the homogenization approach are that the separation, rotation and slip of blocks cannot be modelled (Hammah et al., 2008). For instances where fractures are incorporated as interfaces (i.e., the second approach), although strains and rotations of discrete bodies can be accommodated, however the changes in the edge-to-edge contacts on the interfaces should be minimal and this can only be accomplished where the displacements and rotations of the joints are small (Lisjak and Grasselli, 2014).

To overcome these limitations, and because the micro-mechanisms in rock are complicated phenomena which continuum theories have difficulty portraying (Potyondy and Cundall, 2004), a promising approach is to use the discrete modelling methods, also known as discrete element method (DEM). DEM simulations allow for an explicit approach to investigate the behaviour of discontinuum material. In DEM, discrete bodies can rotate and displace finitely, and new contacts are made within the simulations (Lisjak and Grasselli, 2014). One main program that adopts the explicit form of DEM (which is called the distinct element method) is particle flow code (PFC), from Itasca Consulting Group. In PFC, a bonded particle material (BPM) is created which models rock as a cemented granular material. In this model, the particles interact dynamically, and equilibrium is reached when the internal forces are balanced. Damage is simulated explicitly by the formation, interaction and propagation of micro-cracks (Potyondy and Cundall, 2004).

In the particle-based models, one principal advantage is that simple contact logic replaces complex constitutive relationships. However, the number of simulations needed to verify that simulations correctly represent the macro-scale behaviour of rock specimens, increases. This is done by modifying micro-scale parameters in the model and observing the macro-scale behaviour (Lisjak and Grasselli, 2014). In the BPM, because particles and bonds represent similar micro-objects in real rock (Potyondy and Cundall, 2004), one of the interests of using 3D printed material to replicate rock is to directly input the micro-parameters into the simulations without the need for a trial and error process. This was the focus of the research carried out by Hodder (2017), where he simulated a 3D printed sand specimen in a UCS setup in PFC3D. His research found that the Young's modulus of the simulations was in the range of experimental results, however the UCS was significantly less than expected. This area requires substantial investigation.

Several researchers have conducted direct shear tests in PFC numerically over the years. Almost all the research has been applied on CNL boundary conditions. However, CNS conditions have also been simulated (for example, Bewick et al. (2014a) and Bewick et al. (2014b) for intact rock under direct shear, Wang et al. (2015) for joints and Shang et al. (2018) for incipient joints).

Cundall (2000) simulated a joint in CNL conditions in 2D and reported that the dependence of peak shear strength and dilation to normal stress, also asperity degradation corresponded to laboratory experiments. Park and Song (2009) modelled a rough joint (JRC=18-20) in PFC3D and investigated the effect of micro-parameters on the shear behaviour of the joints in CNL conditions. They used the contact bond model and obtained UCS=55.02 MPa, and E=55.45 GPa for the intact rock. The particles comprising the joint were assigned zero bond strength for the contacts between the upper and lower joint particles. Due to the roughness of joint particles (balls), artificial roughness was produced in place of the intended roughness. Park and Song (2009) showed that the failure process of the simulations was close to laboratory findings. They found that the peak shear strength was controlled by the roughness, contact bond strength ratio

and friction coefficient. The friction coefficient was the most prominent factor in determining both the dilation angle and the shear strength.

Asadi et al. (2013) modelled direct shear tests on triangular and wavy shaped asperities. They calibrated the intact material to UCS tests and showed that for the triangular asperities, with the increase of asperity angle, the fracture mode changed from sliding to tensile cracking, and the damage zones were similar to laboratory tests. However, PFC overestimated the peak shear strength values for various normal loads. They attributed this to the cohesive effects of particles that were located on opposite sides of the joint profile. They did not use smooth-joints in their simulations.

Lambert and Coll (2014) generated a natural joint surface in granite in PFC3D and ran direct shear tests in CNL conditions. Parallel bonds were used for the intact particles and smooth-joints contacts were adopted to simulate the joints. The smooth-joint contacts diminished the inherent roughness associated with the particles representing the joint. Also, the radius of the balls varied from 0.5 mm (in the vicinity of the joint) to 2.4 mm (towards the walls). This allowed for less computational time. The intact rock micro-properties were varied to match the measured UCS and Young's modulus. They achieved relatively good agreement between the simulations and Barton's empirical equation. However, the dilation was overestimated for high normal stresses. Lambert and Coll (2014) also performed a parametric analysis on the effect of smooth-joint micro-parameters on shear behaviour of the joints. They found that the increase in joint friction angle increased the peak shear strength, and the behaviour of the joint became more brittle. However, joint dilation was untouched by these changes. Further, the increase in joint normal stiffness didn't affect the peak strength significantly, and this was most likely because of the stress redistribution between the two joint walls. Finally, the increase in smooth-joint shear stiffness increased the joint shear stiffness but didn't impact the normal dilation.

Bahaaddini and coworkers conducted several numerical studies on rock joints (e.g., Bahaaddini et al., 2013, Bahaaddini et al., 2015, Bahaaddini et al., 2016). They put forward a shear box generation approach to address the particle interlocking problem: when using smooth-joints to simulate fracture profiles, during shear, PFC could not detect the particles that lay on opposite sides of the joint profile, therefore after large displacements, particle interlocking took place. They compared the numerical simulations on saw-tooth joints and standard profiles with empirical equations and/or laboratory experiments. Their results showed that PFC can reproduce shearing mechanisms, which is influenced by joint geometry and applied normal load. It can also simulate crack propagation leading to asperity degradation and asperity shearing off. They suggested further study of asperity degradation at residual shear stages is needed. Lazzari et al. (2014) compared laboratory direct shear tests on medium to course-grained granite and mentioned that the smooth-joint contact segments should be short enough to properly capture the joint roughness. Consequently, the ball radius near the joint surface should be small (for their work they suggested an average particle radius equal to 0.06 mm), which increases computation time. They also encountered the same particle interlocking as Bahaaddini et al. (2013) shown in Figure 2.5.

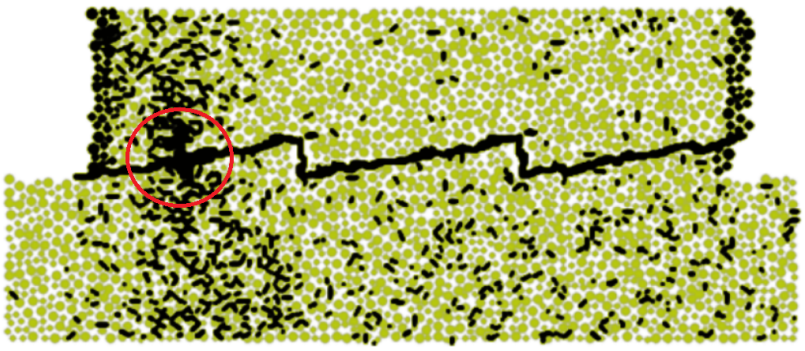

Figure 2.5. Particle interlocking which resulted in unusual stress concentration around the interlocked particles. Figure modified from Lazzari et al. (2014).

In a recent study, Bayona et al. (2018) compared the shear strength of a profile with JRC 10-12 to equivalent profiles generated based on fractals. They used parallel bonds for simulating

the intact material and smooth-joint contacts were inserted where the joints were located. To resolve the problem of interlocking between the particles on the joint surface, a high value for smooth-joint normal stiffness micro-property was chosen. Also, the shear box generation was based on the approach by Bahaaddini et al. (2013) where the two parts of the shear box are generated separately by inserting a wall in place of the fracture geometry in the specimen generation. They concluded that even though PFC is capable of simulating shear stress-shear displacement curves qualitatively, however the numerical simulations underestimated peak shear strength values compared to Barton and Choubey (1977) empirical criterion. Several reasons were cited for this discrepancy which included running tests in 2D and the inability of tilting of the shear box during testing.

From the above review it is apparent that even though there have been many studies that have adopted the DEM for analyzing the direct shear response of joints in rock, however, there still remains many differences between laboratory and simulated results. The current research will attempt to understand some of these discrepancies.

3 Feasibility of using additive manufacturing to replicate rock proxies and fracture geometry in direct shear tests

3.1 Introduction

Additive manufacturing is gaining traction in the field of rock mechanics and reservoir geomechanics because of its ability to rapidly produce complex structures. In this chapter, in the first section, the printing processes developed to build the sand analogues for intact rock are presented, and the effect of different print configurations and post processes on the strength and deformation of the analogues are investigated. The printed rock is then compared to natural rock.

The 3D printed sand proxies are material that previously have not been tested under direct shear. Thus, in the second section, to investigate the response of this material in direct shear, rock joints with simple geometry were printed and tested in the GCTS direct shear apparatus under constant normal load (CNL) conditions. They were printed with the M-Flex printer, using the procedures that were optimized for the intact sand proxies in the first section.

A brief look at an alternative method to adopt AM technology to create rock proxies, that is the fused deposition modeling (FDM) printing process is provided. In this process, molds are printed, and gypsum cement is cast to make the rock and joint replicas.

3.2 Intact sand analogues

3.2.1 Sample preparation

3.2.1.1 Printing process

Sand specimens were prepared with ExOne's M-Flex 3D printing machine (ExOne, PA, USA) shown in Figure 3.1. The printer uses additive manufacturing technology by depositing one layer of powder and one layer of binder alternatively on a print bed, in order to build the desired specimen geometry. The powder included silica sand mixed with an activator. ExOne FA001 was the activator which consisted mostly of P-toluenesulfonic acid. The binder liquid was ExOne FB001 which consisted mainly of furfuryl alcohol with trace amounts of bisphenol A, resorcinol, and 3-aminopropyltriethoxysilane. Furfuryl alcohol polymers are used as sand molds in traditional metal casting (McKillip, 1989). The activator acts as a catalyst for the binder, allowing the binder to fully crystallize.

The procedure was to mix 1.4 grams of acid per 1000 grams of sand at 135 rpm prior to printing. A stand mixer was used for the pre-mixing. The mixing time was approximately 2 minutes, although if needed, this time was extended to ensure that the sand was uniformly coated with the acid. The complete integration of acid with silica sand was necessary; if they were not fully mixed, the flowability of sand coming out of the recoater was jeopardized, which altered the print quality. The mixed sand was dropped into the hopper. The hopper sat on the top corner of the printing machine, and it supplied the recoater. The printer recoater deposited the powder at a constant speed on the print bed and it vibrated during the deposition. The print bed is a platen located inside a steel container called the job box. Then, the printhead which was equipped with 4 × 256 piezoelectric nozzles, dispensed the binder liquid onto the powder. Once the binder came in contact with the acid (which was the activator), the furfuryl alcohol started to polymerize, forming the shape of the sand analogues based on the uploaded digital file. The micro drops of

liquid were dispensed in closely spaced lines ensuring the coverage of sand particles on the print bed. The printhead had the ability to move along the X-axes and Y-axes and was fixed in the Z-direction.

Figure 3.1. M-Flex 3D printing Machine, (M-FLEX 3D Printing System User Manual, 2014), modified.

After each layer the print bed moved down at a specified distance in the job box, parallel to the axis normal to the sand layer, allowing for the printing of the next layer. An option to apply heat to the sand layers during print was available. The thickness of each powder layer was set to 250 μm and the particle size distribution of silica sand was narrow (D10=110 μm, D50=175 μm, D90=220 μm). The grain matrix of printed sand specimens are depicted in Figure 3.2 (from Hodder, 2017). Printing with this procedure lead to printed analogues where the binder mainly accumulated at the sand grain contacts. After the print was completed, the samples were post processed in the oven by heat-curing. The effect of printing configurations such as binder saturation and layer orientation on print properties, also the curing process is discussed in more detail in the next sections.

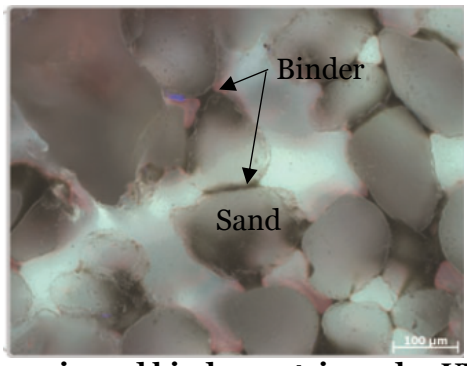

Figure 3.2. Image of the grain and binder matrix under UV light from a polymer-saturated section of a 3D printed sample. The rounded shapes of the sand and the darker coloured binder that is placed at the grain-grain contacts are illustrated (Modified with permission from Hodder, 2017).

3.2.1.2 Binder saturation

Binder concentration during the build process effects the properties of the printed specimens. Binder saturation is the percentage of the pore space filled with the Furan binder. The first printed specimens using M-Flex were printed with 10% set binder saturation (Osinga et al., 2015). The printing machine controls assumes that the loose packing porosity is approximately 40%, therefore a binding saturation of 10% means that binder content should be equivalent to 4% of total volume. However, the actual binder volume was 1.5 times the set binder volume fraction which was probably due to a calibration issue (Hodder et al., 2018).

Gomez (2017) investigated the effect of binder saturation on the strength of 3D printed sand specimens printed with the activated sand and M-Flex binder in layers. The samples were cured at room temperature after print. They found that the UCS of cylindrical samples of approximately 1.5 inch diameter and 3 inch height increased from 14.78 MPa to 18.02 MPa to 20.78 MPa, for a set binder saturation increasing from 10% to 15% to 20%, accordingly. That is, for an increase of set binder saturation from 10% to 20%, there was approximately 40% increase in compressive strength. This was due to the increased polymerized binder at grain contacts which lead to an increase in the bond forces. Furthermore, Hodder et al. (2018) noticed that for set saturations higher than 20%, the resolution of the prints started to diminish and the dimensional integrity of

the geometry of the specimens were at risk. This was attributed to the bleeding of the binder through the layers of sand. The binder accumulated at the bottom of the specimens and the distribution of the binder became heterogeneous. Based on the above investigations, which were conducted parallel to this study on sand analogues printed with the M-Flex printer, and the overall printing procedures were similar to the present study, a set binder saturation of 20% was chosen for building the specimens for the current research.

3.2.1.3 Layer orientation

It is possible to change the orientation of the building planes in the print bed such that the layer orientation of the printed samples would vary relative to the vertical axis of the samples. Gomez (2017) examined the effect of layer orientation on UCS strengths for samples printed with the M-Flex printer. The samples were prepared by mixing the sand with the activator and building the specimen in layers, with set binder saturation of 10%. However, the specimens were not cured after print. Cylindrical specimens with 0^o, 25^o, 45^o, 65^o and 90^o inclination with respect to the load application axis were fabricated and their uniaxial compressive strengths were compared. The size of the specimens was approximately 1.5 inch in diameter and 3 inch in height. The results showed that the average peak stress increased by 14% when the layers were perpendicular to the loading axis (90^o inclination) as opposed to parallel to it (0^o inclination). Gomez (2017) also stated that the failure modes changed from an inclined shear plane (for 90^o inclination samples) to a shear plane that was along the building planes (for 0^o inclination samples). This confirms that the printing process produces an anisotropic final product where the interlayer bonds are weaker than that of each layer. In the current study, to obtain consistency in the strength and deformation response of all the tests, the UCS cylindrical samples and the Brazilian disks were printed such that their layers were perpendicular to the vertical axis. A schematic illustration of layer orientation for a cylindrical UCS sample is given in Figure 3.3.

Figure 3.3. Schematic illustration of a cylindrical printed sample showing the orientation of the layers.

3.2.1.4 Curing process

Right after the samples are printed, because the binder has not crystalized fully, the samples are soft and need to be cured. Primkulov et al. (2017) mentioned that during the polymerization process, water builds up in the sample. This water, in later stages of curing, may reduce the mechanical strength of the sand analogues due to creation of macropores and ring hydrolysis of the monomers and therefore needs to be removed. One way to eliminate the water is by applying heat. The effect of curing temperatures on printed sand analogues were investigated by Primkulov et al. (2017). They used the same overall procedure to print the samples as the current study, that is combining the sand with the ExOne activator, printing the specimen in layers with the binder (mostly furfuryl alcohol), and curing the specimens in the oven. The samples were cured in the oven at 60°C, 80°C, 115°C, 150°C and 200°C. Once the samples were moved from the oven, they were cooled in room temperature. UCS tests were performed on cylindrical samples that were approximately 1 inch in diameter and 2 inch in height. The results are plotted in Figure 3.4.

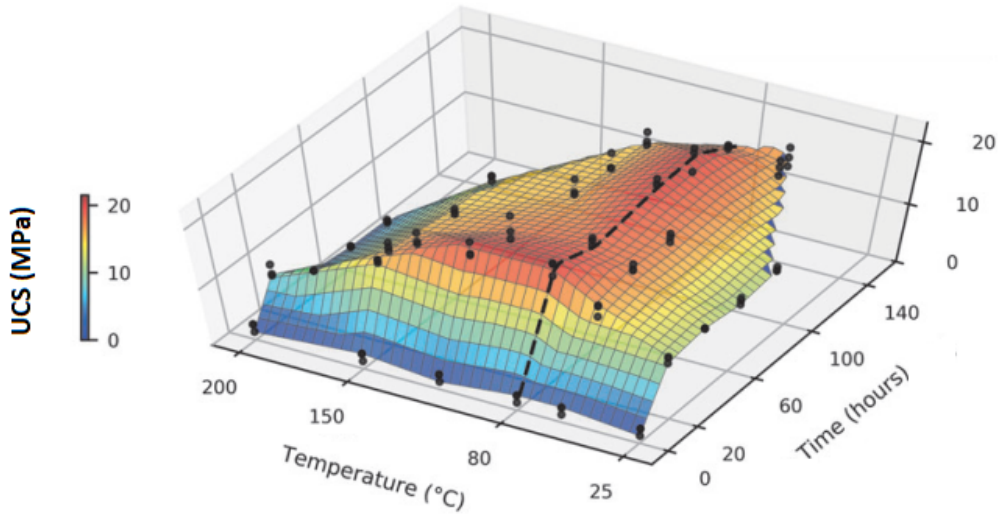

Figure 3.4. Plot of the UCS of printed samples as a function of curing temperature and time (modified from Primkulov et al., 2017).

This plot showed that the strength of the samples increased as the curing temperatures rose from 25°C to 80°C, revealing the highest strength at 80°C. They concluded that at this temperature, the water removal from the pore space was accelerated, yet keeping the integrity of the print. For temperatures above 100°C, the degradation of furfuryl alcohol was observed in the samples (Primkulov et al., 2017). Additionally, based on exposing the samples to thermal cycles of 80°C and 25°C, they concluded that the UCS of the prints will not be affected by exposure to the laboratory environment. This is due to strong bonds between the sand and resin (because of the organic nature of the acid and the existence of 3-aminopropyltriethoxysilane in the binder). Based on the findings of the stated study, for this research program, 80°C was chosen as the optimal temperature for curing the printed samples. They were cured at this temperature for 65 hours after print.

As mentioned previously, there was an option to apply heat to the samples when printing. Based on the effect that heat has on the crystallization of binder in the sand specimens and consequently on their mechanical strength, the effect of applying heat during the printing process was examined. For this, a heat arm installed in the printer was employed. The process was such that for each print layer, the recoater deposited the sand, the heat arm traversed the print bed

applying heat, then the printhead dispensed the binder. The layers were heated to approximately 40°C. At the end of the print, the samples were transferred to the oven and cured at 80°C for 65 hours, conforming to the same post-process as the samples that were not heat-cured during print.

3.2.2 Strength tests

UCS and Brazilian tests were carried out on cylindrical printed samples. Each sample was cleaned, and any remaining loose sand was brushed off prior to testing. Details of the tests and results are presented in the following sections.

3.2.2.1 UCS tests

UCS tests were conducted on the 400 kN INSTRON 5988 load system. Samples were placed on a fixed platen and an upper platen moved down applying load on the sample. The load and displacement data were recorded by a data logger. For these tests, cylinders with several dimensions were chosen. Smaller dimensions were chosen at first to comply with the parallel investigations taking place in our research group on 3D printed sand analogues. In the first sample set, cylindrical samples had 25.8 mm diameter and 51.3 mm height. The second sample set had cylinders with 38.6 mm in diameter and 76.9 mm in height. Both sample sets were prepared such that heat was applied during the printing process and then cured in the oven. The Young's modulus was calculated at 50% of peak axial stress. For the first sample set (average of 4 tests) the UCS value obtained was 33.1 MPa and the Young's modulus 2.68 GPa, and for the second sample (average of 3 tests, as one test was disregarded due to incorrect loading), the UCS was 39.5 MPa and Young's modulus was 2.90 GPa.

Ultimately, cylindrical samples with set diameter equals 54 mm and height of 135 mm were chosen. The first set of tests were conducted on samples with the heat-arm turned off, meaning no heat was applied to the samples during the printing process. For the second set, the heat-arm was turned on and heat was applied to each layer of print. UCS results for samples for the first set

(based on the average of 2 tests with 54.6 mm in diameter and 135.4 mm in height) and for the second set (based on the average of 7 tests with 54.6 mm in diameter and 135.7 mm in height) are depicted in Table 3.1. The UCS increased by 8% when heated during print. The axial stress-strain plots for the tests that were heated during the print and a photo of a sample after failure are illustrated in Figure 3.5. After the seating phase, the stress-strain curve exhibited a linear path followed by a nonlinear response up to peak stress. Failure was sudden, with large cracks forming across the sample.

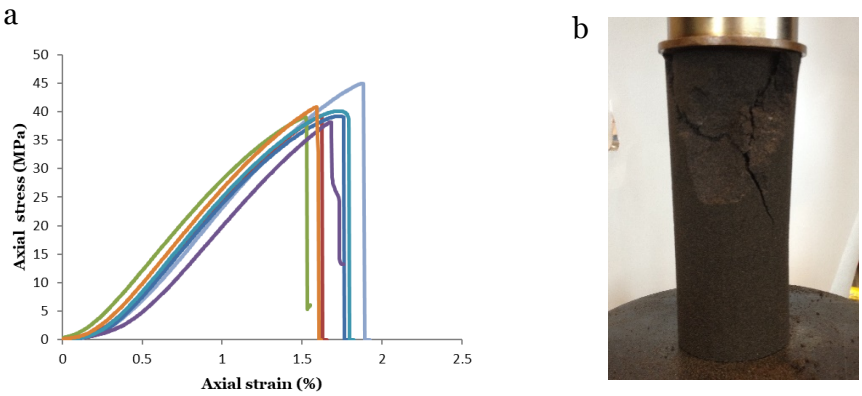

Figure 3.5. a. Axial stress versus axial strain for UCS tests b. sample after failure.

3.2.2.2 Brazilian tests

Brazilian tests were conducted on disk shaped samples using 150 kN INSTRON 3384 loading device. The samples were placed in a pair of GCTS loading jaws and compressed in the loading frame. The measured data was recorded digitally with the datalogger. The indirect tensile strength is obtained from Equation (3.1) (ISRM, 1978):

$$\sigma_t = \frac{2P}{\pi t D} \tag{3.1}$$

where P is the maximum applied load, t is the thickness of the disk and D is the diameter of the disk. As per the UCS tests, two sets were tested. The first set was only oven cured and the second set was heated during the printing process and oven cured. The test results for the first set

(average of 4 tests, diameter 54.7 mm and thickness 22.5 mm) and the second set (average of 6 tests, diameter 54.6 mm and thickness 22.2 mm) are shown in Table 3.1. The increase in tensile strength is roughly 7% for when the samples were also heated during the printing process. The failure patterns were similar in both events. The curves showed similar patterns of non-linearity due to sample seating at the start of the test, followed by a linear-elastic phase then nonlinearity near the peak shear stress. Once peak shear stress was reached, the samples failed which was visualized by a sudden drop in the stress curve.

Table 3.1. Compressive and tensile test results on printed samples

Test	No heat applied during print; oven cured	Heat applied during print; oven cured
UCS (MPa)	36.9	40.2
E (GPa)	2.75	3.27
Brazilian test (MPa)	6.9	7.4

Figure 3.6 illustrates the stress-displacement plots for the Brazilian tests carried out on the samples that were heated during the printing process along with a picture of the tested sample after failure.

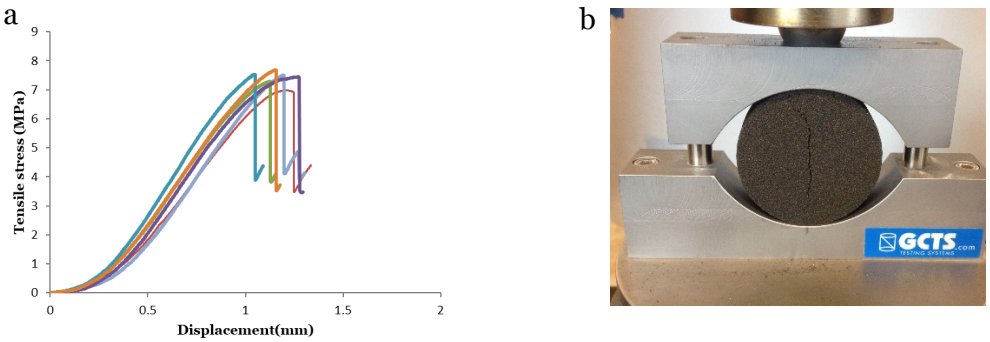

Figure 3.6. a.Tensile stress versus diametric displacement for Brazilian disk samples b. disk after failure.

3.2.3 Discussion

One of the objectives of this research is to study the feasibility of AM technology in creating rock replicas and to obtain higher compressive strengths. In this regard, the optimal printing process has to be selected. Based on the results of the strength tests in the previous section and because heating the print bed allows the polymerization of the binder to occur faster during printing and therefore impedes bleeding of the binder from the boundaries of the geometry, the method where heat is applied during the printing process then the samples are cured in the oven at 80^{o}c for 65 hours, was selected. Thus, from herein, the referred fabricated samples are prepared using this method which includes the specimens printed for direct shear tests.

3.2.3.1 Comparing 3D printed analogues to natural rock

Compared to other studies that fabricated rock analogues with powder-based 3D printed techniques, the values achieved for compressive strength in this study were much higher: approximately 4.9 times higher than values obtained by Jiang et al. (2016), approximately 10.6 times higher than values reported in Zhou and Zhu (2018) and approximately 9.2 times higher than the average UCS reported by Perras and Vogler (2019). This average UCS was obtained from averaging the unconfined compressive strength of 4 different specimens, namely the Voxeljet sand-furan, the ExOne sand-furan, the ExOne ceramic-silicate and the ExOne sand-silicate (Table 2.1). Among these, the samples built with the ExOne printer and the sand-furan composition, had the highest strength at 6.91 MPa (Table 2.1), thus the printed samples in the current research were approximately 5.8 times higher than the sand-furan composition by Perras and Vogler (2019). The reason is most likely that the ExOne sand-furan printed samples from Perras and Vogler (2019) were not heated and instead were cured naturally, as opposed to the specimens in the current study where the samples were heated during the printing process then heat-cured in the oven afterwards.

However, there are some discrepancies between the printed analogues and natural rock. In defining the characteristics of rock, the ratios of compressive strength to modulus and tensile strength to compressive strength are important. Deere and Miller (1966) classified intact rock based on their modulus ratio into three groups: class H (high modulus ratio) where the E/UCS > 500, Average, where 200<E/UCS<500 and class L (low modulus ratio) where E/UCS <200. The graph for elastic modulus versus UCS for sedimentary rock is plotted in Figure 3.7 (the graph is modified from Tatone, 2014). On this plot the data point representing the ratio for the 3D printed analogues along with the error bars are plotted. As shown, this ratio is below the average modulus ratio, classified as low modulus ratio.

Tatone (2014) created a classification based on the ratio of the indirect tensile strength (Brazilian tensile strength, BTS) and UCS of rock. In this classification, three groups were created: high, where UCS/BTS>20, average, where 8<UCS/BTS <20, and low, where UCS/BTS <8. The graph is modified and plotted in Figure 3.8, showcasing the range for different types of sedimentary rocks. For the sandstone rock, the data points are specifically drawn. The data point for the 3D printed analogues and the error bars are placed on the graph and as seen in the plot, the ratio of UCS/BTS for the printed samples is within the “low” category.

Perras and Diederichs (2014) also compared the relationship between BTS and UCS and found great scatter in the data from literature. However, they mentioned that the ratio of UCS/σ_t lies within the range of 4-32, in accordance with the Hoek-Brown m_i constant. Perras and Vogler (2019) edited the graphs provided by Perras and Diederichs (2014) to include only sandstones. This graph is shown in Figure 3.9 (for UCS of up to 200 MPa). The data point for the printed models from this research is drawn on this graph, which lies between the UCS/5 and UCS/10 lines.

The reason for the low ratios of E/UCS and UCS/BTS are likely due to the large pore space in the structure of the 3D printed analogues. Because the particle size distribution of the silica sand is uniform, the rock is not tightly packed and the binder exists between the sand grains contacts, leaving large pores between the grains. However strong bonds are created where the binder is crystallized between the sand contacts. Also, because the silica sand has a round morphology, the particle-particle contact is lower compared to a natural sandstone (Hodder, 2017).

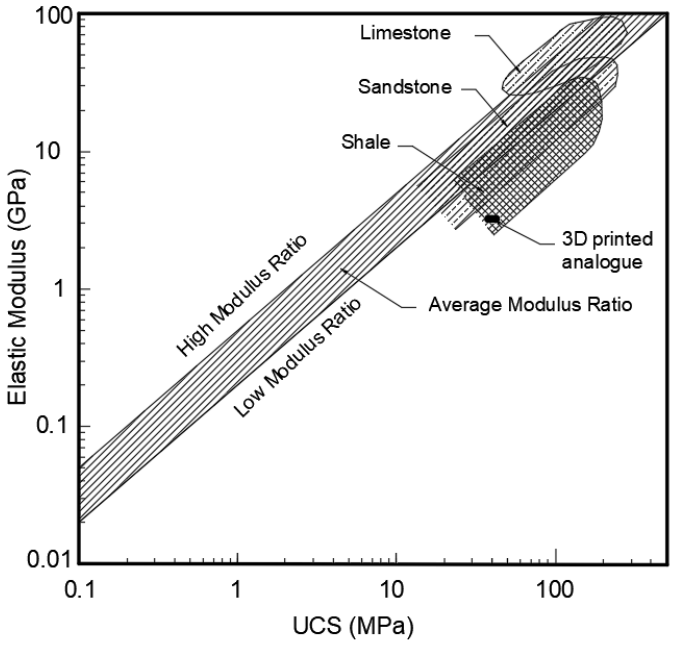

Figure 3.7.Placement of 3D printed rock analogues on the elastic modulus versus UCS chart, based on Deere and Miller (1966), modified from Tatone (2014).

As part of their investigations, Perras and Vogler (2019) studied the compressive and tensile strength of natural sandstones in Switzerland (Table 2.1). One of the sandstones studied was the Baerloch sandstone (from the Quarry Baerloch). Its mineral composition included 40-50% quartz, 20-40% feldspar, 10% calcite matrix and 10% layered silicates and other minerals and its strength parameters included UCS_{mean} = 53.11 MPa, E_{50mean} = 4.66 GPa and BTS_{mean} = 5.26 MPa. Based on these strength data, the 3D printed specimens in the current study are somewhat closer to the Baerloch specimens.

Of note is that to get a precise match between natural rocks and rock replicas, features such as true internal geometry (for example pore shape) and heterogeneous textures should also be considered. Ishutov et al. (2018) highlighted these and other challenges that exist to achieve accurate rock replicas using 3D printers.

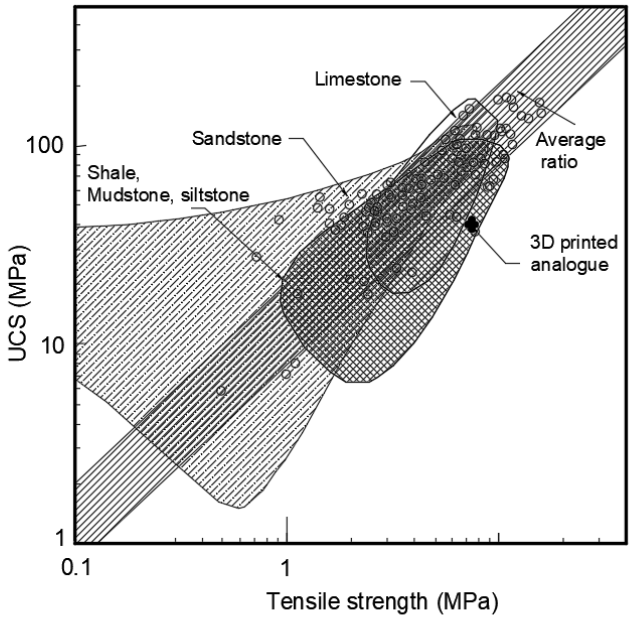

Figure 3.8. Placement of 3D printed rock analogues on the UCS versus tensile strength chart. The hallow circles represent sandstone data. Modified from Tatone (2014).

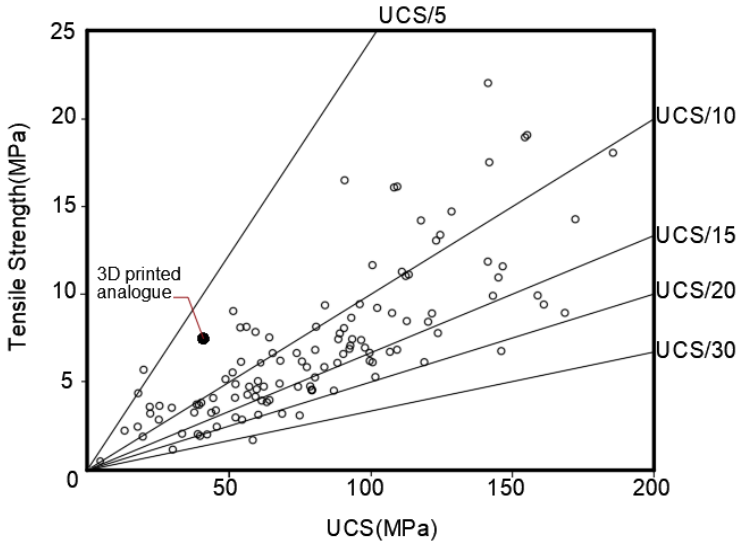

Figure 3.9. Placement of 3D printed rock analogues on the tensile versus UCS strength chart, modified from Perras and Vogler (2019). The original graph was presented in Perras and Diederichs (2014), but was later modified by from Perras and Vogler (2019) to show only sandstone data.

3.2.4 Additional post processing techniques

As mentioned in the previous sections, the 3D printed sand analogues have large porosities. One way to decrease porosity is to infiltrate the printed analogues with an alternative material, similar to Maleksaeedi et al. (2014). Therefore, as a first step, preliminary tests were devised to investigate the feasibility of the printed analogues to be infiltrated by an extraneous material.

For this purpose, epoxy resin (LECO, 811-563-107, MI, USA) was mixed with epoxy hardener (LECO, 812-521-HAZ, MI, USA) with a ratio of 5 to 1 by weight. The epoxy is clear therefore a green dye was added for colour. Disk-shaped samples were printed and placed in a container along with the epoxy resin. The container was placed under vacuum and the epoxy infiltrated the specimen. Results showed that the printed specimen was successfully infiltrated with the resin. Figure 3.10 illustrates a picture of a disk that was cut open after the it was partially infiltrated with the resin.

Figure 3.10. Infiltration of the printed disks with epoxy resin. The green part is where the dyed epoxy resin has infiltrated the specimen. The gray part is not yet infiltrated.

UCS and Brazilian tensile tests were conducted on the infiltrated specimens. The UCS tests were conducted on two cylindrical samples with average diameter of 25.8 mm and height of 51.2 mm. The axial stress vs. axial strain for the tests is depicted in Figure 3.11a. From this it was seen that even though the average maximum stress increased considerably (approximately by a multiple of 3), however, the response was no longer brittle, and the sample was bulging in the middle.

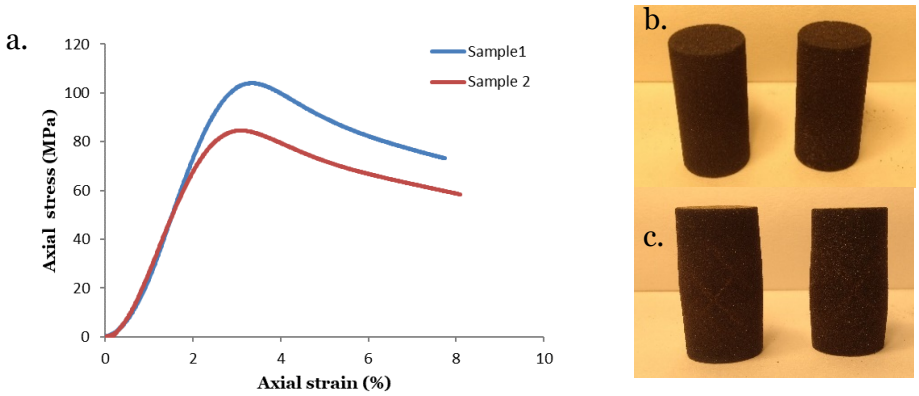

Figure 3.11. UCS tests on printed samples infiltrated with epoxy: a. axial stress versus axial strain b. samples before failure c. samples after failure.

The same trend was seen for Brazilian tests on two disks (average diameter of 54.4 mm and thickness of 22.1 mm) in Figure 3.12a, where the disks continued to gain strength after the initial failure in the tensile stress vs. displacement curves. The disks were flattened after failure which is shown in Figure 3.12b.

Based on these results, it is concluded that the printed specimens can be infiltrated with external material to decrease porosity and increase strength. However, more investigation is needed to adopt material such as cement or concrete, that would result in a stronger specimen and behave in a brittle manner, resembling natural rock.

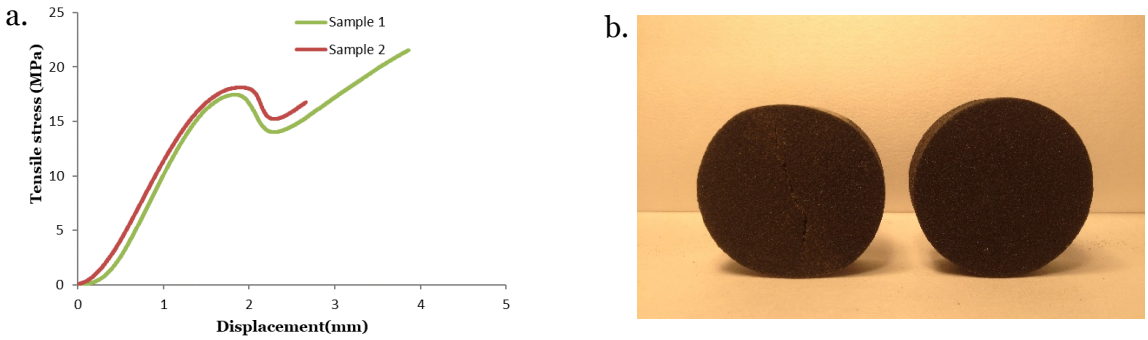

Figure 3.12. Brazilian tests on printed samples infiltrated with epoxy: a. tensile stress versus diametric displacement b. sample after failure (on the left) compared to the sample before testing (on the right).

3.3 Fracture surfaces

In this section, the response of the 3D printed specimens printed with the M-Flex sand printer is studied in direct shear. The printing process is based on the optimized process in the previous sections, i.e., 20% binder saturation, heat-cured during print and post processed for 65 hours in the oven at 80^{o}C. The investigated geometries include triangular asperities with 15-, 30- and 45-degrees slopes, and standard profiles by Barton and Choubey (1977) with JRC equal to 6-8, 12-14 and 18-20. The shear stress and dilation versus horizontal displacement, the strength envelopes, and the failure mechanism of the above fabricated specimen are explored in direct shear tests in this section. The results are compared with typical rock behaviours.

3.3.1 Direct shear apparatus

The shear tests were carried out using the GCTS RDS-100 direct shear apparatus. This system has the capacity to apply maximum normal load of 50 kN and maximum shear load of 100 kN. These loads are applied via ISCO pumps. The normal load is applied to the center of the upper shear box. The shear load is applied to the upper shear box while the lower shear box is fixed. Two Linear Variable Displacement Transducers (LVDTs) measure the vertical and horizontal displacements. This apparatus can conduct tests under the ISRM suggested method for laboratory shear tests (Muralha et al., 2014). Figure 3.13 shows the direct shear apparatus. The testing machine could run tests under constant normal load (CNL) conditions. It was later modified to incorporate constant normal stiffness (CNS) boundary conditions (Chapter 4).

3.3.2 Direct shear tests

The strength and deformation response of printed triangular joints and standard profiles were investigated under various applied normal loads. The shearing rate for the tests was 0.1 mm/min.

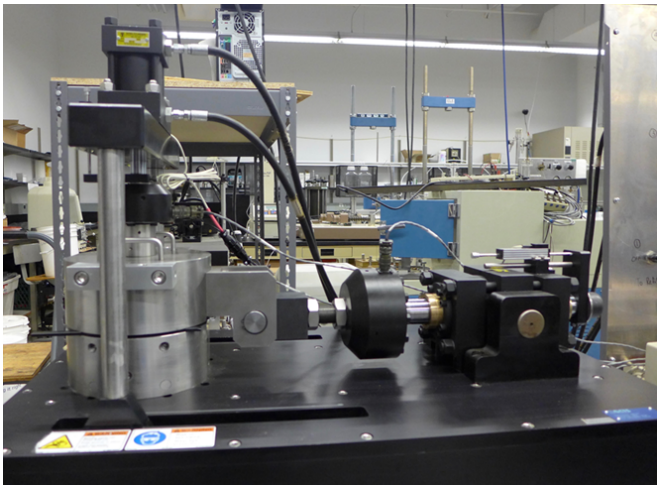

Figure 3.13. The direct shear apparatus.

3.3.2.1 Triangular joints

A total of 6 triangular joint samples were printed and tested. Each sample had a triangular asperity with base length of 20 mm placed in the center of the specimen. Three triangular joints were printed with asperity slopes of 15, 30 and 45 degrees (Figure 3.14). Shear tests were performed on these specimens under applied normal stresses of 0.125 MPa and 0.5 MPa. Figure 3.15 illustrates the shear stress and normal displacement versus shear displacement for these tests. Results indicated that with the decrease of asperity angle from 45° to 15°, the peak shear stress decreased, and so did the dilation magnitude. Furthermore, by applying a higher normal stress, i.e., 0.5 MPa, the peak shear stress increased. The post peak response changed from brittle for the 45° asperity to a more ductile response for the 15° asperity, cueing different failure mechanisms.

Visual inspection of the specimens showed that during the tests, the upper joint half rode up the lower half (Figure 3.16a and Figure 3.17a) resulting in the dilation of the joints. After the tests ended, signs of failure were apparent on the surface of the joints. For the asperities with 15 and 30 degree angles, under both normal stresses, whitish-gray areas were seen, indicative of the sand that had sheared off (Figure 3.16b, Figure 3.16c, Figure 3.17b, Figure 3.17c). The damage

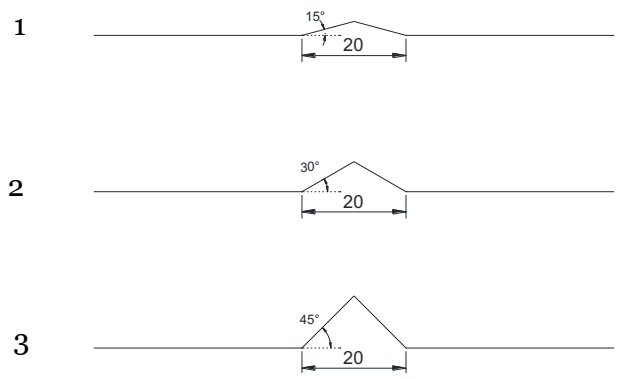

Figure 3.14. Geometry of the triangular joints with 15°, 30° and 45° angles for direct shear tests.

was located on the surface opposing the shear direction and especially concentrated on the edge of the asperity. Lindenbach and Bearce (2018) also noticed the damage was concentrated on the ridge for hydrostone saw-tooth samples. For these asperities no visible cracks were noticed. For the 45-degree angle triangular joint, failure occurred through the intact rock. When the asperity was sheared under 0.125 MPa applied normal stress, an inclined crack formed in the asperity (Figure 3.18a) and when it was sheared under 0.5 MPa applied normal stress, after about 2.5 mm of shear displacement, the asperity was sheared horizontally and was cut off entirely (Figure 3.18b). A steep decline in shear stress was witnessed in the shear stress vs. shear displacement graph (Figure 3.15).

The objective of this section was to adopt 3D printed joints with simple geometry to compare with rock behaviour in direct shear tests. From the above results it is concluded that the overall shear behaviour of the 3D printed material is typical of rock joint replicas.

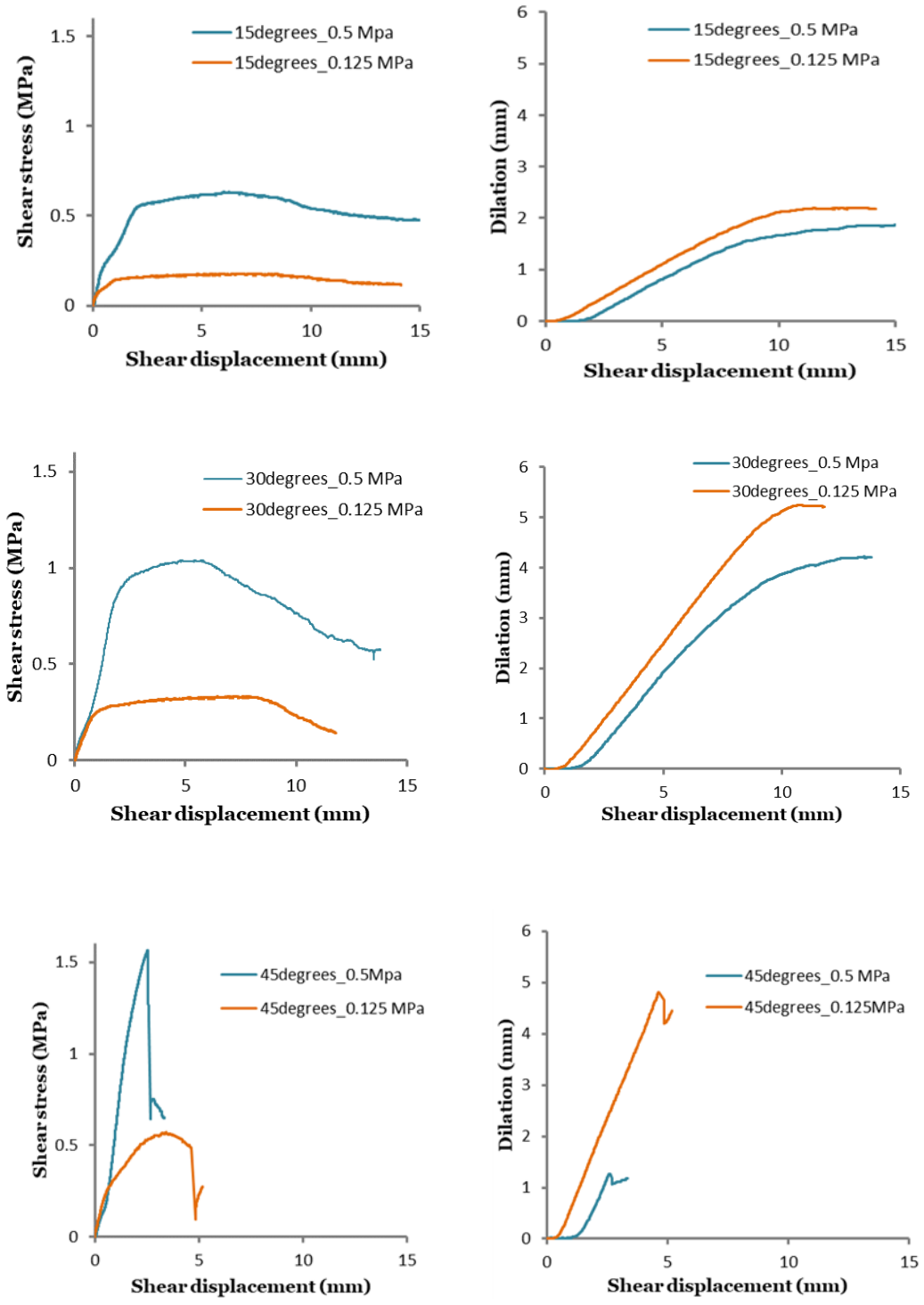

Figure 3.15. Shear stress and dilation vs. shear displacement for triangular asperities under 0.125 MPa and 0.5 MPa applied normal stress.

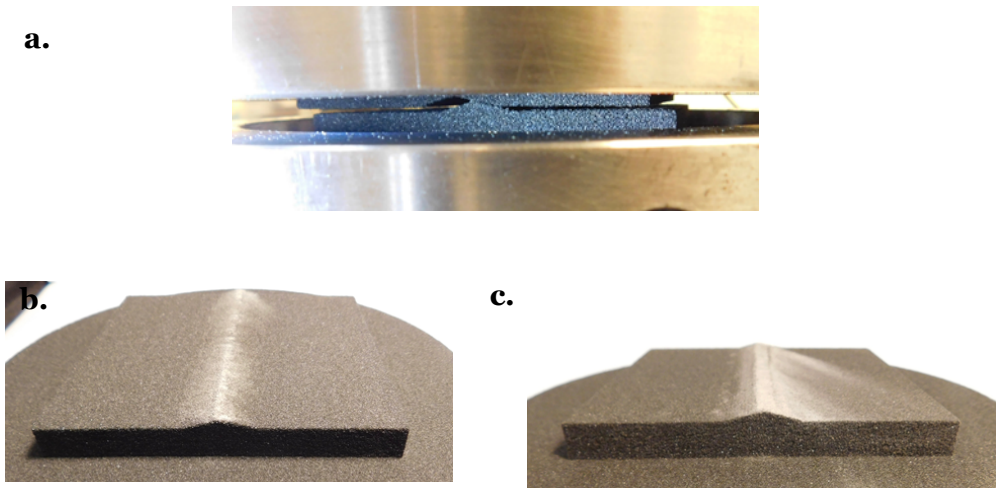

Figure 3.16. Triangular joint with 15^{o} inclination: a. during shear in the shear box b. after shear, under 0.125 MPa normal stress c. after shear, under 0.5 MPa normal stress; areas with whitish-gray sand is indicative of failure.

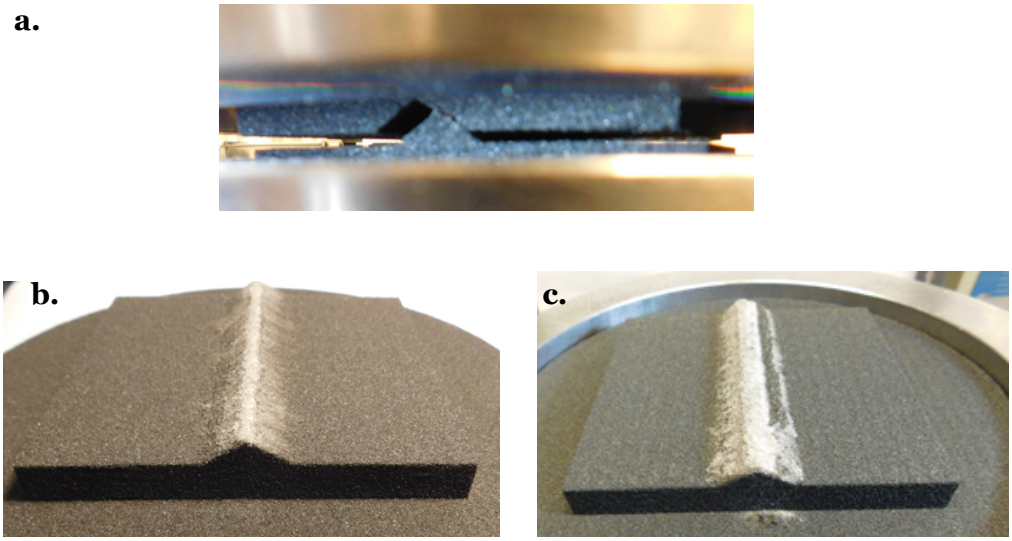

Figure 3.17. Triangular joint with 30^{o} inclination angle: a. during shear in the shear box b. after test, for joint under 0.125 MPa applied normal stress c. after test for joint under 0.5 MPa applied normal stress. Notice the increase in loose sand in the failed areas under 0.5 MPa.

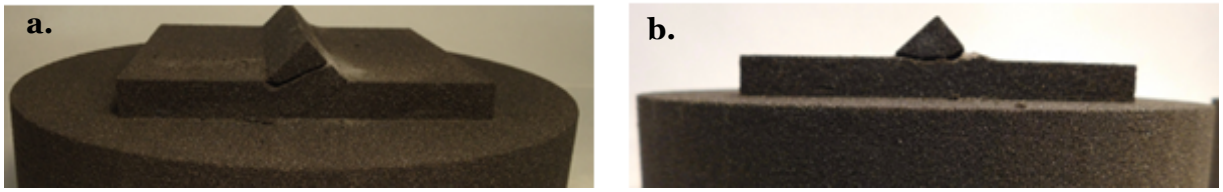

Figure 3.18. Failure patterns observed in triangular joints with 45° inclination angle: a. under applied normal stress = 0.125 MPa b. under applied normal stress = 0.5 MPa.

3.3.2.2 Standard Profiles

Three standard joint profiles from Barton and Choubey (1977) representing various surface roughness were chosen and direct shear tests were conducted in constant normal load conditions. The roughness profiles included joints with JRC = 6-8, JRC = 12-14 and JRC = 18-20. The range of applied normal stress was between 0.25 MPa to 1 MPa. For profiles with JRC=18-20, two additional tests under 1.5 MPa and 2.5 MPa applied normal stress were performed. In total, 11 samples were fabricated and tested. Figure 3.19a illustrates the upper and lower joint surface with JRC=18-20 and Figure 3.19b shows the lower joint surface assembled in the shear box prior to shearing. The shear stress and dilation versus shear displacement results of the tests on these joints are depicted in Figure 3.20, Figure 3.21 and Figure 3.22.

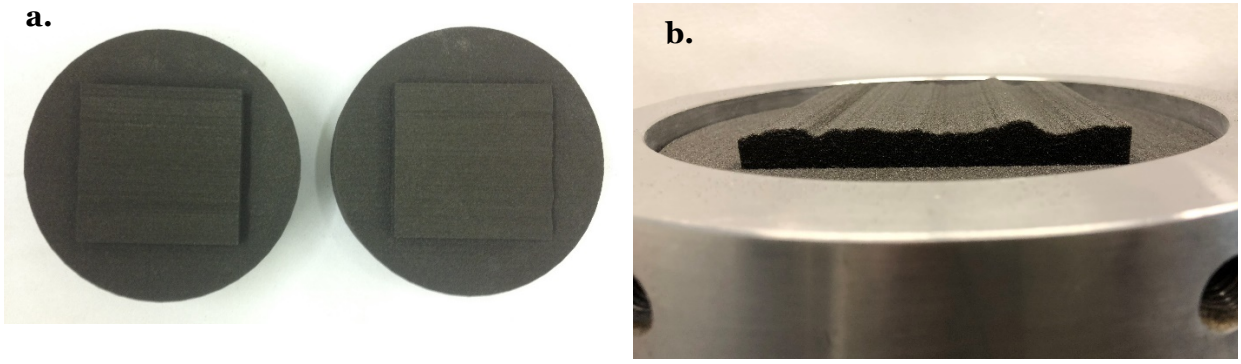

Figure 3.19. Printed joints with JRC= 18-20: a. upper and lower halves b. lower joint surface placed in the shear box.

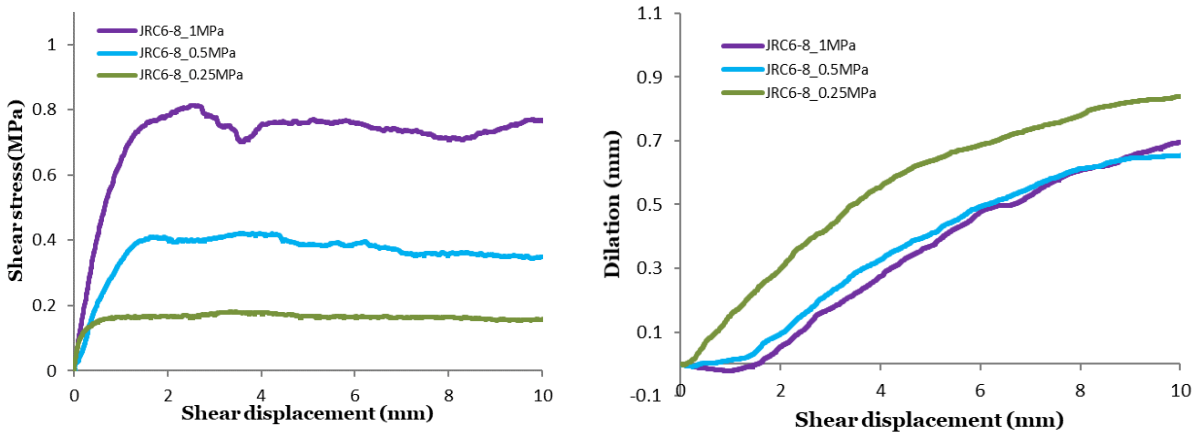

Figure 3.20. Shear test results on joints with JRC=6-8 under applied normal stress of 0.25 MPa, 0.5 MPa and 1 MPa: shear stress vs. shear displacement and dilation vs. shear displacement.

In the beginning of all the tests, in the stress plots, the shear stress increased in a linear elastic manner. This is explained by Archambault et al. (1997) and Tatone (2014) as the phase that the increase of shear stress causes the transfer of stresses on the asperities opposing the direction of shear thus leading to an increase in localized normal stress.

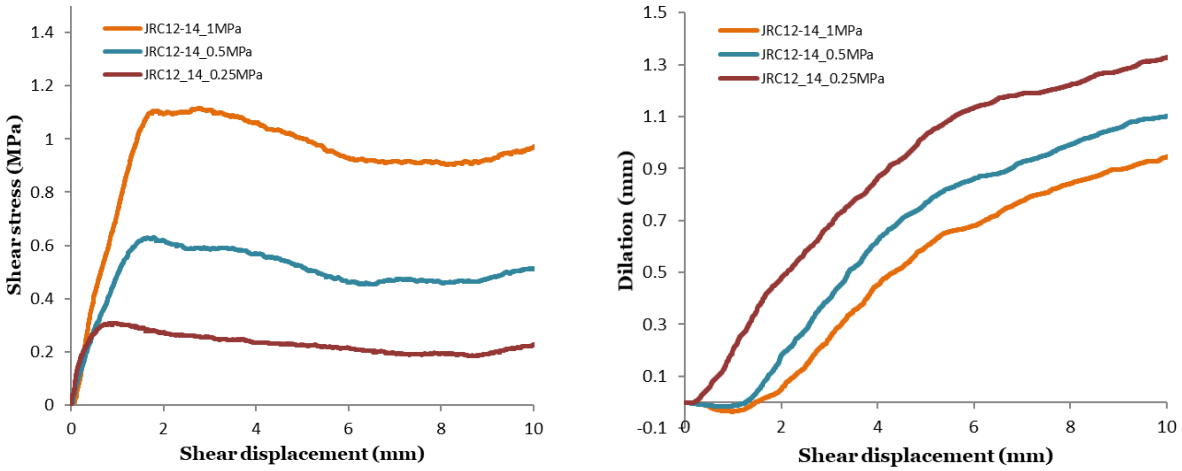

Figure 3.21. Shear tests on joints with JRC=12-14 under applied normal stress of 0.25 MPa, 0.5 MPa and 1 MPa: shear stress vs. shear displacement and dilation vs. shear displacement.

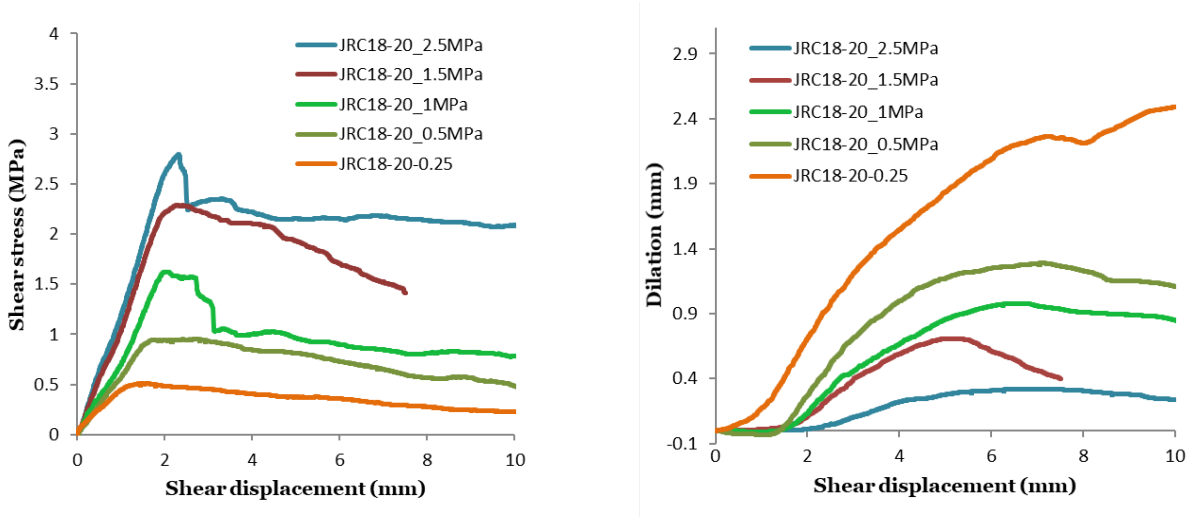

Figure 3.22. Shear tests on joints with JRC=18-20 under applied normal stress of 0.25 MPa, 0.5 MPa and 1 MPa, 1.5 MPa and 2.5 MPa: shear stress vs. shear displacement and dilation vs. shear displacement

They further mentioned that the increase in the normal stress causes the increase of frictional resistance and the mobilization of the shear stiffness. This is followed by sliding of the upper asperities on the lower ones and the decrease in the contact area, which leads to the increase of the localized normal stresses and hence the increase of the frictional resistance. Dilation is occurring during this phase. The degradation of the joint surface was observed as wear, abrasion or cracking of the asperities. Gradually the peak shear strength is reached followed by post peak softening, which is due to damage and degradation of the asperities. The above phases mentioned by Archambault et al. (1997) and Tatone (2014) were observed in the shear tests on the printed joints. For the joint surfaces that had similar asperity roughness, the increase in applied normal stress was associated with a decrease in dilation and more brittle post peak behaviour. For the joint profile with JRC=6-8 (Figure 3.20) the increase in peak shear stress under 0.5 MPa and 1MPa applied normal stress was 134% and 350% with respect to an applied normal stress of 0.25 MPa. Furthermore, at the start of the tests, the joints contracted which is shown by the negative normal displacement in the dilation plots. This is seen in many laboratory tests on rocks and is the result of the interaction of shear and normal loads (Archambault et al, 1997). The two halves

of the joint surface after shear for JRC=6-8 are depicted in Figure 3.23. The white areas show the asperities that were damaged the most.

For the joint with JRC 12-14 (Figure 3.21), the stress-displacement curves had similar shapes for the various applied normal stresses, however the post peak response for the test with applied normal stress of 1 MPa was more brittle. The increase in shear stress was 104% to 262% from 0.25 MPa to 0.5 MPa to 1 MPa applied normal stress. For the joint surface with JRC 18-20 (Figure 3.22), the peak shear stress increased with the increase of normal stress from 0.25 MPa to 2.5 MPa, by 447%. The peak shear displacement was approximately between 2-3% of the length of the samples.

The results of all the shear tests on standard roughness profiles conducted under normal stresses of 0.25 MPa, 0.5 MPa and 1 MPa are illustrated once more on the same plot in Figure 3.24. The purpose is to compare the effect of asperity geometry and roughness on shear strength and normal deformation. Results indicated that, as expected, for a similar applied normal stress, there is a positive correlation between roughness (JRC value) and peak shear strength and

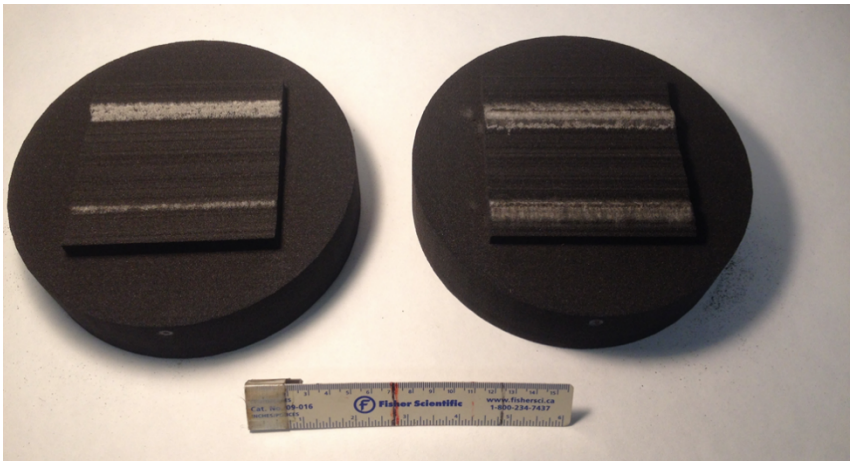

Figure 3.23. Upper and lower joint surfaces with JRC=6-8 after shearing. The white areas show the extent of the damage.

dilation. Also, for each standard profile, peak shear displacement was lower for lower applied normal stresses. Moreover, the post peak response became more brittle for rougher joint surfaces.

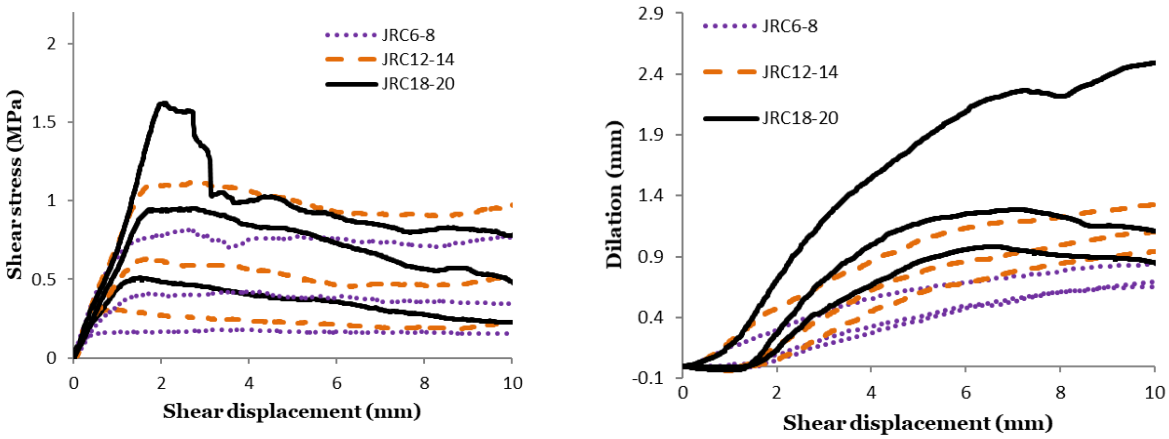

Figure 3.24. Accumulation of stress and dilation curves in one graph to compare the effect of roughness on shear stress and dilation response.

Comparison of 3D printed shear tests with Barton-Bandis model

The direct shear test results of the printed standard profiles are compared with the empirical Barton-Bandis shear model (Barton and Choubey, 1977). For JCS, the unconfined compressive strength was used (40.2 MPa). To attain the value of basic friction, planar surfaces were printed. The flat surfaces were then tested in direct shear under 0.25 MPa, 0.5 MPa and 1 MPa applied normal stress. The shear load versus shear displacement charts are illustrated in Figure 3.25.

It should be noted here that some previous studies have questioned the accuracy of the basic friction attained using saw-cut surfaces, stating that the minor textural variations affect the values obtained for basic friction (e.g., Hencher and Richards, 2015). Nevertheless, based on the repeatability of the 3D printed rock proxies, the basic friction of the printed material was obtained by the conventional method of shearing planar surfaces in the direct shear apparatus. Based on these tests, the basic friction coefficient was obtained to be 0.57.

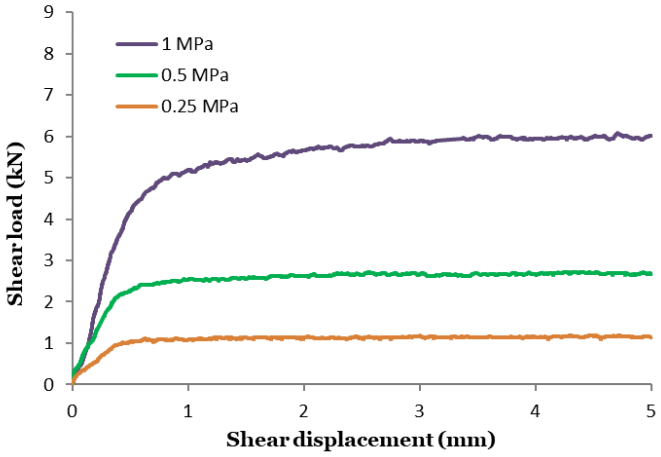

Figure 3.25. Shear test results for printed flat surfaces.

The peak shear strength versus applied normal stress of the joint surfaces is plotted in Figure 3.26 (for JRC=6-8 and JRC 12-14) and Figure 3.27 (for JRC =18-20). As illustrated in these plots, in general, the peak shear stresses of the sand proxies agree with the Barton-Bandis model, however the experimental results are slightly underestimated compared to the shear criterion. This becomes more obvious for JRC =18-20 at 2.5 MPa applied normal stress, where the experimental result appears to deviate from the model.

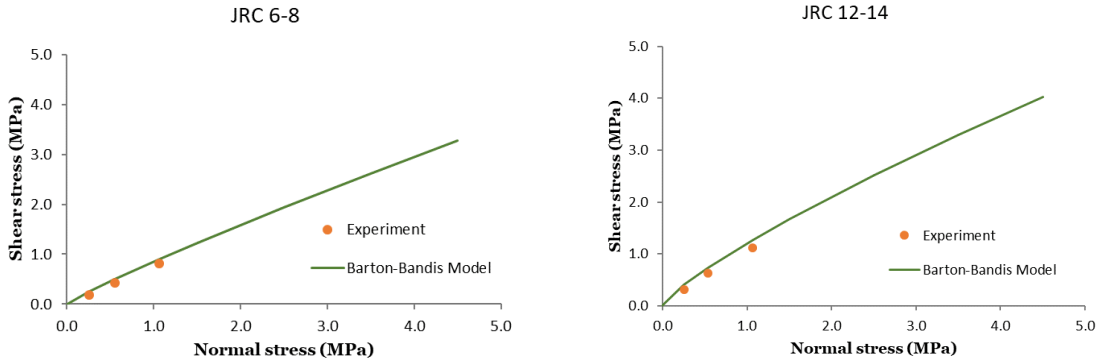

Figure 3.26. Comparison of peak shear stress measured in laboratory for joints with JRC=6-8 and JRC=12-14 with the Barton-Bandis shear criterion.

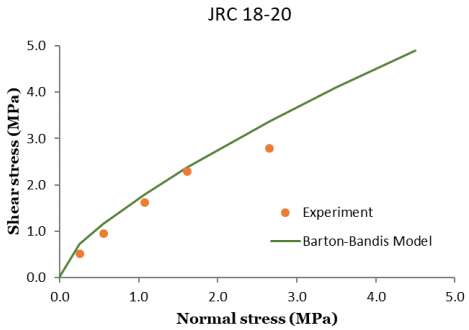

Figure 3.27. Comparison of peak shear stress measured in laboratory for joints with JRC=18-20 with the Barton-Bandis shear criterion.

This could be because of the high porosity of the 3D printed material (as explained previously), where under higher normal loads the asperities collapse. Nevertheless, from the results obtained in this section, it is concluded that in general, the 3D printed joint surfaces can be used to represent natural rock-like surfaces in direct shear.

3.3.3 Repeatability

To examine the repeatability aspect of 3D printed samples, direct shear tests were conducted on two sets of printed joint samples in CNL conditions. In the first set, direct shear tests under 0.125 MPa applied normal stress were carried out on two printed triangular asperities with inclination angle of 15^{o}. In the second set, three joints with JRC=18-20 under 1MPa applied normal stress were tested. The results of the triangular asperities are shown in Figure 3.28 and Figure 3.29 shows the results on the joints with JRC=18-20. For the triangular joints the dilation is depicted until approximately 8 mm of shear, because in one of the tests there was a problem detected in the normal LVDT after 8 mm of shear. For the triangular joints, the stress- dilation curves are nearly identical and for the JRC=18-20, even though after peak shear stress, the shear stress and dilation are slightly higher for replica 3, these results showed that overall, the 3D printer can produce repeatable test specimens.

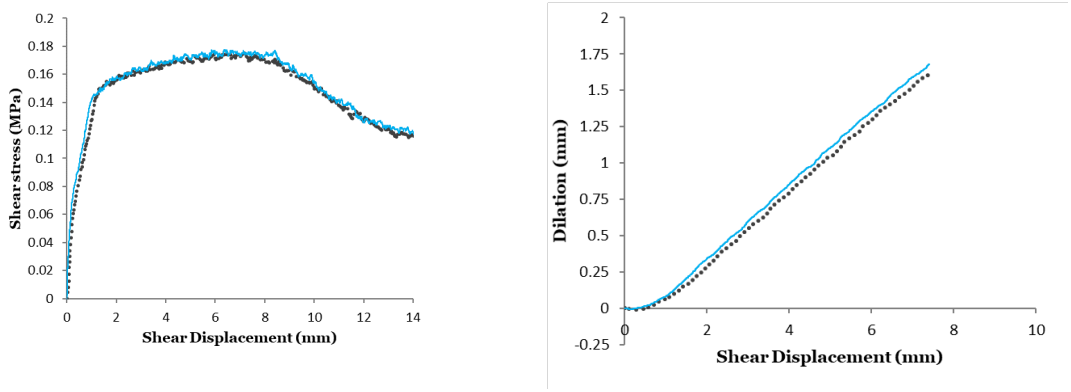

Figure 3.28. Comparison of direct shear tests conducted on two joint profiles with the same roughness, i.e. triangular joints with 15° inclination, under 0.125 MPa applied normal stress.

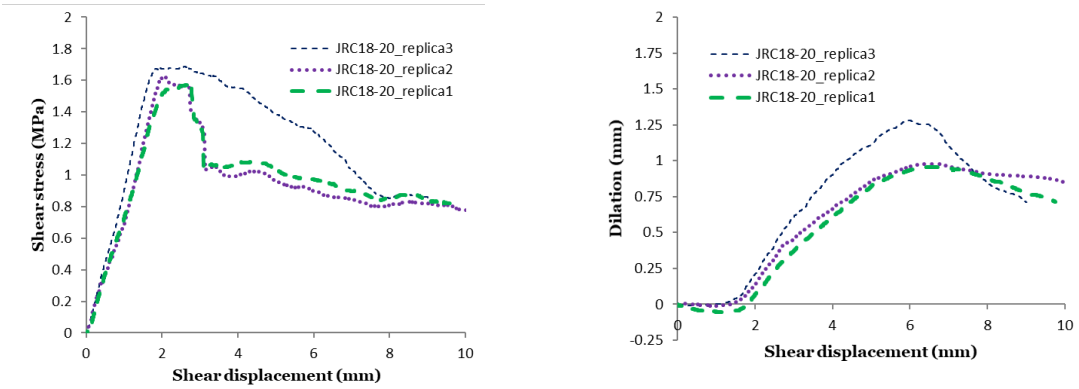

Figure 3.29. Comparison of direct shear tests conducted on three joint profiles with the same roughness, i.e., JRC=18-20, under 1 MPa applied normal stress.

3.3.4 Using the FDM process in additive manufacturing

For completeness, and to integrate additive manufacturing technology with the conventional methods used to replicate rock, in this section the use of 3D printing to fabricate molds for rock joints is investigated briefly. For this purpose, a desktop 3D printer i.e. the LulzBot TAZ 4 3D printer, that was readily available and cost-effective was used.

LulzBot TAZ 4 3D printer employs Fused Filament Fabrication (FFF)[1], also known as the fused deposition modeling (FDM) process, where a thermoplastic strand, the filament, is heated, forced through an extruder and deposited in layers to create the desired geometry. Two printheads were incorporated for this printer: The TAZ 4 Single Extruder Tool Head, which was able to print with the polylactic acid (PLA) filament; and the TAZ Flexystruder Tool Head v2, that was capable of printing with flexible filaments. The Cura LulzBot Edition v.21.04 software was used to control the TAZ 4 printer. Gypsum cement (Hydro-Stone Gypsum Cement, USG, USA) was then used to produce the joint replicas.

To test the capability of the FFF technology in creating rock replicas, molds for a joint with JRC=18-20 was printed, and the joint surface was cast using gypsum cement. Using the PLA filament with the Single Extruder Tool Head, first, a mold for the joint was printed in one piece (Figure 3.30a). Because the PLA filament is brittle, the resulting print was a rigid body, therefore removal of the casted cement was not accomplished easily. Hence, another mold was printed with the same material but in three separate parts (Figure 3.30b). This time, the extraction of the casted cement was easier, however there were some inconveniences such as leaking of the liquid cement from the spaces in between the individual parts. For the molds printed with the PLA material, the integrity of the print was examined visually, and it showed that although the asperities of the joint geometry were intact, there were some additional patterns inserted on the asperities (Figure 3.31). These unwanted patterns were formed by the nozzle of the printhead when the filament was being extruded during the print. For comparison, a mold was also fabricated with the M-Flex printer using sand (Figure 3.30c).

To make the extraction of the cast cement easier without having a leakage problem, a flexible mold was printed. For this, the printhead was replaced with the TAZ Flexystruder Tool

[1] https://www.lulzbot.com/store/printers/lulzbot-taz-6/specifications#

Head. NinjaFlex filament, which is a flexible filament, formulated from a thermoplastic polyurethane (TPU) material was used as the printing material. The mold was printed in one piece (Figure 3.30d). Because the resulting mold was flexible, removing the casted cement was easily accomplished.

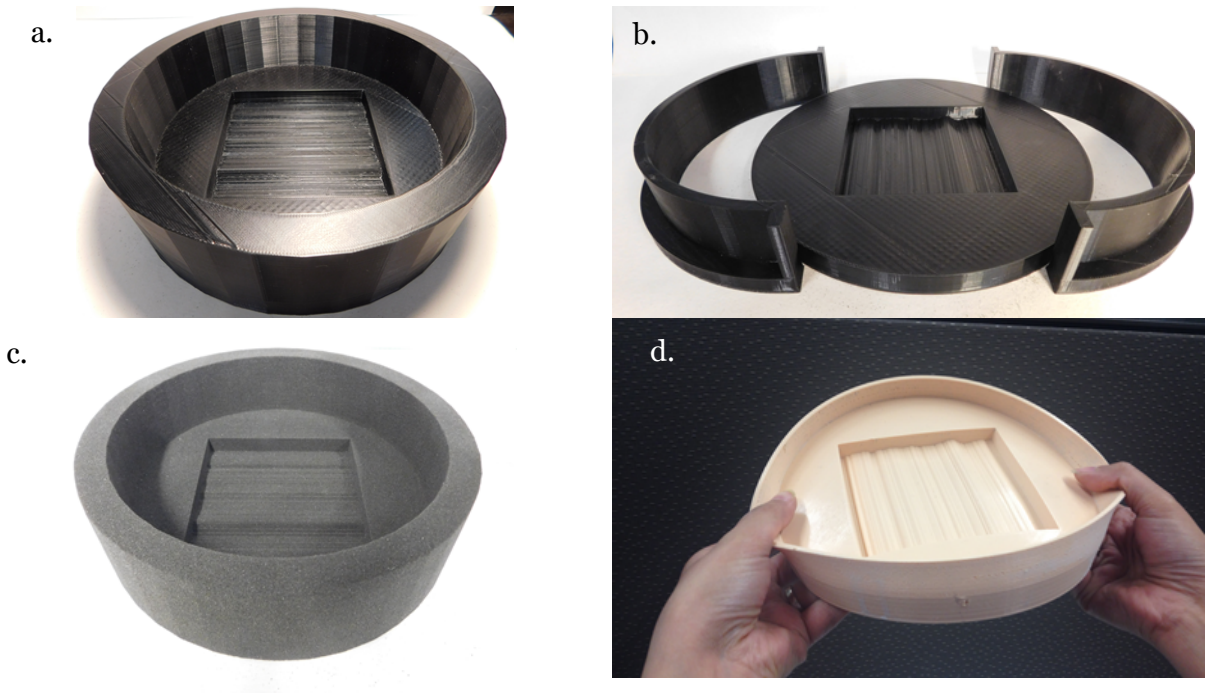

Figure 3.30. 3D printed molds for joint with JRC = 18-20: a. mold printed in one piece using PLA b. mold printed in 3 pieces using PLA to make the extraction easier c. mold printed with sand using the M-Flex printer d. mold printed with flexible filament.

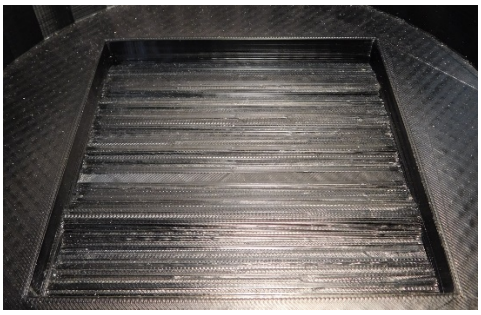

Figure 3.31. Unwanted patterns observed on the printed material when using the PLA filament.

Also, based on visual inspections, there were less intrusions from the printhead and the asperities were “cleaner”. The printing temperature for the Flexystruder was set to 230°C and the bed temperature was set to 25°C. The print speed was 10 mm/s which was 5 times slower compared to the print speed when using the PLA material. A picture of the printhead and the cast joint made with the printed flexible mold is shown in Figure 3.32.

a. b.

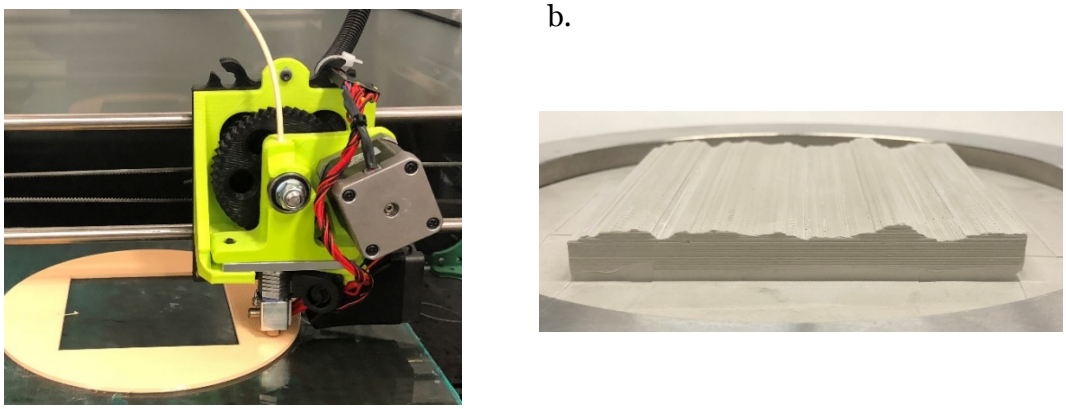

Figure 3.32. a. Flexystruder Tool Head for the TAZ 4 printer b. Joint created with gypsum cement with JRC 18-20 cast in mold printed with the Ninjaflex flexible filament.

Working with 3D printers became challenging at times. One of the frequent problems encountered while printing with the Flexystruder was the extrusion of the filament. The insufficient extrusion lead to a stringy print (shown in Figure 3.33). This problem was solved either by adjusting the printing temperature or by cleaning the nozzle. If these methods were insufficient, the nozzle needed to be replaced. Based on the above observations, it is concluded that the FFF technology and printing with the flexible filament are suitable alternatives for creating molds for rock joint replicas, however more investigations are needed to ensure the integrity of the cast material in these molds for direct shear tests.

Figure 3.33. Stringy print encountered when printing with the Flexystruder printhead.

4 Understanding the effect of geometry components on joint shear behaviour using 3D printed sand analogues in CNL and CNS conditions

4.1 Introduction

The anisotropy of joint roughness plays a prominent role in the shear behaviour of discontinuities. Several approaches are used to describe anisotropy, among them are statistical parameters and empirical approaches such as standard profiles (JRC). Furthermore, the importance of executing representative field stress conditions especially constant normal stiffness conditions in laboratory tests has been emphasized in literature (e.g., Jiang et al., 2006, Indraratna et al., 2015). The objective of this chapter is to investigate further the geometrical components that contribute to surface roughness and therefore effect the shear response of joints in constant normal load (CNL) and constant normal stiffness (CNS) boundary conditions.

For this purpose, in the first section, seven triangular-tooth profiles were chosen, and direct shear tests were conducted on them. In the second section, the use of standard JRC profiles in predicting the shear response of 3D printed rock joints is investigated. In this regard, new geometries were configured by rearranging the standard profiles and they were tested in direct shear. All shear experiments were conducted in CNL and CNS conditions. For implementing CNS boundary conditions, the GCTS direct shear machine was modified to accommodate this condition. The analysis was done using the sand proxies that were printed with the M-Flex 3D printer with 20% binder saturation. Heat was applied during printing and the samples were post-processed in the oven for 65 hours at 80^{o}C.

4.2 Modifying the direct shear testing machine

The shear tests were carried out using the GCTS RDS-100 direct shear apparatus. The testing machine could run tests under constant normal load (CNL) conditions. To conduct tests under constant normal stiffness (CNS) conditions, the system was modified using LabVIEW (National Instrument Co., Ltd.) to implement a normal stiffness. The LabVIEW code was written in collaboration with Victor Zhao, and then later modified by Les Dean. Based on Equation (4.1) (Porcino et al., 2003), the normal stiffness is defined as the change in normal stress divided by the change in normal displacement.

$$\mathrm{k_n} = \frac{\Delta\sigma}{\Delta\mathrm{u}} \rightarrow \Delta\sigma = \mathrm{k_n}\Delta\mathrm{u} \rightarrow \sigma_t - \sigma_0 = k_n \Delta u \tag{4.1}$$

where k_n is the normal stiffness, $\Delta\sigma$ is the change in normal stress, Δu is the change in vertical displacement, σ_t is normal stress at time t, and σ_0 is the initial normal stress applied on the sample. The change in normal displacement is measured with the normal LVDT and based on the chosen normal stiffness, the change in normal stress is calculated from Equation (4.1) and applied with the ISCO pumps on the sample. To avoid an overshoot on the normal load applied on the specimen, the rate of change of the normal pump pressure was controlled. Based on trial tests on several specimens, a suitable rate of change was chosen and entered in the user interface. Several tests were carried out on the printed sand samples to verify that the LabVIEW code was performing correctly. Figure 4.1 displays the response of the modified direct shear apparatus for tests with two different normal stiffnesses. Normal stress vs. vertical displacement is plotted for a triangular profile, i.e., profile 1 (defined in the next section). The slope of each graph is consistent with its equivalent applied normal stiffness.

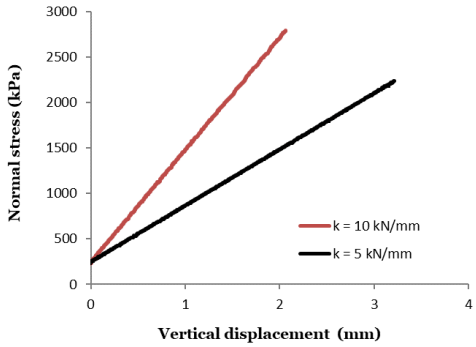

Figure 4.1. Response of the modified direct shear apparatus, displaying the trend of normal stiffness in CNS tests.

4.3 Triangular profiles

4.3.1 Geometry and test configurations

Seven triangular-tooth profiles were selected. These profiles differed from one-another in shape, height and directionality of joint asperities. Figure 4.2 shows the geometry of the profiles. Profiles 1-6 have the same slope angles in the direction of shear, i.e., 30 degrees. Profile 7 is the reversal of profile 6 and has a slope of roughly 44 degrees in the direction of shear. The profiles were extended through the width of the profile to make rectangular shaped samples. The length and width of the profiles are 80 mm and 100 mm respectively. The base length of each triangular tooth varies; profiles 1 and 2 have a base length of 20 mm; profiles 3, 4 and 5 have 10 mm base length; profile 6, and 7 have a base length of 16 mm. Profile 4 has a horizontal unit as well. The profiles were chosen such that the total length of the profile remains the same for all the joints. Table 4.1 depicts the statistical parameters calculated for each of the profiles. Direct shear in CNL and CNS boundary conditions were performed on the specimens. The normal stress applied to the joint samples for the CNL tests was 0.25 MPa. This was also the initial normal stress applied in the CNS tests. The stiffness applied in the CNS tests was k= 5 kN/mm. For profile 1, additional

tests were run which included CNL tests under 0.5 MPa and 1 MPa applied normal stress also a CNS test under k=10 kN/mm.

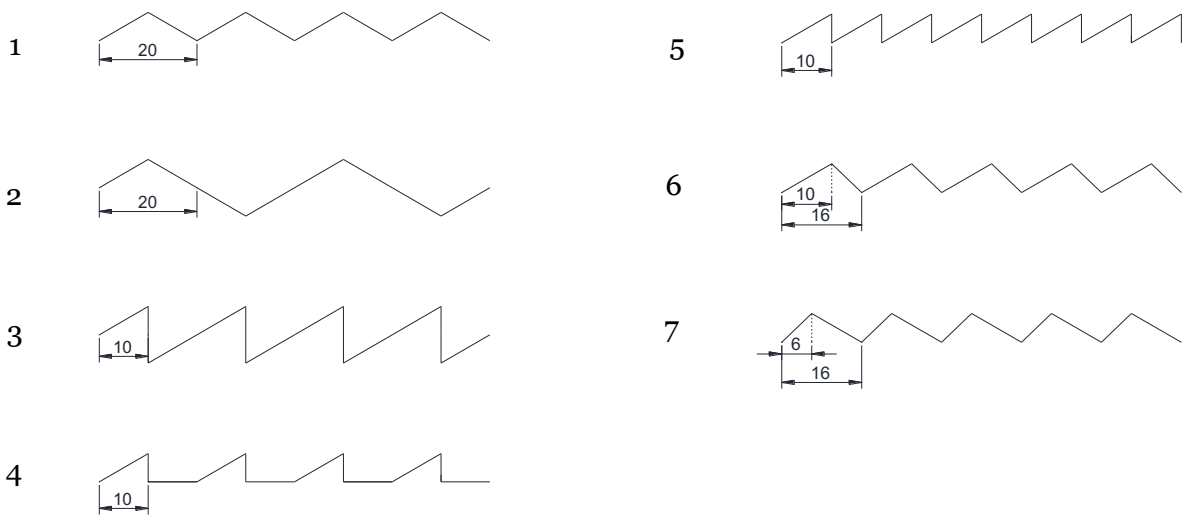

Figure 4.2. Geometry of the triangular profiles for direct shear tests.

The normal stiffness should be representative of field conditions (surrounding rock mass or rock reinforcement (Indraratna et al., 2015)). However, in this study, to understand the effect of boundary stiffness on the behaviour of the 3D printed joints, primarily a normal stiffness based on similar studies in the literature was selected (e.g., Indraratna et al., 1999).

4.3.2 Direct shear test results in CNL conditions

Results of shear stress and dilation vs. shear displacement in CNL tests of profiles 1-7 are plotted in Figure 4.3. From the shear stress versus shear displacement plots in all the CNL tests, it is evident that at the beginning, the shear stress increased in a linear elastic fashion. After the shear stiffness is mobilized, the upper profile surface slides over the lower asperities, causing dilation. As shear displacement progresses, the contact area decreases. This generates localized

normal stresses and escalates frictional resistance. Then the shear stress reaches its peak, and due to the wear of the surface of the profiles and the cracks in the intact material, shear stress drops.

Table 4.1. Statistical parameters for triangular profiles.*

Profile	R_p	R_v	R_t	CLA	RMS	Z_2	Z'_2
1	2.89	2.89	5.77	1.44	1.67	0.5774	0.4082
2	5.77	5.77	11.54	2.89	3.33	0.5774	0.4082
3	5.77	5.77	11.54	2.89	3.33	∞	0.5774
4	4.33	1.44	5.77	1.62	1.86	∞	0.4082
5	2.89	2.89	5.77	1.44	1.67	∞	0.5774
6	2.89	2.89	5.77	1.44	1.67	0.7453	0.4564
7	2.89	2.89	5.77	1.44	1.67	0.7454	0.5893

* Statistical parameters defined in section 2.5.1

As noted earlier, additional tests were carried out on profile 1 which included CNL tests with applied normal stress of 0.5 MPa and 1 MPa. These results are depicted in Figure 4.4. From these charts it is evident that in CNL conditions, as the normal stress increased from 0.25 MPa to 0.5 MPa to 1 MPa, the shear strength increased by 103% and 263%, also the shear stiffness increased by 39% and 64%. In the next sections, these results are evaluated in greater detail.

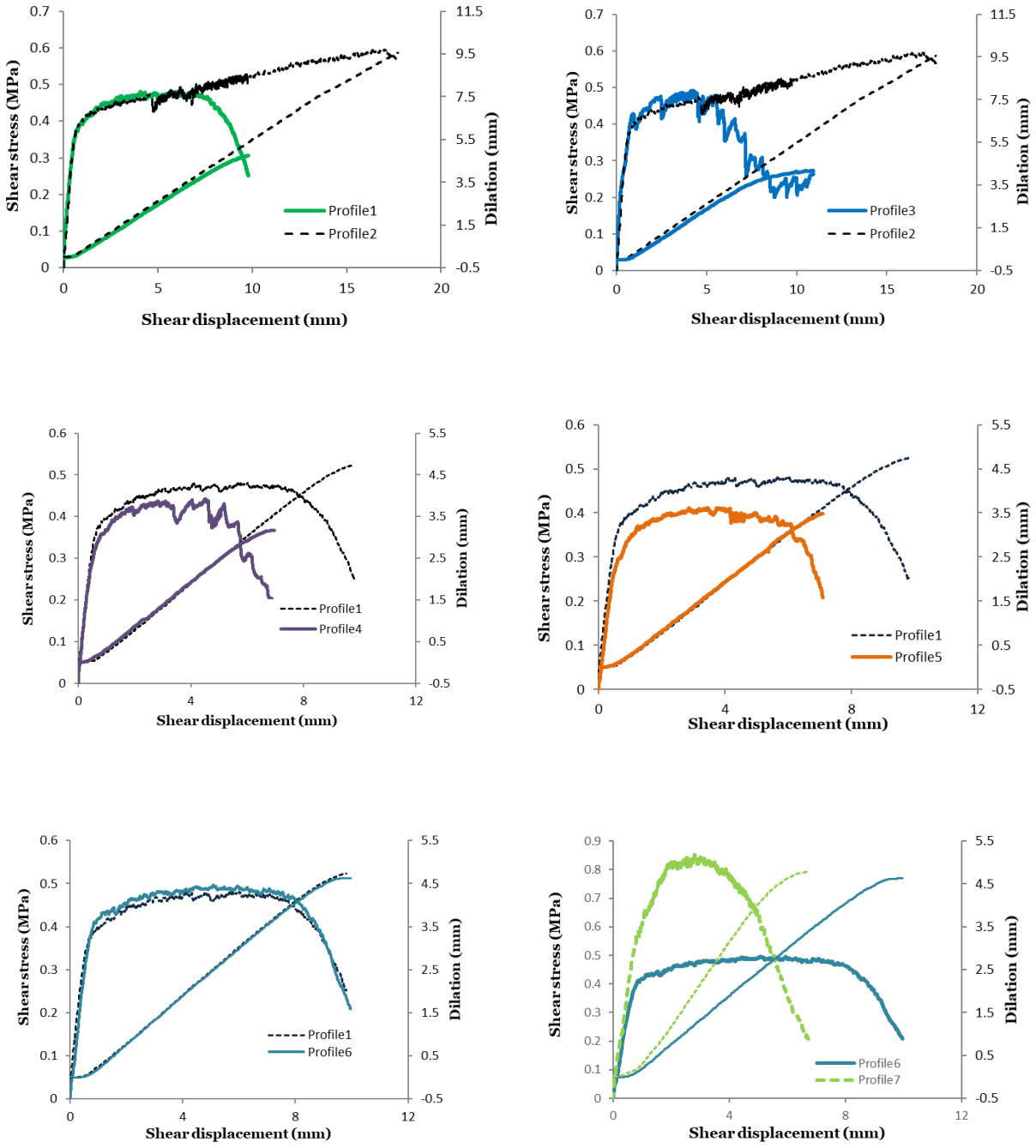

Figure 4.3. Shear stress and dilation vs. shear displacement in CNL conditions, profiles 1-7.

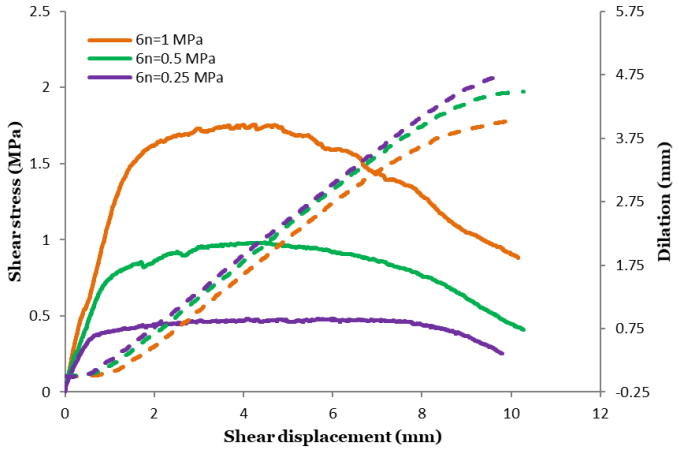

Figure 4.4. Comparison of shear stress and deformation of profile 1 in CNL under 0.25 MPa, 0.5 MPa and 1 MPa applied normal stress. The solid lines illustrate stress and the dashed line illustrate dilation.

4.3.3 Direct shear test results in CNS conditions

To gain insight into the shear behaviour of the discontinuities in constant normal stiffness boundary conditions, direct shear tests in CNS were conducted on profiles 1-6. The initial applied normal stress was 0.25 MPa and the applied normal stiffness was k=5 kN/mm. First, the response of each profile is compared in CNS and CNL boundary conditions and their shear stress and dilation vs. shear displacement is plotted in Figure 4.5. Then the profiles are compared two-by-two in CNS conditions in Figure 4.6 which showcases the change in shear and normal stresses versus shear displacement. The stress paths for profiles 1-6 are illustrated in Figure 4.7. For each profile, the applied normal stress starts at 0.25 MPa, then continues to increase with the application of normal stiffness.

For profile 1, a direct shear test in CNS conditions under k=10 kN/mm normal stiffness was also carried out. The shear stress-shear displacement and dilation-shear displacement of this test is plotted alongside the results of the direct shear test of profile 1 under k=5 KN/mm, in Figure 4.8. The results are discussed further in the next section.

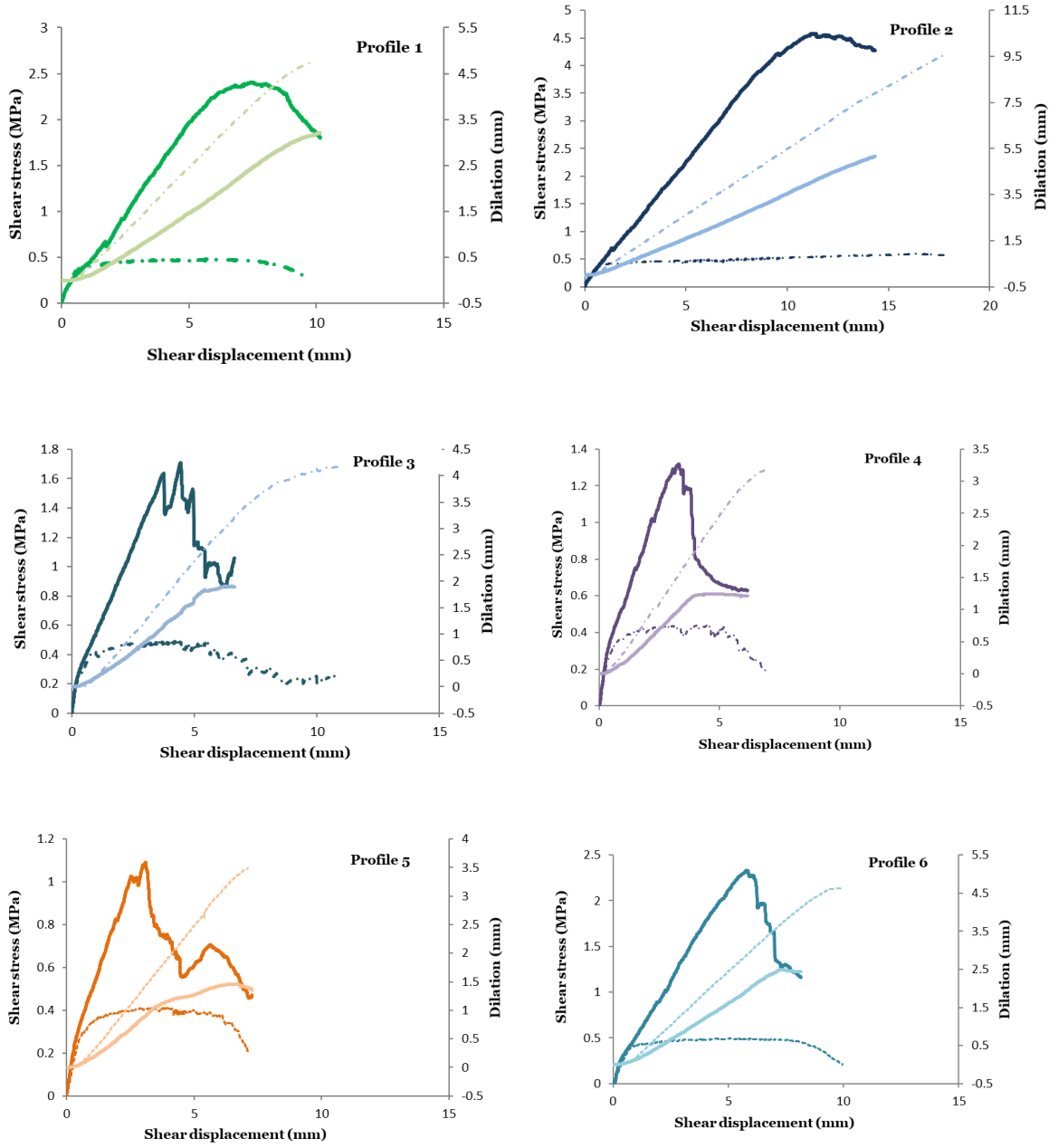

Figure 4.5. Shear stress and dilation vs. shear displacement for profiles 1-6, comparison between CNS and CNL: Solid lines illustrate CNS conditions, dashed lines illustrate CNL conditions; dark colours show shear stress; light colours represent dilation.

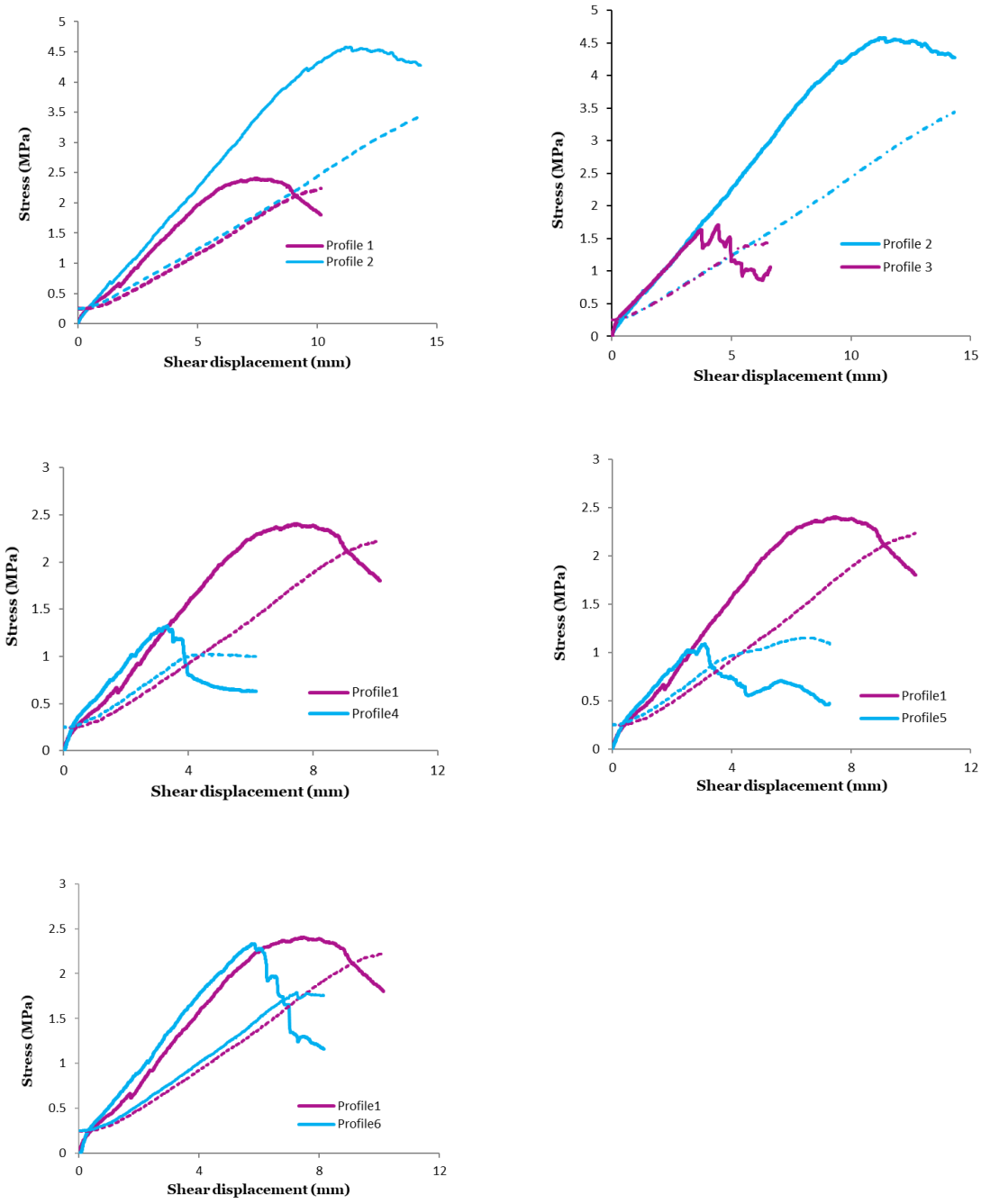

Figure 4.6. Comparison of the normal and shear stress vs. shear displacement of profiles 1-6 in CNS conditions. The solid lines illustrate shear stresses, and the dashed lines illustrate normal stresses.

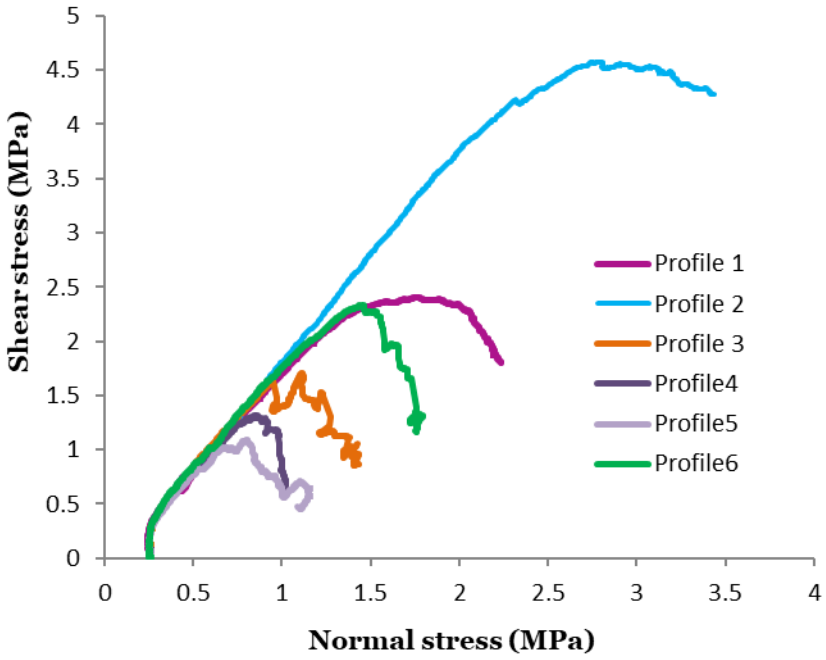

Figure 4.7. Stress paths for CNS conditions for the triangular profiles 1-6. The initial normal stress is 0.25 MPa and applied normal stiffness is k= 5 kN/mm.

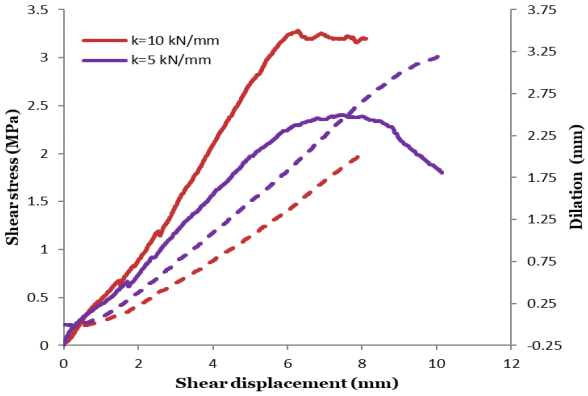

Figure 4.8. Comparison of shear behaviour of profile 1 in CNS under k=5 kN/mm and k=10 kN/mm applied normal stiffness. The solid lines illustrate shear stress and the dashed line illustrate dilation.

4.3.4 Analysis and discussion

In this section, the results of the direct shear tests are discussed for CNL and CNS conditions, with a focus on statistical parameters used to define surface geometry. From Figure 4.3, in CNL conditions, the following observations are made:

A look at the geometry of profile 1 and profile 2 (Figure 4.2) reveals that both geometries have the same slope in the direction of shear, therefore, they have the same Z_2 and Z'_2, however they differ in their respective heights. For profile 1, the total height (R_t) is 5.77 mm, while the R_t for profile 2 is 11.54 mm. In profile 1, when the maximum stress is reached, the contact area was reduced to such an extent that the increase in contact stress led to crushing near the peaks of the teeth. The joint continued to dilate after peak shear stress was reached, albeit with a slightly lower rate. At around 7 mm of shear displacement the magnitude of shear stress decreased rapidly. Profile 2 followed relatively the same path on the shear stress vs. shear displacement curve as profile 1, however where profile 1 reached its peak shear stress and failed, profile 2 continued to gain strength. For profile 2, the geometry of joints reveals that after 20 mm of shear displacement, assuming no degradation of the joint surface occurs, the upper joint surface can slide up the lower joint surface such that the vertex of the upper and lower triangles come into contact. This would lead to maximum dilation. For profile 1, to achieve such maximum dilation, the shear displacement would be equal to 10 mm. For this reason, in profile 2, sliding continued for larger shear displacements. The dilation continued with the same rate throughout the test, only revealing a very slight decrease towards the end, portraying that sliding was the dominant occurrence, while damage was localized. The higher statistical height parameters of profile 2 appropriately predicted the higher peak shear strength at a much higher shear displacement. The strength of profile 2 increased by 23% in comparison to profile 1. Figure 4.9a shows profile 2 at the beginning of the shear test and Figure 4.9b shows sliding of the asperities.

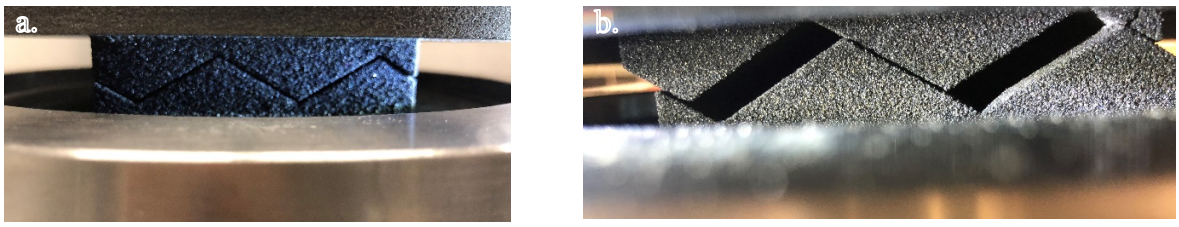

Figure 4.9. Shear tests on profile 2: a. before shear b. sliding of asperities during shear.

In comparison of profile 2 and profile 3, the evaluation of the statistical parameters reveals that the two profiles have identical statistical height parameters (for example R_t=11.54, RMS=3.33), but differ in the statistical slope parameters. Of note is the Z_2 of profile 3 (∞), due to the vertical slopes embedded in the geometry of the profile. With the progression of shear displacement, profile 3 followed the same path as profile 2, until approximately 4 mm of shear displacement, with roughly the same slope in the shear stress- shear displacement curve, where it failed at 0.492 MPa. As mentioned earlier, the height of the profiles is similar, so is the 30° slope of the asperities. However due to the vertical slopes present in profile 3 as demonstrated by the Z_2 parameter, during shearing, there was localized stress concentration on the middle three teeth and cracks were formed on those teeth (Figure 4.10). This is reflected in the shear curve as there are signs of damage and drops in the magnitude of shear stress after the initial phase of overcoming frictional resistance. The accumulation of cracks resulted in the failure occurring at a shear displacement lower than that of profile 2, and with lesser magnitude. Of interest is that the failure pattern observed in Figure 4.10 is asymmetric. This might be due to the non-homogeneous stress distribution and tilting of the sample in the shear setup.

Moving on to profile 4, this profile has four triangular teeth that are separated by four horizontal spaces. The base length of the teeth and the horizontal spaces are 10 mm long and it also has four vertical slopes. The total height of the profile (R_t) is the same as profile 1, however the values of CLA and RMS of profile 4 are higher than that of profile 1. The Z_2 is ∞ and the Z'_2 is the same as profile 1. The overall shape of the shear stress- shear displacement curve for profiles

1 and 4 were generally similar, however, the shear stress curve in profile 1 was smoother in comparison to profile 4. There were signs of asperity damage and breakage at roughly 3.5 mm of horizontal displacement, which was evident in the drops in the shear stress curve. This was similar to the drops in shear stress in profile 3 due to the localized stress concentration on the triangular edges. The post peak softening phase was more rapid in profile 4 compared to profile 1. In comparison, the magnitude of peak shear stress in profile 1 is roughly 9% more than profile 4. The cracking of the asperities is shown in Figure 4.11a.

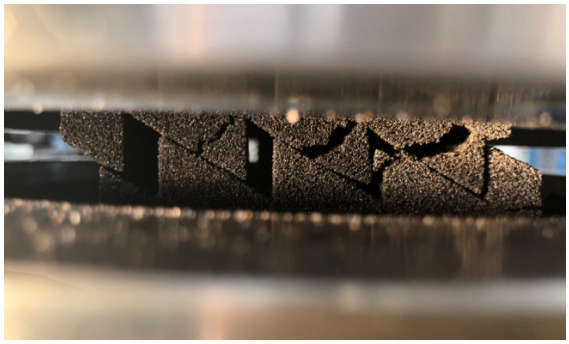

Figure 4.10. Cracking near the tips of triangular teeth in profile 3 during shearing.

Profile 5 with eight right angle triangular teeth and base length of 10 mm features identical height statistical parameters as profile 1 but differs in Z_2 and Z'_2. Again, due to the vertical slopes present in profile 5, Z_2 is ∞. The stress-horizontal displacement curve was similar to profile 1 and profile 4 in terms of shape. However, it didn't have the sharp drops in the magnitude of shear stress as was observed in profile 4. This is because the normal load is distributed on a larger area in profile 5 as opposed to profile 4 (Figure 4.11b).

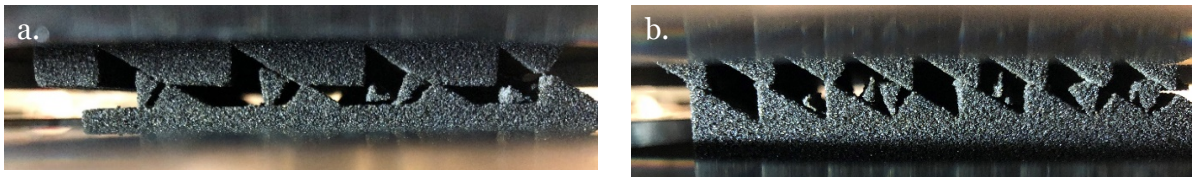

Figure 4.11. Asperity damage: a. profile 4 b. profile 5.

Progressing to profile 6, there are six triangular teeth, where the slope in the direction of shear is 30° but opposite to the direction of shear is about 44°. The statistical height parameters are the same as profile 1. The Z_2 is 0.7453 which is higher than profile 1, however the Z'_2 parameter is closer to profile 1 at 0.4564. The shear stress vs. horizontal displacement of profile 6 closely resembles profile 1. From the vertical displacement plots it is evident that for profiles 1-6, all the curves follow the same pattern and the same dilation rate. The joints continue to dilate after peak shear stress was reached, but with a slower rate. The shear stiffness (k_s) for these profiles was approximately between 0.6-0.7 MPa/mm.

To further explore the importance of directionality, profile 6 was reversed (and named profile 7) and sheared in the direction of the 44° slope asperities. Profiles 6 and 7 have all the same statistical parameters and differ only in Z'_2 (=0.5893 for profile 7). The shear strength of profile 7 was, as predicted, higher than profile 6 (71% higher) which occurred at 2.8 mm of shear displacement, at a lower shear strain than profile 6. The dilation rate was higher because sliding took place on an asperity with higher slope (Figure 4.12).

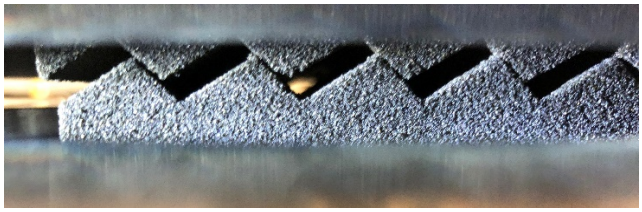

Figure 4.12. Sliding of asperities in profile 7.

As mentioned, additional tests were carried out on profile 1. Referring to Figure 4.4, where the shear response of profile 1 is shown under various normal stresses, it is seen that at higher applied normal stresses, the joint displayed a more brittle post peak response. This was also reported in Indraratna et al. (1998) for sawtooth joints made from gypsum plaster. Also, as expected, the magnitude of dilation decreased with the increase of normal stress from 0.25 MPa to 0.55 MPa to 1 MPa. Peak shear strength of profile 1 in CNL conditions, along with Patton's

shear strength model (Patton, 1966) for sliding are drawn in Figure 4.13. The experimental results follow Patton's shear strength model for sliding (Equation (2.1)) quite well where $\emptyset_b = 29.7°$ and $i = 30^0$. This shows that in these tests the main shearing mechanism was sliding.

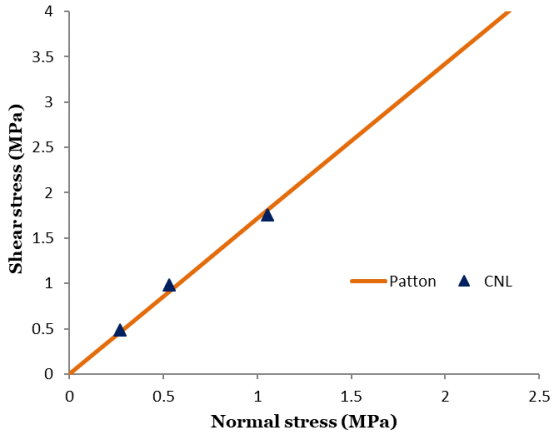

Figure 4.13. Comparison of peak shear strength of profile 1 in direct shear tests under CNL conditions with Patton's sliding model.

Moving forward to direct shear tests in CNS conditions, from Figure 4.5 and Figure 4.6, the following observations are made:

In all the profiles, similar to the constant normal load condition, elastic deformations took place before the sliding of the two faces of the asperities. When static friction was overcome by localized shear stresses (Tatone, 2014), sliding began and the upper asperities rode the lower ones. This was observed with the change in the slope of the shear stress- shear displacement curve. With the continuation of sliding and dilation, the normal load increased due to the applied stiffness on the samples, which lead to more shear resistance until there was enough damage to the asperities by formation of shear planes and/or surface wear such that asperities failed, and the shear resistance dropped. Similar observations were noted by Kodikara and Johnston (1994) for triangular asperities. In their tests, the triangular asperities were made with two different material: for the bottom joint surface, a synthetic soft rock was constructed from combining mudstone powder, cement, water and a set accelerator. The UCS of this material was equal to 2.8

MPa and the secant modulus was equal to 360 MPa. The top joint surface was built from concrete. The failure of the asperities was controlled by the soft rock that was much weaker than the concrete. In their results however, in most samples, after full mobilization of friction, a drop in the shear resistance was reported. This was due to the remolding of micro-asperities in the soft rock joint surface. Comparing the shear response of profile 1 to the shear strength of regular triangular joints made with cement mortar with 25 and 45 degree angles from Mouchaorab and Benmokrane (1994), showed that the shear strength of cement mortars were significantly higher and their post peak response was more abrupt. The reason was the properties of the high strength mortar (UCS = 100 MPa, E = 35 GPa), also the loss of cohesion in the asperities after failure. This showed that the mode of failure was different in these samples compared to the printed samples. In profile 1, the post peak decline in shear strength was more gradual. This was reflected in examining the damage following the shear test where the particles of sand that were sheared off were close to the surface of the asperities and no visible cracks were formed penetrating in the intact rock.

Furthermore, in CNS conditions all profiles exhibited brittle behaviour and post peak softening happened at a higher rate compared to CNL conditions. However, rate of softening in profiles 1 and 2 was not as high as in profiles 3-6. This is because at the time of failure, the area of the asperities in contact for profile 1 and 2 was greater compared to profiles 3-6, allowing for more uniform stress distribution and gradual failure.

Based on visual observations, the number of cracks formed were more significant in CNS conditions compared to CNL conditions. A clear peak shear stress is noted in all the tests in CNS condition. This was also observed in Indraratna et al. (1999) for saw-toothed specimens made from gypsum plaster (UCS = 11-13 MPa, E =1.9-2.3 GPa). The specimens had teeth with inclination angles equal to 9.5^{o} and 18.5^{o} and were tested in CNS with σ_{n0} = 0.30 MPa, 0.56 MPa and 1.10 MPa and under normal stiffness equal to 8.5 kN/mm. However, in Jiang et al. (2006)

for standard joint surfaces with JRC=8-10, σ_{n0} = 2 MPa and under k=3 GPa/m and 7 GPa/m, also a replica of a natural joint surface with equivalent JRC=0-2, σ_{n0} = 1 MPa and under k= 7 GPa/m, the shear stress continued to increase until the end of the direct shear tests with 20 mm of shear displacement. These artificial samples were made with a mixture of plaster, water and retardant (UCS= 47.4 MPa, E = 28.7 GPa, σ_t = 2.5 MPa). In another study by Jiang et al. (2004b) the same observations were made for standard joints with JRC = 4-6, σ_{n0} = 5 MPa and under k=3 GPa/m and 7 GPa/m using the same material. They also replicated rough joint surfaces in granite using resin concrete (UCS= 107.7 MPa, E = 27.1 GPa, σ_t = 10.3 MPa) and for these joints with JRC = 3.6, σ_{n0} = 2, 5 MPa and under k=5.4 GPa/m, also joint surfaces with JRC = 8.5, σ_{n0} = 2 MPa and under k=5.4 GPa/m the same trend of shear stress increase with shear displacement was observed. Lindenbach and Bearce (2018) performed tests on sawtooth joints made of hydrostone. In their investigations, tests were carried out in CNL under initial applied normal stress ranging from 30 to 280 kPa and in CNS with initial normal stress of 30 kPa and two normal stiffnesses (i.e., 0.88 kN/mm and 1.75 kN/mm). The sawtooth joints had 12^o angle asperities, with one set of specimens having large ridges and the other having small ridges. For CNS tests, for small ridge samples, a peak shear stress was reached, however in the large ridge specimens, the shear stress continued to increase until the end of the tests. Indraratna et al. (2015) stated the reason a distinct shear stress might not be demonstrated in shear plots might be that the extent of asperity damage is such that the resulting gouge compaction nullifies the roughness of the other asperities. Or, that rolling friction becomes prominent compared to sliding friction because of the gouge formation. Therefore, in the above cases where there was a distinct peak shear stress such as the results of the shear tests in this study, the formation of gouge was not adequate to cause these effects.

Comparing the shear strength of the profiles in CNL and CNS conditions (Figure 4.5) revealed that in CNS the shear strength increased significantly due to the constrained dilation and increased normal load applied to the asperities. The difference between the peak shear strength

in CNL and CNS conditions was maximum for profile 2 (670% increase) and minimum for profile 5 (165% increase). This was because in profile 2 sliding was the main shearing mechanism and in contrast, in profile 5, shearing off of the asperities was the main mechanism, which led to failure at a lower shear displacement. Profile 2 had the largest shear strength and maximum shear displacement, and these values were the lowest for profile 5 in both CNL and CNS conditions.

Considering the dilation rate of the profiles, it is revealed that in CNL conditions, the dilation closely followed the slope of the asperities. As an example, a line corresponding to the angle of the asperities, i.e., 30 degrees is drawn on the dilation versus shear displacement curve for profile 1 in Figure 4.14. In CNS conditions, the dilation angle is less than in CNL, and therefore less than the asperity inclination angle. This is due to the normal and shear loads applied on the asperities.

Comparing profiles 1 and 2 in CNS conditions (Figure 4.6), the shape of the profiles in the shear stress-shear displacement curve are generally the same: both have smooth curves with no sudden drops in the shear stress and a gradual post peak softening. Because of the higher height statistical parameters (R_t, CLA) of profile 2, the top joint surface continued to slide up the bottom asperities, and with the gradual increase of normal stress on the joint surface, the profile failed at 4.579 MPa. The normal stress curves of the profiles closely followed each other. Profile 3 followed the same shear stress vs. horizontal displacement as profile 2, until roughly 3.7 mm of shear displacement, where cracks were formed abruptly, and asperities failed quickly. Profiles 3, 4 and 5 all showed similar patterns of abrupt post peak failure. Compared to tests run in CNL conditions, profiles 3, 4 and 5 had the least amount of increase in maximum shear stress (248%, 198% and 165% respectively). This is due to the localized stress concentrations on the right-angle teeth (Figure 4.15). Profile 6 fails at 2.332 MPa and post peak softening in profile 6 is more rapid compared to profile 1. As mentioned before, in CNL conditions, both profile 1 and profile 6 had

very similar shear stress and dilation curves. The increase in normal stress and the stress concentration on the asperity tips led to this post peak difference in CNS conditions.

Of note is that although the Z_2 parameter in profiles 3, 4 and 5 (i.e., ∞) was able to detect the vertical slopes present in the geometries, however the failure of asperities is due to local stress

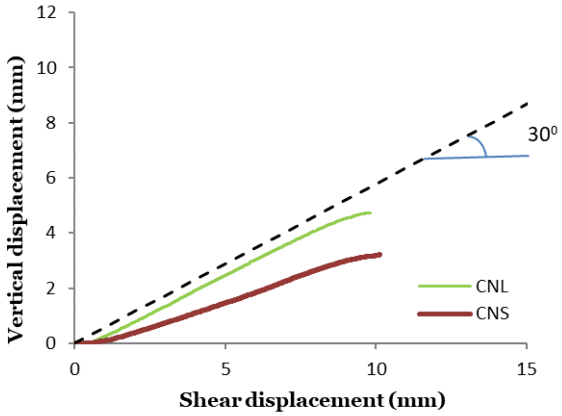

Figure 4.14. Comparison of dilation angle of profile 1 with the asperity angle in CNL and CNS.

concentrations. For example, a rectangular shaped asperity with vertical edges will also have a Z_2 of ∞, however it will show greater shear resistance compared to a triangular asperity like profile 5, because in profile 5, there is high non-uniform stress distribution on the triangular asperity edge, which leads to asperity failure.

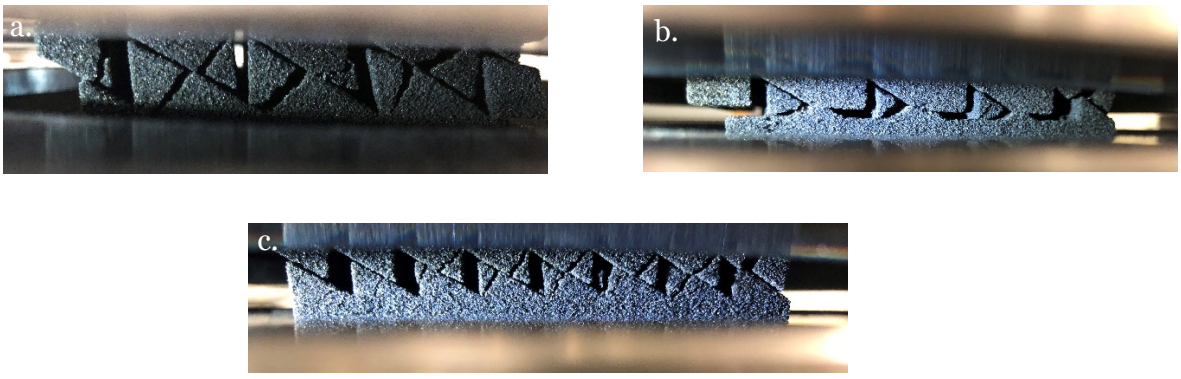

Figure 4.15. Stress concentration on the asperity tips: a. profiles 3 b. profile 4 c. profile 5.

The stress paths for profiles 1-6 in CNS conditions (k=5 kN/mm) are drawn in Figure 4.7. From that graph it is seen that all the profiles followed the same linear path until approaching near the peak shear stress (albeit before reaching the peak), where the paths became non-linear and the rate of change in normal stress decreased based on the geometry of the joint. Nevertheless, in all the profiles, the normal stress continued to increase even after the joints had reached peak shear strength. This is likely because at failure, the damage was localized, and the joints continued to dilate. Profile 2 had the highest increase in normal stress, (σ_n= 2.75 MPa at maximum peak shear strength) and profile 5 had the lowest increase (σ_n= 0.80 MPa at maximum peak shear strength). Towards the end of the tests, for some of the joints (for example profile 1 and 2) the normal stress continued to increase. For others such as profile 4, the normal stress was constant after approximately 4 mm of shear displacement. For profile 5 the normal stress decreased towards the end of the test. This is due to the substantial damage of the asperities in these profiles.

As noted earlier in this chapter, additional tests were carried out on profile 1. From Figure 4.8, it is observed that in CNS conditions, for the test under k=10 kN/mm the shear strength increased by 37% and the peak shear horizontal displacement decreased by 16% compared to the test carried out under 5 kN/mm normal stiffness. The increase in shear strength was expected due to the higher normal stiffness that caused the increase of normal load on the asperities. Rim et al. (2005) reported similar results in CNS tests on cement-mortar sawtooth samples (UCS = 47 MPa and E = 14.0 GPa, σ_t = 4 MPa) with inclination angles between 5° and 30°, where they observed an increase in the maximum shear stress when the normal stiffness increased from 0.2 MPa/mm to 0.5 MPa/mm to 1 MPa/mm.

Looking at the dilation charts of profile 1, the shapes of the dilation curves look relatively similar in CNL and CNS conditions (Figure 4.4 and Figure 4.8). In CNS, the magnitude of dilation was hindered for both stiffnesses, and was less than CNL conditions. The reason is that in CNS, the increase in normal load was approximately 2.5-3 times more compared to the CNL test under

the largest applied normal stress (i.e., σ_n= 1 MPa). The damage to the asperities increased in CNS conditions, which is evident from the dilation curves where the dilation magnitude and dilation rate decreased with the advent of the tests and the increase in shear displacement.

The stress paths for profile 1 under k=5 kN/mm and k=10 kN/mm in CNS conditions are depicted in Figure 4.16 and for comparison, the peak shear strengths in CNL and Patton's shear strength model (from Figure 4.13) are also drawn. From this plot it is seen that the pre-peak CNS stress paths follow the CNL failure envelope up to approximately the 1.2 MPa normal stress mark for k=5 kN/mm and up to approximately 1.9 MPa normal stress for k=10 kN/mm, affirming that up to these stresses, the dominant shear mechanism was sliding. Lindenbach and Bearce (2018) reported that for sawtooth joints made of hydrostone (mentioned in the previous paragraphs), the CNL failure envelope was close to the rollover of the CNS stress paths. Distinctly, for the samples with small ridges under both normal stiffnesses and for specimens with large ridges under the lower stiffness, the CNS strength envelope was lower than the CNL failure envelope. For specimens with large ridges and k=1.75 kN/mm, the CNS stress path followed the CNL failure envelope.

In CNS conditions, after the peak shear stress was reached for profile 1, the normal stress continued to increase, however the rate was lowered, showcasing localized damage. This was also the case in Lindenbach and Bearce (2018) for small ridge samples where the normal stress decreased after peak shear strength but for large ridge joints the normal stress continued to increase until the end of the test, most likely showing greater damage on smaller ridges.

To obtain a better understanding of the influence of geometrical parameters involved in shear, the stress-dilation response of the profiles is explored further: As mentioned, in CNL conditions profile 7 showed the highest shear strength among all other profiles. This is logical as the slope of the asperity in the direction of shear had the largest angle (44 degrees). This is showcased in its Z_2 (0.5893) and even though the amplitude parameters of profile 7 are half of

profile 2, it's shear strength is 43% higher than profile 2 and 75% higher than the average of all the other profiles. Among the profiles that had the same slope in the direction of shear, profile 2 had the highest shear strength, 28% higher than the average of other profiles. The lowest shear strength was recorded for profiles 4 and 5. The reason was the concentration of stress on the tooth near the vertical edges present in the geometry.

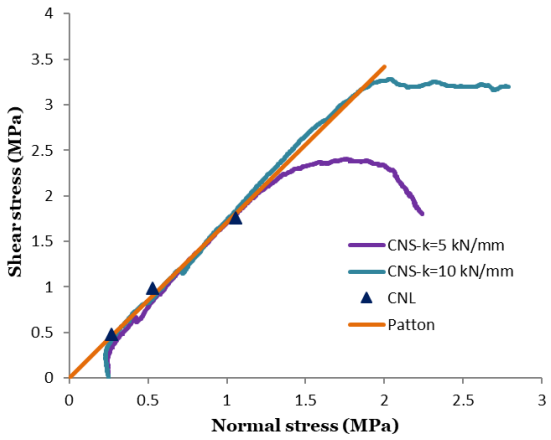

Figure 4.16. Stress paths for profile 1 in CNS – for comparison peak shear strength in CNL and Patton's sliding model are also drawn.

In CNS, the maximum shear strength was reported for profile 2 (a CNS test was not conducted on profile 7) at 4.579 MPa. The lowest exhibited strength was for profiles 4 and 5, which was similar to the CNL results. However, the differences in statistical parameters led to higher distinctions in the overall shear stress-shear displacement curves for all the profiles in CNS conditions as opposed to CNL conditions; and as mentioned by Yang et al. (2010) and Hencher and Richards (2015), other than peak shear stress, the *complete* shear stress-shear displacement curve is important in evaluating the behaviour of rock joints.

The peak shear stress versus applied normal stress for all the profiles in CNL and CNS conditions is plotted in Figure 4.17. As shown in this figure the difference in peak shear response under CNS conditions is higher compared to CNL conditions. As an example, the shear strength of profile 2 showed 320% increase compared to profile 5 in CNS conditions. This value was 44 %

in CNL conditions. It is important to note that the difference in the maximum shear stress in CNS is due to the difference in normal stress at failure for each profile. If the shear stress would be normalized to normal stress (giving the instantaneous friction angle), this difference would be minor. Nevertheless, the magnitude of peak shear stress in CNS compared to CNL is of importance.

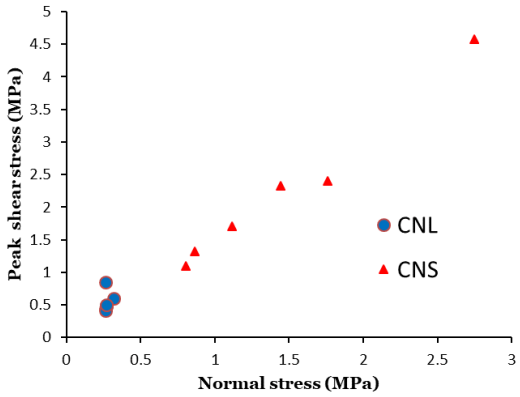

Figure 4.17. Peak shear stress vs. normal stress for triangular profiles in CNL and CNS conditions.

The peak shear stress of the profiles is plotted against CLA in CNL and CNS conditions in Figure 4.18. Also, the peak shear stress versus Z'_2 in CNL and CNS conditions is plotted in Figure 4.19. From these plots it is concluded that based solely on one statistical parameter -used to define the geometry-there isn't a clear correlation between that parameter and peak shear strength. If both amplitude and slope parameters are considered, better prediction on the behaviour of the joints can be made, however even that is not enough. Therefore, it is concluded that even though statistical parameters are good indicators for defining the anisotropy in roughness of the profiles, they are not adequate. Other factors such as contact area and edge effects that results in local stress concentrations play an important role in predicting the shear response of joint surfaces.

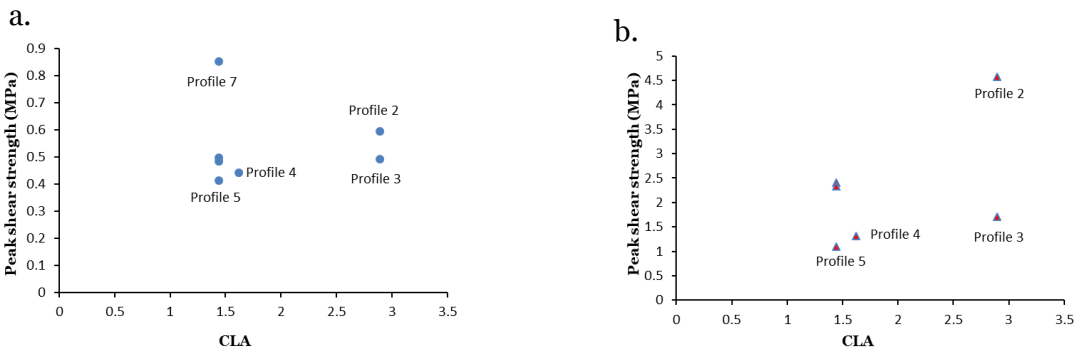

Figure 4.18. Peak shear stress vs. CLA for triangular profiles: a. CNL conditions b. CNS conditions.

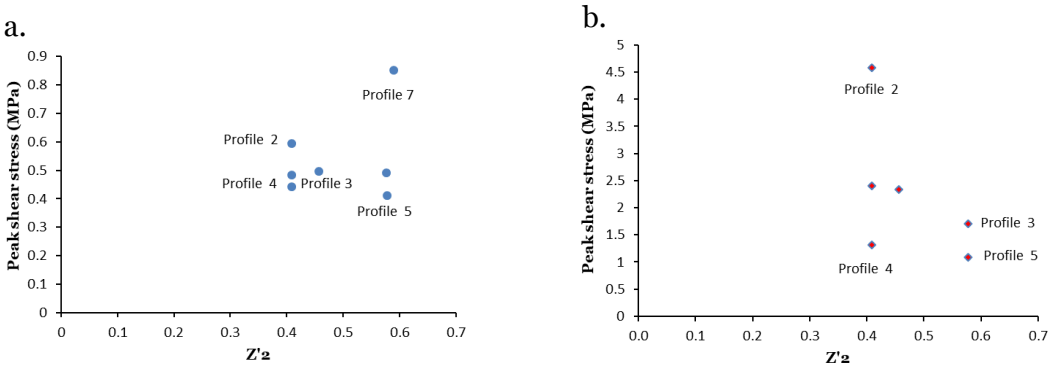

Figure 4.19. Peak shear stress vs. Z'$_2$ for triangular profiles: a. CNL conditions b. CNS conditions.

4.4 Rearranged standard profiles

4.4.1 Geometry and test configurations

In this section the effectiveness of standard JRC profiles in defining the surface geometry and therefore estimating the shear strength and deformation of 3D printed rock joints is explored. For this purpose, new geometries were constructed by rearranging two standard JRC profiles and direct shear tests in CNL and CNS boundary conditions were conducted on them. The first joint profile was in the smoother range, i.e., JRC 6-8 and the other profile was the roughest in the JRC standard chart, i.e., JRC 18-20. Using a MATLAB code, each profile was divided into smaller segments and the segments were randomly rearranged to change the geometry configuration and create new joint profiles. The profiles were only rearranged in 2D, along the shearing direction.

For the profile with JRC=6-8, the original joint was divided into 5 segments and a new set of geometries were constructed. For the profile with JRC 18-20, two sets of geometry were configured. In the first set, the original length of the profile was divided into 5 segments and in the second set the original length was divided into 10 segments. Then for each profile the segments were rearranged, constructing new geometries. Statistical parameters Z_2 and Z'_2 were calculated for the new configurations, a number of profiles with the maximum and minimum Z_2 and Z'_2 were selected as the new geometries to be sheared. In total 9 new profiles called the New Configured Joints (NCJs) were created. The new joint samples were named in the following manner: for the joints based on JRC 6-8: *NCJ-4-sample#*, and for the joints based on JRC 18-20: *NCJ-10-sample#*. The specimens were rectangular and the set width of all the profiles were 100 mm. The rearranged joints have geometries that are different from the original standard JRC profiles. This is reflected in their corresponding statistical parameters. The statistical parameters are calculated for the original profiles and the NCJs and presented in Table 4.2.

Figure 4.20 illustrates the joint with JRC=6-8 divided into 5 segments and the resulting NCJ-4-1, NCJ-4-2 and NCJ-4-3. Figure 4.21 illustrates the JRC=18-20 profile divided into 5 segment divisions and the resulting NCJ-10-1, NCJ-10-2 and NCJ-10-3. Finally, Figure 4.22 shows NCJs for JRC 18-20 with 10 segment divisions: NCJ-10-4, NCJ-10-5, NCJ-10-6. To better understand the rearrangements, the original joints and the first NCJ in each figure is colour coded.

For CNL conditions, the direct shear tests were done under the applied normal stress of 0.25 MPa. For the CNS condition, the normal stress initiated at 0.25 MPa and fluctuated according to the normal stiffness of k=5 kN/mm. The overall shear behaviour of the newly generated joints which includes peak shear strength and dilation are evaluated. Additional images of the failed profiles are provided as Appendix of this thesis.

Table 4.2. Statistical parameters for the original standard JRC 6-8 and JRC 18-20 and new configured joint (NCJ) profiles

Profile	R_p	R_v	R_t	λ	CLA	RMS	Z_2	Z'_2
Original JRC 6-8	0.84	0.77	1.61	0.02	0.31	0.38	0.1994	0.1460
NCJ-4-1	0.81	0.75	1.56	0.02	0.28	0.34	0.1990	0.1401
NCJ-4-2	1.32	1.11	2.43	0.03	0.44	0.56	0.1997	0.1488
NCJ-4-3	0.96	0.79	1.75	0.02	0.43	0.49	0.1999	0.1305
Original JRC 18-20	2.3	1.71	4.01	0.04	0.69	0.87	0.3938	0.2820
Divided into 5 segments								
NCJ-10-1	1.4	2.7	4.06	0.04	0.75	0.89	0.3967	0.3137
NCJ-10-2	2.48	2.15	4.63	0.05	0.81	1.01	0.3943	0.2764
NCJ-10-3	1.85	1.58	3.42	0.03	0.61	0.77	0.3936	0.2881
Divided into 10 segments								
NCJ-10-4	3.96	3.86	7.82	0.08	1.50	1.75	0.4071	0.3445
NCJ-10-5	2.33	2.17	4.50	0.05	1.09	1.24	0.3936	0.2879
NCJ-10-6	3.81	3.82	7.62	0.08	1.62	1.81	0.4018	0.2495

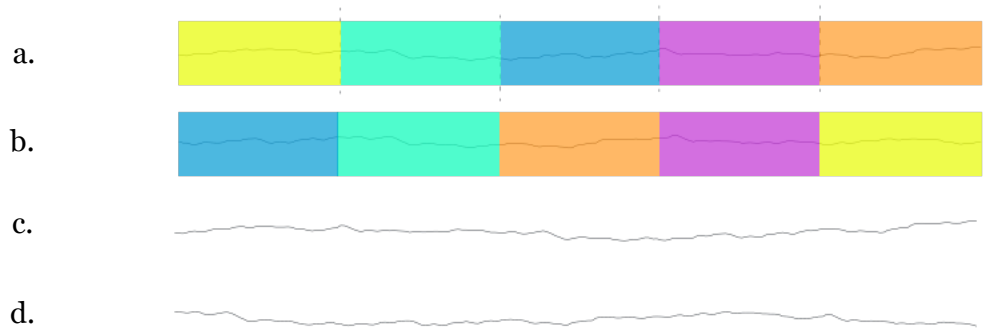

Figure 4.20. New configured joints for JRC= 6-8: a. original joint with JRC=6-8 divided into 5 segments b. NCJ-4-1 c. NCJ-4-2 d. NCJ-4-3.

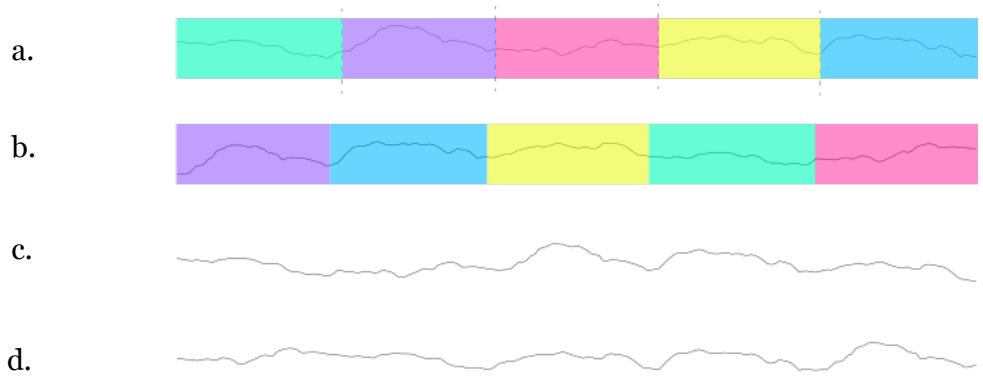

Figure 4.21. New configured joints for JRC= 18-20 a. original joint with JRC=18-20 divided into 5 segments b. NCJ-10-1 c. NCJ-10-2 d. NCJ-10-3.

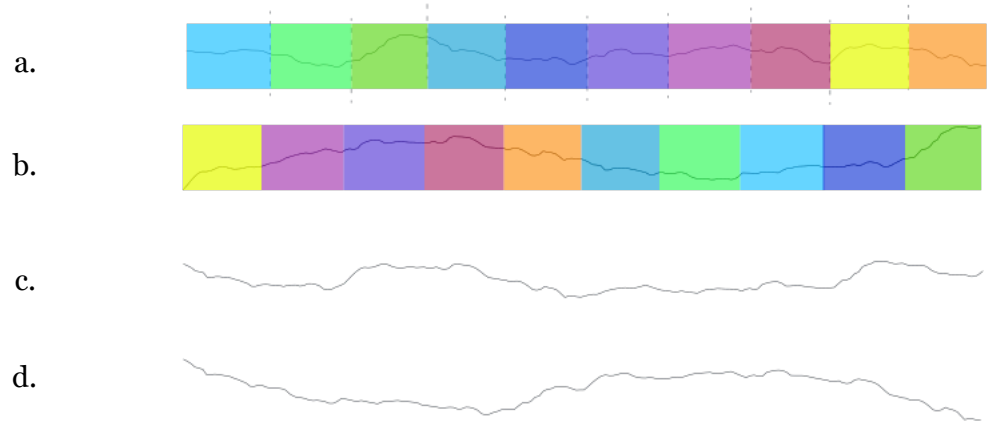

Figure 4.22. New configured joints for JRC= 18-20 a. original joint with JRC=18-20 divided into 10 segments: b. NCJ-10-4 c. NCJ-10-5 d. NCJ-10-6.

4.4.2 Direct shear test results in CNL and CNS conditions

The change of shear stress and dilation with shear displacement for JRC 6-8 profiles and their rearranged counterparts (NCJ-4s) in CNL and CNS conditions are shown in Figure 4.23 and Figure 4.24, respectively. To obtain a better understanding of the differences between CNS and CNL conditions, the shear strength curves of the original and reconfigured surfaces of NCJ-4s are compared two-by-two in CNL and CNS conditions in Figure 4.25.

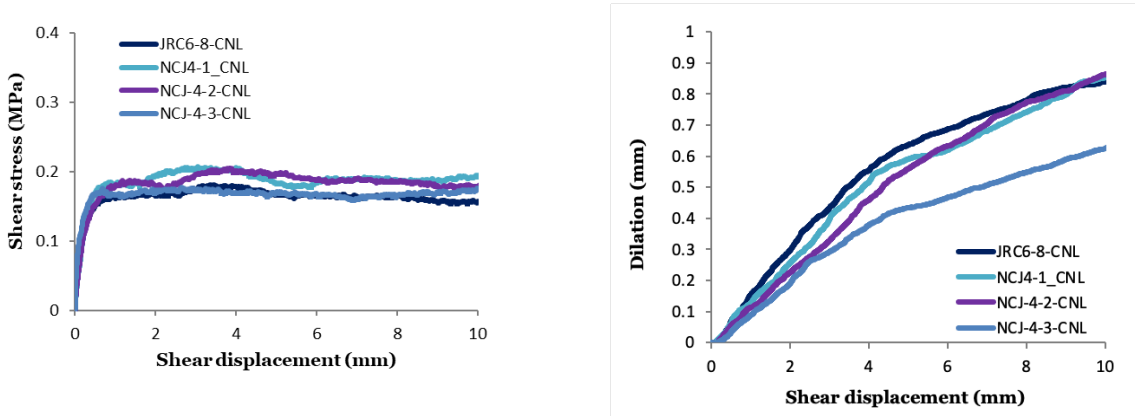

Figure 4.23. Shear stress and dilation versus shear displacement for profiles with JRC 6-8, and NCJ-4-1 to NCJ-4-3 in CNL conditions.

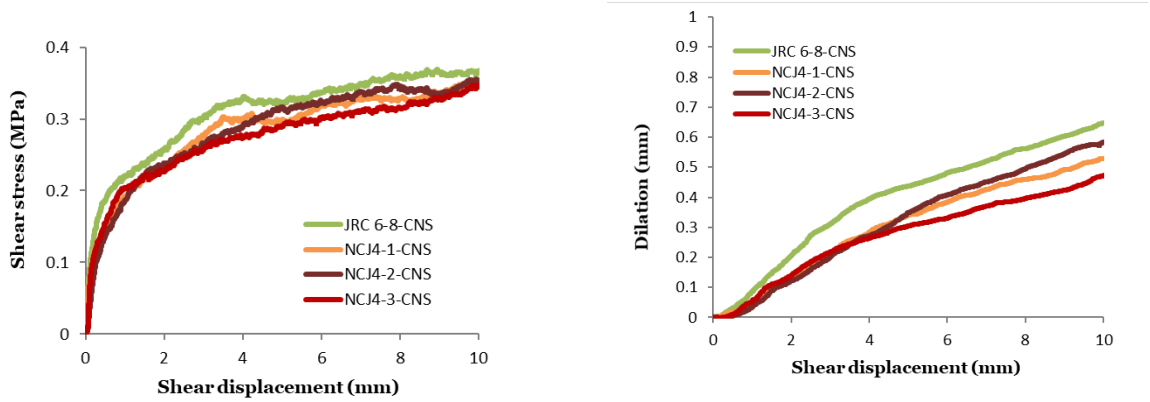

Figure 4.24. Shear stress and dilation versus shear displacement for profiles with JRC 6-8, and NCJ-4-1 to NCJ-4-3 in CNS conditions.

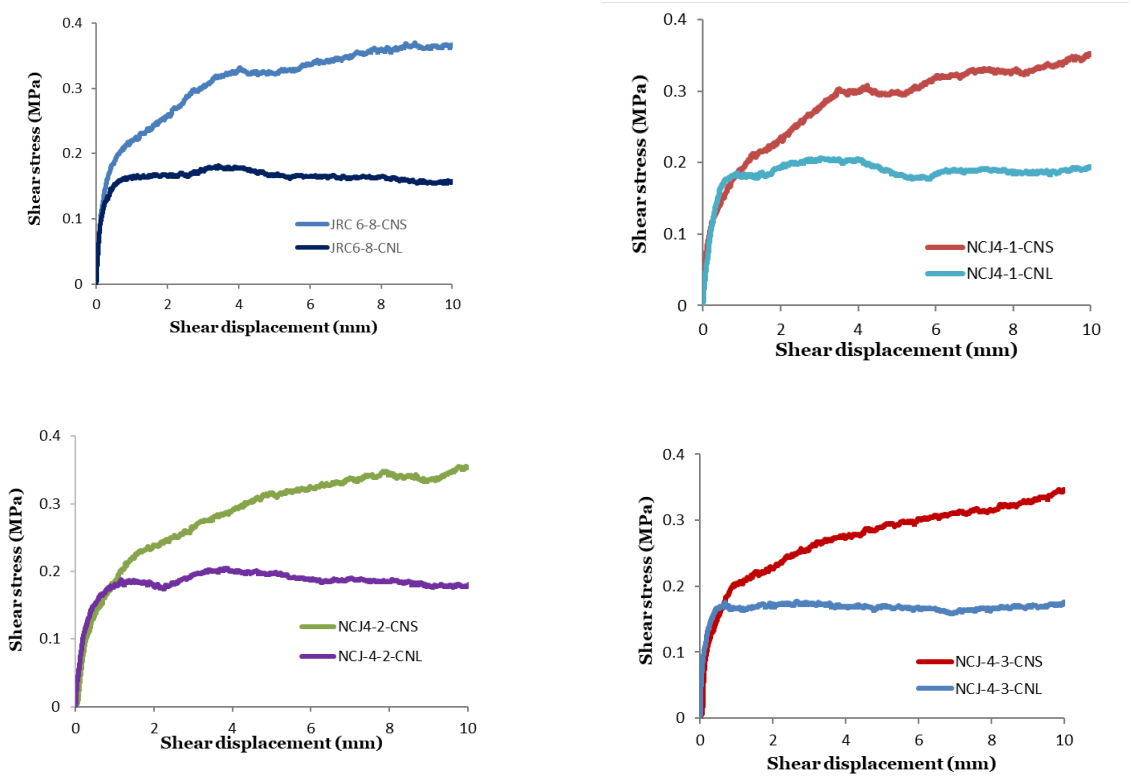

Figure 4.25. Shear stress versus shear displacement for JRC 6-8 and NCJ-4 profiles, comparison between CNL and CNS conditions.

The shear stress and dilation vs. shear displacement for the original JRC 18-20 and the new configurations for the joints that were divided into 5 segments, i.e., NCJ-10-1 to NCJ-10-3 in CNL and CNS conditions are shown in Figure 4.26 and Figure 4.27 respectively. The same plots are drawn for the NCJs that were rearranged based on 10 segment divisions (NCJ-10-4 to NCJ-10-6) in CNL (Figure 4.28) and CNS (Figure 4.29) conditions.

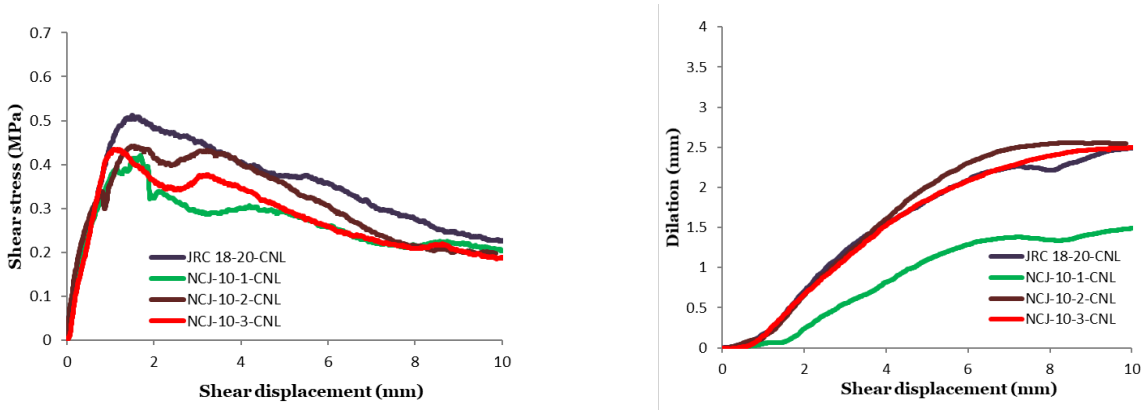

Figure 4.26. Shear stress and dilation vs. shear displacement for original joint with JRC 18-20 and NCJ-10-1 to NCJ-10-3 in CNL conditions.

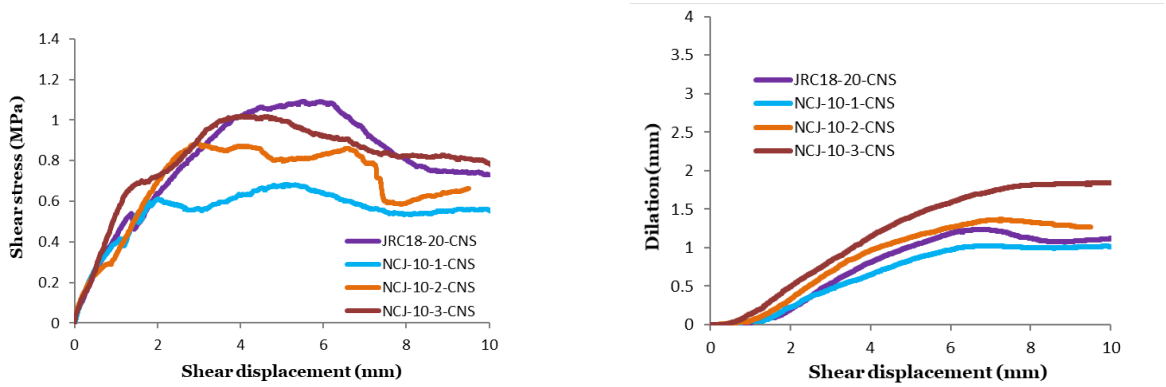

Figure 4.27. Shear stress and dilation vs. shear displacement for original joint with JRC 18-20 and NCJ-10-1 to NCJ-10-3 in CNS conditions.

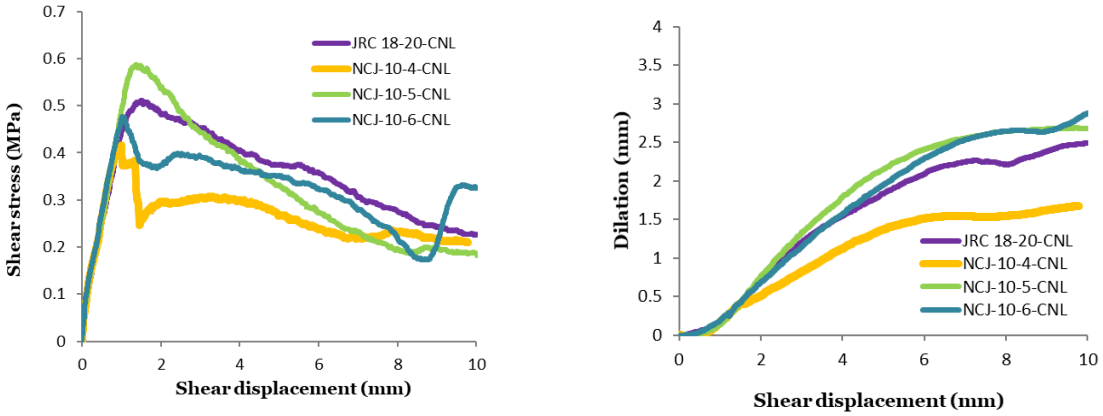

Figure 4.28. Shear stress and dilation vs. shear displacement for original joint with JRC 18-20 and NCJ-10-4 to NCJ-10-6 in CNL conditions.

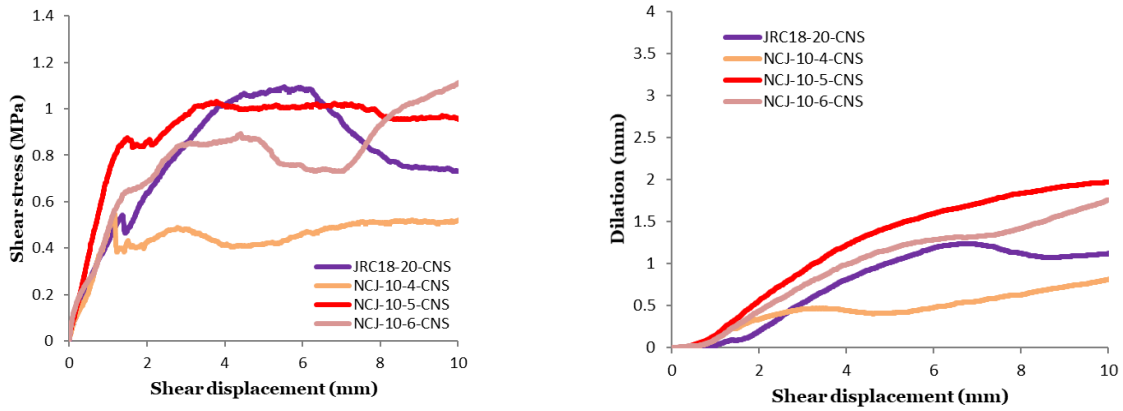

Figure 4.29. Shear stress and dilation vs. shear displacement for original joint with JRC 18-20 and NCJ-10-4 to NCJ-10-6 in CNS conditions.

The shear results for the original joint with JRC=18-20 and for NCJ-10-1 to NCJ-10-6 are compared two-by-two to in Figure 4.30 and Figure 4.31 to further highlight the contrast between CNL and CNS boundary conditions.

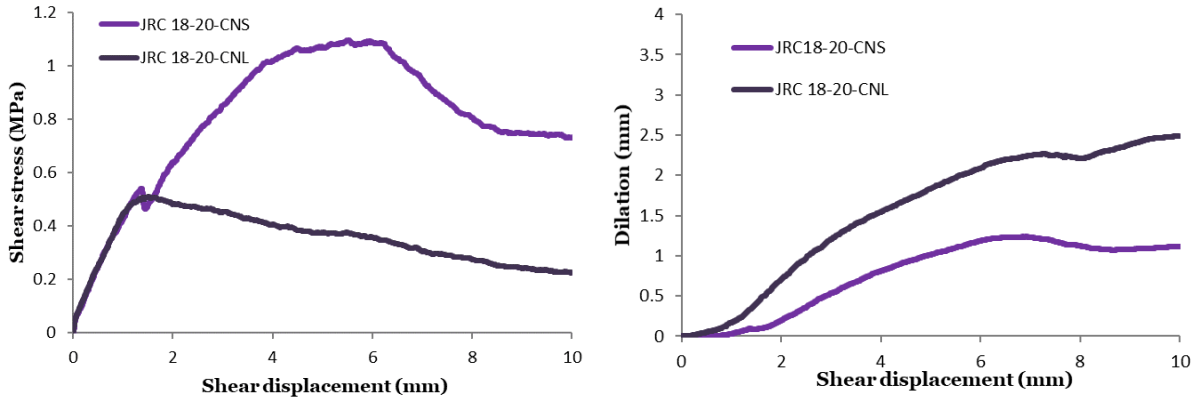

Figure 4.30. Shear stress and dilation vs. shear displacement for the original JRC 18-20 profile, comparisons between CNL and CNS conditions.

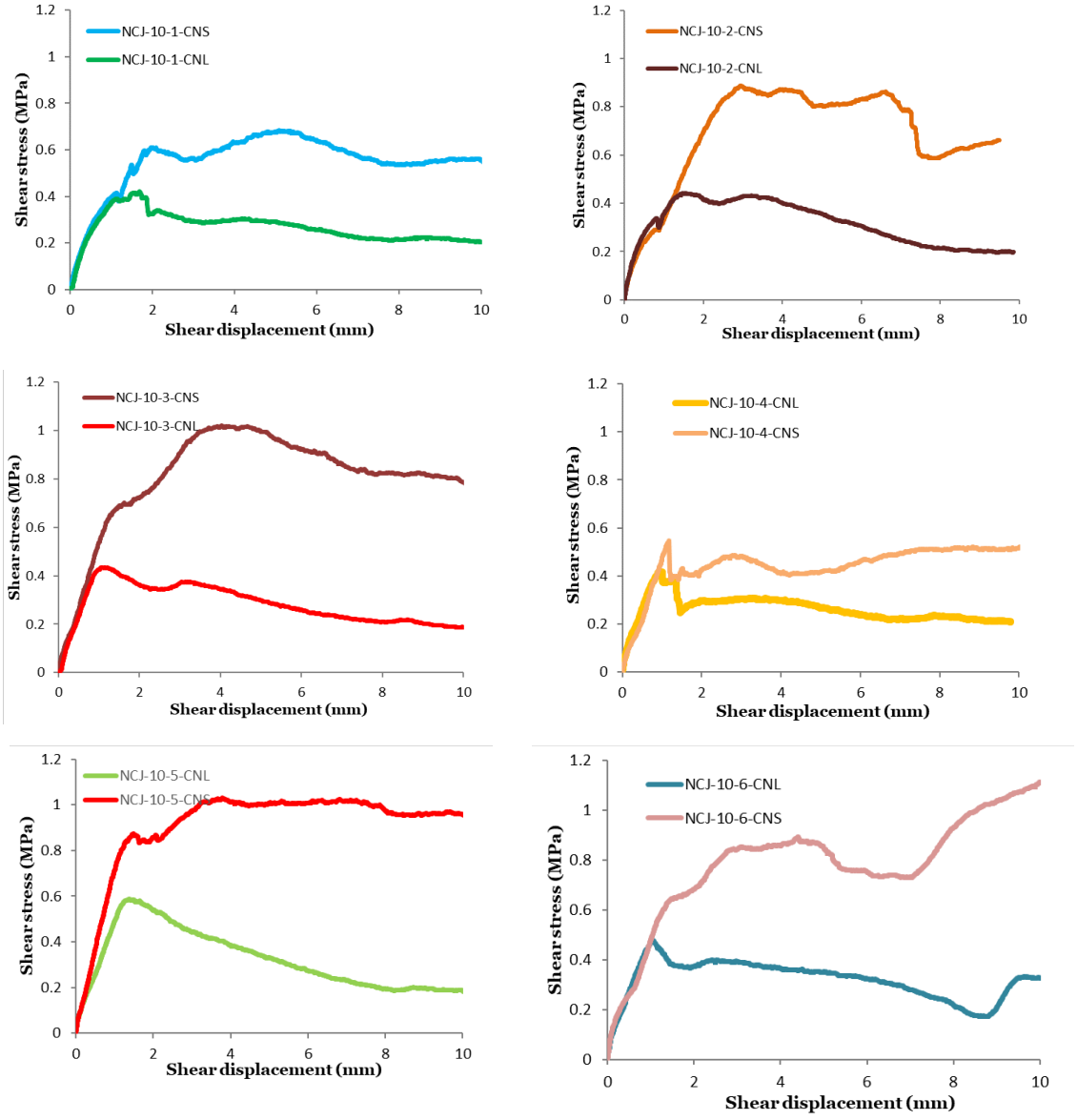

Figure 4.31. Comparison of shear stress vs. shear displacement for NCJ-10-1 to NCJ-10-6 in CNL and CNS conditions.

4.4.3 Analysis and discussion

For the rearranged profiles based on the original joint with JRC=6-8 (NCJ-4 profiles), the following observations are drawn:

The shear stress–displacement curves of the rearranged profiles are similar to the original joint with JRC=6-8, in CNL boundary conditions (Figure 4.23). These joints displayed a peak

shear stress followed by a slight post-peak softening. The maximum difference in shear strength of the NCJ-4s from the original geometry is 14%. The minor variation in the slope and amplitude statistical parameters didn't have a significant effect on the shear curves. Likewise, under CNS boundary conditions, the variations in the shape and magnitude of the shear curves were limited (Figure 4.24). The shear stress-shear displacement curves continued to gain strength until 10 mm of shear displacement. In both CNL and CNS conditions, NCJ-10-3 had the least magnitude of shear strength and dilation compared to other configurations. This may be explained by the lower value of Z'_2. From Figure 4.25 that compares the shear strength of the original and reconfigured surfaces of NCJ-4s in CNS and CNL conditions, it is seen that the stress plots initially followed the same path, illustrating a similar shape. This is where frictional resistance was being overcome by the asperities with no dilation noticeable. Once this point was reached, the asperities began to dilate, the applied normal stiffness was engaged, and stress plots diverged from each other in CNL and CNS conditions. The increase in shear stress was approximately 70% for NCJ-4-1 at 10 mm shear displacement in CNS compared to the maximum shear strength in CNL, and nearly doubled for the original JRC=6-8 profile.

Moving forward to the NCJ-10 profiles, based on the results of Figure 4.26 to Figure 4.31, these observations are made:

In CNL conditions, for the original JRC 18-20 joint and the new configured joints, to overcome frictional resistance all the profiles followed approximately the same slope in the shear stress-shear displacement curve. Additionally, the joints displayed brittle behaviour with a distinct peak shear stress followed by rapid post peak softening until reaching residual shear stress. For the CNS tests, the stress response for the new configured geometries differed significantly from the original joint. In all the plots, there was an initial peak in shear stress between 1 mm and 1.5 mm of shear displacement, however after that, each geometry configuration took a unique path: For the original 18-20 joint, there was a small drop in shear stress followed

by a second peak at 1.09 MPa of shear stress. This drop was more significant in NCJ-10-4, however the shear strength continued to increase until the end of the test. In NCJ-10-1 there was a peak at approximately 5 mm of shear and then it plateaued until the end of the test. For NCJ-10-2 the maximum peak strength occurred at approximately 3 mm of shear displacement and the shear stress decreased slightly until approximately 7 mm, then dropped significantly. For NCJ-10-3, NCJ-10-5, and NCJ-10-6 no drop was observed. For NCJ-10-3 the shear stress continued to increase until reaching maximum shear strength then declined in post-peak at a slower rate. In NCJ-10-5 the peak shear stress occurred at 3.7 mm shear displacement then decreased at a slow rate until the end of the test. For NCJ-10-6 however, after the second peak stress and post-peak decline, the shear stress continued to increase at a rapid rate. This was due to the profile tilting in the shear box. The same trend was observed in the shear stress curve in CNL conditions at approximately 9 mm of shear displacement, again due to tilting of the joint.

Comparing the behaviour of the original joint with JRC=18-20 in CNL and CNS conditions (Figure 4.30), it was found that in CNS, the maximum shear stress (second peak) increased by 114% compared to the maximum shear stress in CNL conditions. The shear stress-displacement curves in both boundary conditions followed the same path until at around 1.5 mm, where the peak shear strength of the CNL curve occurred, and a drop in shear stress in the CNS curve was observed.

Among the NCJ-10 profiles, NCJ-10-1 and NCJ-10-4 displayed the least magnitude of shear strength and dilation in both CNL and CNS conditions. In CNL conditions, the shear stress-shear displacement curves of these two profiles were similar, such that after reaching the peak shear stress, there was a major decline in shear stress post-peak. The peak shear stress decreased by 17% and %19 respectively in comparison with the original roughness profile. Based on the values of Z_2 and Z'_2, it was expected that these configurations would have the maximum shear strength, however the opposite was observed. Taking a closer look at the geometry of profiles NCJ-10-1 and

NCJ-10-4 (Figure 4.21 and Figure 4.22) reveals that in both surfaces the critical asperity (asperity with the highest inclination) was located at the end of the profiles. During the test, when the initial frictional resistance was overcome and the upper half of the joint wall rode up the lower half, normal stress was localized on these asperities and consequently they were sheared off (Figure 4.32). There was a distinct drop in the peak shear stress at this point, which resulted in overall lower dilation and shear strength.

Visual observation of the post-test surface of the NCJ-10's disclosed that some main damage areas were similar to the original roughness surface, however there were asperity failure patterns that were distinctly different from the original JRC 18-20 joint and unique to the specific joint geometry. That is why the stress and dilation curves showed distinct behaviours. Similar results were observed in Ueng et al. (2010) for direct shear tests on soft-rock replicas. In their study, Ueng et al. (2010) devised new geometries by taking saw-tooth joints, standard JRC joints and natural joints and either dividing the original joints, enlarging them or building a repeated assembly of the profiles. The specimen lengths were in the range of 75 to 300 mm. They observed different damage patterns on the new geometries and stated that the peak shear strength of the profiles depended on the geometry of that profile and not on the specimen size. The direct shear tests were conducted in CNL conditions.

Comparing the results of the joints with JRC=18-20, original and newly configured, with their counterparts with JRC=6-8, revealed that for JRC=18-20 profiles in CNL, there was significant strain softening after peak shear stress, signaling the failure of critical asperities. In CNS conditions, the response to the applied normal stiffness displayed much more variation in profiles with JRC=18-20 in comparison to JRC=6-8, which was evident in the shear stress- shear displacement plots. This was expected because as indicated by the higher slope and amplitude parameters, the JRC 18-20 joint is rougher and therefore the NCJ-10s that were created by rearranging the original joint resulted in surface roughness that digressed from the original

geometry in terms of placement of critical asperities. This is analyzed further in section 4.4.3.1. Similarly, in Ueng et al. (2010) where they assembled 2 and 3 repeated profiles from joints with JRC=4-6 and JRC=18-20, there was insignificant difference in the peak shear strength of the smoother joint, but disparities were noticed for the rougher joint. Moreover, the shear stress at 10 mm of shear displacement for NCJ-10-4, the lowest among the NCJ-10 profiles, was 1.5 times the value of shear stress for the average profiles of JRC 6-8 at the same shear displacement in CNS conditions. This was anticipated as the average Z_2 and Z'_2 for the JRC 18-20 profiles were approximately 2 times as large as the same parameters for JRC 6-8.

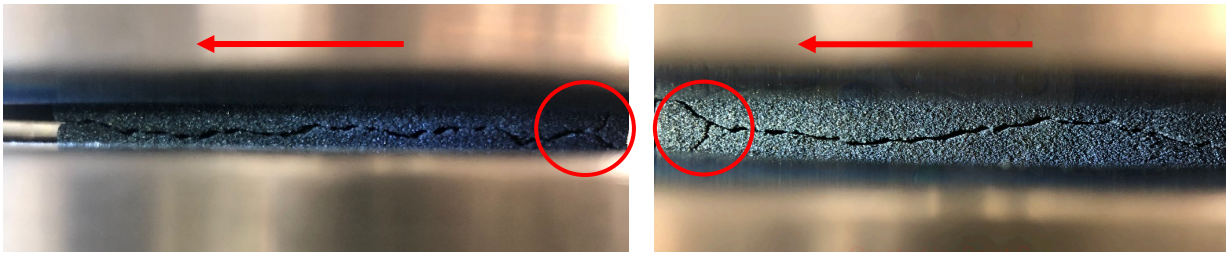

Figure 4.32. Failure patterns for NCJ-10-1 and NCJ-10-4. Notice the breaking of asperities located on the edge of the profiles.

In addition, when comparing the shear stress–shear displacement curves of the triangular profile in CNS conditions with the JRC 18-20 joints, original and rearranged, results showed that for the triangular profiles, post-peak strain softening happened at a higher rate. Similarly, Seidel and Haberfield (2002) noticed a more ductile response with lower shear strength in joints that had irregular patterns of roughness in comparison to saw-tooth joints with regular triangular asperities. The irregular joints had fractal geometry and the sawtooth joints had asperity angles ranging from 5^o to 27.5^o. This was because in irregular profiles, the asperities were made up of different angles that contributed to the shear strength at various stages of shear displacements. By contrast for sawtooth joints, all the triangular asperities contributed to peak shear strength concurrently. The profiles constituted of a soft synthetic rock for one joint surface and concrete for the other. The tests were conducted in CNS conditions with normal stiffnesses ranging from 0.150 MPa/mm to 0.600 MPa/mm. The effect of statistical parameters in describing the

roughness of the joints and their correlation with JRC is analyzed in more detail in the following section.

4.4.3.1 Estimating JRC values for the NCJs

As discussed previously in chapter 2, there are several ways to statistically define the roughness of a joint. Some parameters consider the amplitude and slope of the asperities. Among the statistical parameters that recognize the slope of the profile are the popular root mean square of the first derivative of the profile (Z_2) and the less common modified root mean square of the first derivative of the profile (Z'_2). Furthermore, because estimating the JRC values of a discontinuity based on the standard Barton and Choubey (1977) profiles are subjective (Beer et al., 2002), many researchers have attempted to correlate the JRC values with statistical parameters. The Z_2 and Z'_2 of the ten standard profiles are calculated and provided in Table 4.3. The calculated values are based on realigned profiles, digitized with sampling interval of 0.5 mm, obtained from Tatone (2014). The JRC values are plotted against the Z'_2 values for the standard profiles in Figure 4.33. An attempt was made to derive an equation for the relationship of JRCs based on the Z'_2 values. The following empirical equation was derived.

$$JRC = 67.77{Z'}_2^{\,0.4325} - 19.22 \tag{4.2}$$

where JRC is the joint roughness coefficient and Z'_2 is the modified root mean square of the first derivative of the profile. To achieve the JRC values for the newly configured joints (NCJs), Equations (2.15) to (2.19) and (2.21) from Chapter 2 pertaining to the Z_2 parameter and Equation (4.2) pertaining to the Z'_2 parameter was adopted. For the newly configured joints that were based on the 6-8 standard joint, i.e., NCJ-4 profiles, the JRC estimations are provided in Table 4.4.

Table 4.3. Z_2 and Z'_2 values for the standard JRC profiles

JRC	Precise JRC*	Z_2	Z'_2
0-2	0.4	0.0672	0.0518
2-4	2.8	0.1153	0.0889
4-6	5.8	0.1280	0.0938
6-8	6.7	0.1994	0.1460
8-10	9.5	0.1923	0.1433
10-12	10.8	0.2127	0.1399
12-14	12.8	0.2390	0.1615
14-16	14.5	0.2777	0.1812
16-18	16.7	0.3242	0.2006
18-20	18.7	0.3938	0.2820

*From Barton and Choubey (1977).

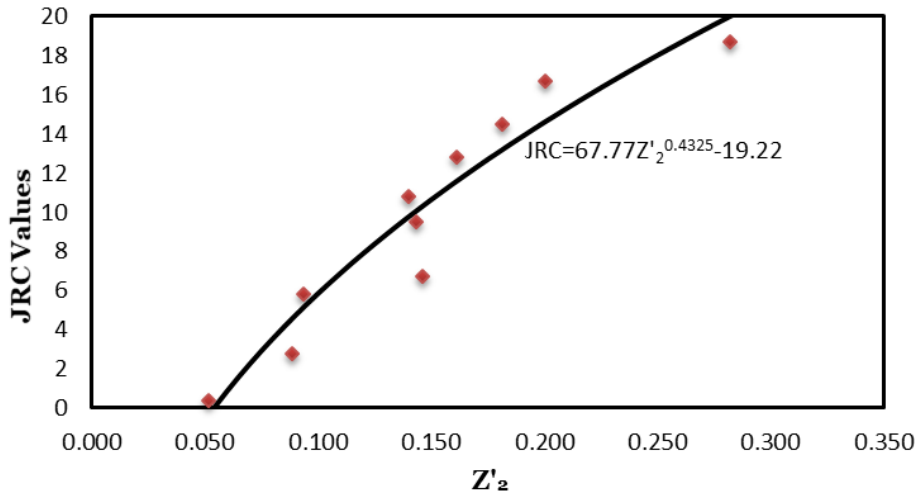

Figure 4.33. JRC values versus Z'_2 for the ten standard JRC profiles.

The difference in Z_2 for the NCJ-4s and the original JRC 6-8 profile is less than 1% and therefore the calculated JRC values are nearly identical. Of note is that the JRC values listed in Table 4.4 are mostly in the range of 8-10. This is because these values are obtained from empirical relationships based on the Z_2 and Z'_2 parameter. These parameters are higher for the standard

JRC 6-8 profile in comparison to its successor, the 5th standard profile with JRC 8-10, as shown in Table 4.3, therefore the calculated JRCs are higher than the actual value (6.7). However, the JRC values calculated based on Li and Zhang (2015) (Equation (2.21)), which is based on a wide range of joints, equals 7.0 which is closer to the original 6.7 value. Nevertheless, the objective here is to compare the relative JRC of the NCJs with the original joint geometry, and the actual value is less important. The difference between the Z'_2 of the NCJ-4s with the original geometry is between 2-11%, which is more significant than the difference bases on Z_2, and thereby reflected in the JRC values.

Table 4.4. JRC estimations based on empirical equations for NCJ-4s

Profile	Eq. (2.15)	Eq. (2.16)	Eq. (2.17)	Eq. (2.18)	Eq. (2.19)	Eq. (2.21)	Eq. (4.2)
Original JRC 6-8	9.6	8.9	9.5	9.5	9.3	7.0	10.3
NCJ-4-1	9.6	8.8	9.4	9.4	9.3	7.0	9.7
NCJ-4-2	9.6	8.9	9.5	9.5	9.4	7.0	10.5
NCJ-4-3	9.6	8.9	9.5	9.5	9.4	7.0	8.9

The estimated JRC values for the NCJ-10 profiles based on Z_2 (Equations (2.15) to (2.19) and (2.21)) and Z'_2 Equation (4.2) are listed in Table 4.5. The Z_2 value of the original JRC 18-20 and NCJ-10s (Table 4.2) differ by 3% maximum and thus there is minimal difference in the estimated JRC values of the newly configured joints based on Z_2. To put this variance into perspective, the difference between Z_2 of the original profile with JRC=18-20 and the standard profile immediately before it, i.e., profile with JRC=16-18, is 21%, and the difference between Z_2 of profile with JRC=16-18 and JRC=14-16 is 17% (Table 4.3). Therefore, based solely on the analysis of Z_2 and consequently the JRC values, it was speculated that the maximum shear strength of the NCJ-10s should be similar. However as previously illustrated, the stress-displacement plots and the shear strength of the new configured joints showed significant variation.

Next, comparing the Z'_2 of the profiles (Table 4.2) showed that the variation of this parameter is more pronounced. It is between 2% (for the original JRC 18-20 and NCJ-10-2) to 22% (for the original JRC 18-20 and NCJ-10-4). The JRCs estimated based on Z'_2 exhibit a larger variation compared to those calculated based on Z_2.

Table 4.5. JRC estimations based on empirical equations for NCJ-10s

Profile	Eq. (2.15)	Eq. (2.16)	Eq. (2.17)	Eq. (2.18)	Eq. (2.19)	Eq. (2.21)	Eq. (4.2)
Original 18-20	19.3	20.9	19.3	19.1	19.3	17.8	20.0
NCJ-10-1	19.4	21.0	19.4	19.2	19.4	18.0	21.8
NCJ-10-2	19.4	20.9	19.3	19.1	19.3	17.9	19.6
NCJ-10-3	19.3	20.9	19.3	19.1	19.3	17.8	20.3
NCJ-10-4	19.8	21.7	19.9	19.5	19.9	18.6	23.5
NCJ-10-5	19.3	20.9	19.3	19.1	19.3	17.8	20.3
NCJ-10-6	19.6	21.4	19.7	19.3	19.6	18.3	18.0

Thus far, the analysis of the profiles was based solely on the parameters describing the slopes of the surfaces. However, as Hong et al. (2008) mentioned, using only one attribute (slope or amplitude) to quantify the asperities may be inadequate in fully describing the roughness of a joint. Zhang et al. (2014) introduced a new roughness index, λ, that considers both directional slope and amplitude. They correlated JRC with this index and presented an average, upper bound and lower bound for their correlations. The JRC values corresponding to Z_2 and Z'_2 and λ of all the profiles are plotted in Figure 4.34. For the JRC calculated based on the Z_2, from Yang et al. (2001), Equation (2.15) is used. Also, for determining the JRC based on λ, for the 18-20 profiles (original and NCJs), Equation (2.24), and for the 6-8 profiles (original and NCJs), Equation (2.25) is adopted.

From Figure 4.34 several conclusions can be made: in comparing the JRC = 18-20 profiles (original and NCJ-10s), with the JRC = 6-8 profiles (original and NCJ-4s), there is more scatter in the JRCs for the NCJ-10 profiles than the NCJ-4 profiles. This shows that when a rougher

profile (18-20) is rearranged, the new profiles will have a more significant difference in terms of geometric properties compared with the original profile, than when the rearrangement takes place for a smoother profile (6-8). In other words, rearranging the JRC 6-8 profile, did *not* yield profiles that were significantly contrasting to the original profile. This was consistent with the stress-displacement and dilation – displacement results in both CNS and CNL conditions. Furthermore, the variations of Z_2 values of the NCJs are smaller in comparison to the Z'_2 and λ parameter. This shows that the Z_2 parameter cannot properly distinguish the geometric changes of the different configurations of the profiles.

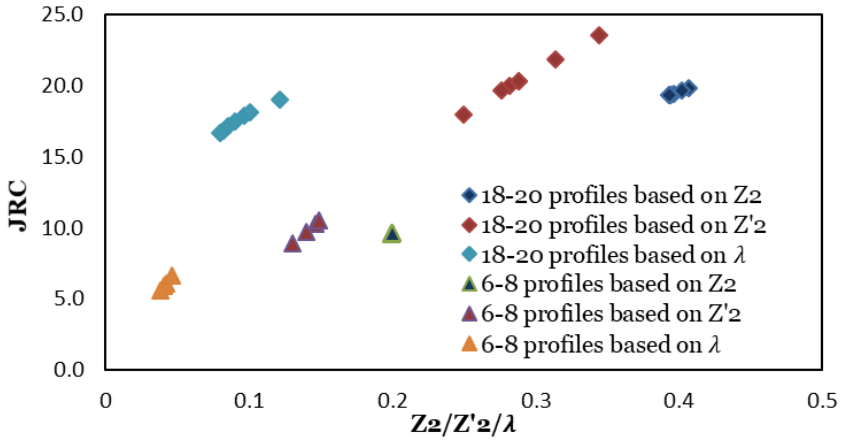

Figure 4.34. JRCs based on the Z_2, Z'_2 and λ of the original 6-8 and 18-20 and the different configurations (NCJs).

Finally, the JRCs obtained from Equations (2.24) and (2.25) were used as input parameters in Barton's equation, to compare the measured shear strength in CNL conditions with calculated ones. The results are depicted in Figure 4.35. Results indicate that predicted peak shear strength are close to those obtained in the lab. The biggest discrepancies are for NCJ-10-1 and NCJ-10-4, which as previously discussed, because the critical asperity is located near the edge of the profiles, due to local stress concentrations, the peak shear stress is lower than predicted. Thus, it is concluded that even though statistical height and shape parameters are effective in quantifying the roughness of a joint profile, however they are not enough. Further, the empirical method of

JRC may be adequate for determining the joint roughness of smoother joints, however for rougher joints, other factors such as distribution of stress on the asperities are critical and should be considered.

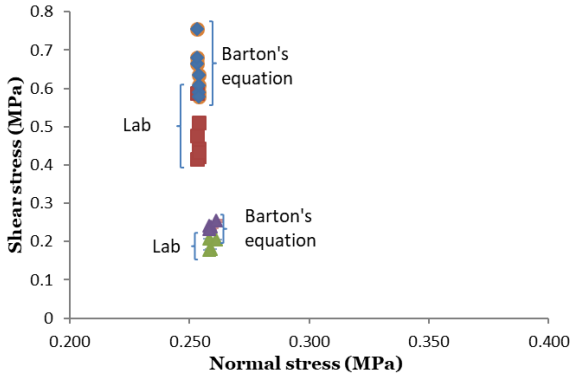

Figure 4.35. Comparison of laboratory peak shear strength with predicted shear strength based on Barton's equation.

4.4.3.2 Examining the dilation angles

In this section the change in dilation angles throughout the shear tests is investigated briefly. The incremental dilation angle for the shear tests is calculated as follows:

$$i = arctan\left(\Delta v / \Delta h\right) \tag{4.3}$$

where Δv and Δh are the increment of change in the vertical direction and shear direction, respectively. The dilation fluctuates throughout the test because as shear displacement advances, asperities come into contact, override each other and deform (Hencher and Richards, 2015). For this analysis the shear increment is chosen as 0.1 mm. Similar approach was taken by Johansson (2016). Figure 4.36, Figure 4.37 and Figure 4.38 illustrate the change in dilation angle with shear displacement for the original joint samples with JRC=18-20, NCJ-10-1 to NCJ-10-3 samples and NCJ-10-4 to NCJ-10-6 samples in CNL and CNS conditions, respectively. The shear stress curves are also drawn for comparison. Moreover, in Figure 4.39, Figure 4.40 and Figure 4.41, the instantaneous friction angle is plotted along with the incremental dilation angle.

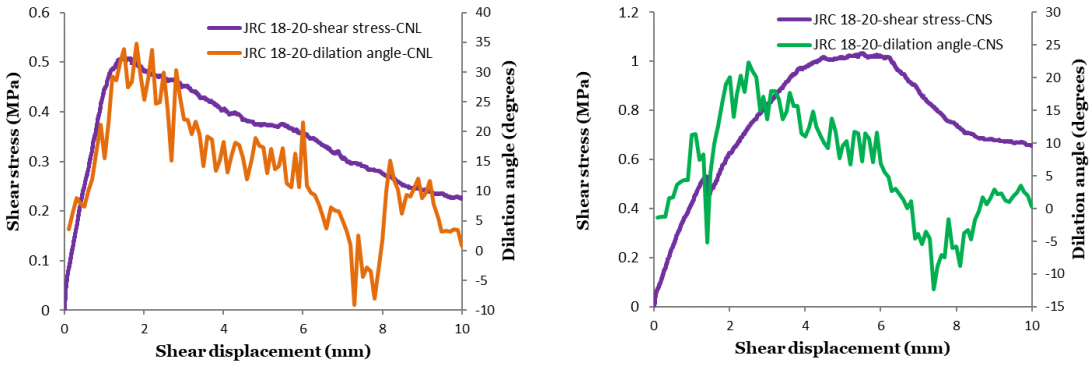

Figure 4.36. Dilation angle and shear stress vs. shear displacement for the original joint with JRC=18-20 in CNL and CNS conditions.

These figures found that in CNL boundary condition, the dilation angle curve followed the shear stress curve, which generally follows the instantaneous friction angle curve. As Hencher and Richards (2015) pointed out, this shows that the shear strength is dependent on incremental dilation. The dilation angle increases in the beginning of shear displacement until the shear peak shear stress is reached. After that, the dilation angle decreases. Johansson (2016) observed that in CNL conditions for tests conducted on unweathered granite, the dilation angle curve followed the total mobilized friction angle. This was because with the advance of shear displacement, the number of contact points decreased and became larger.

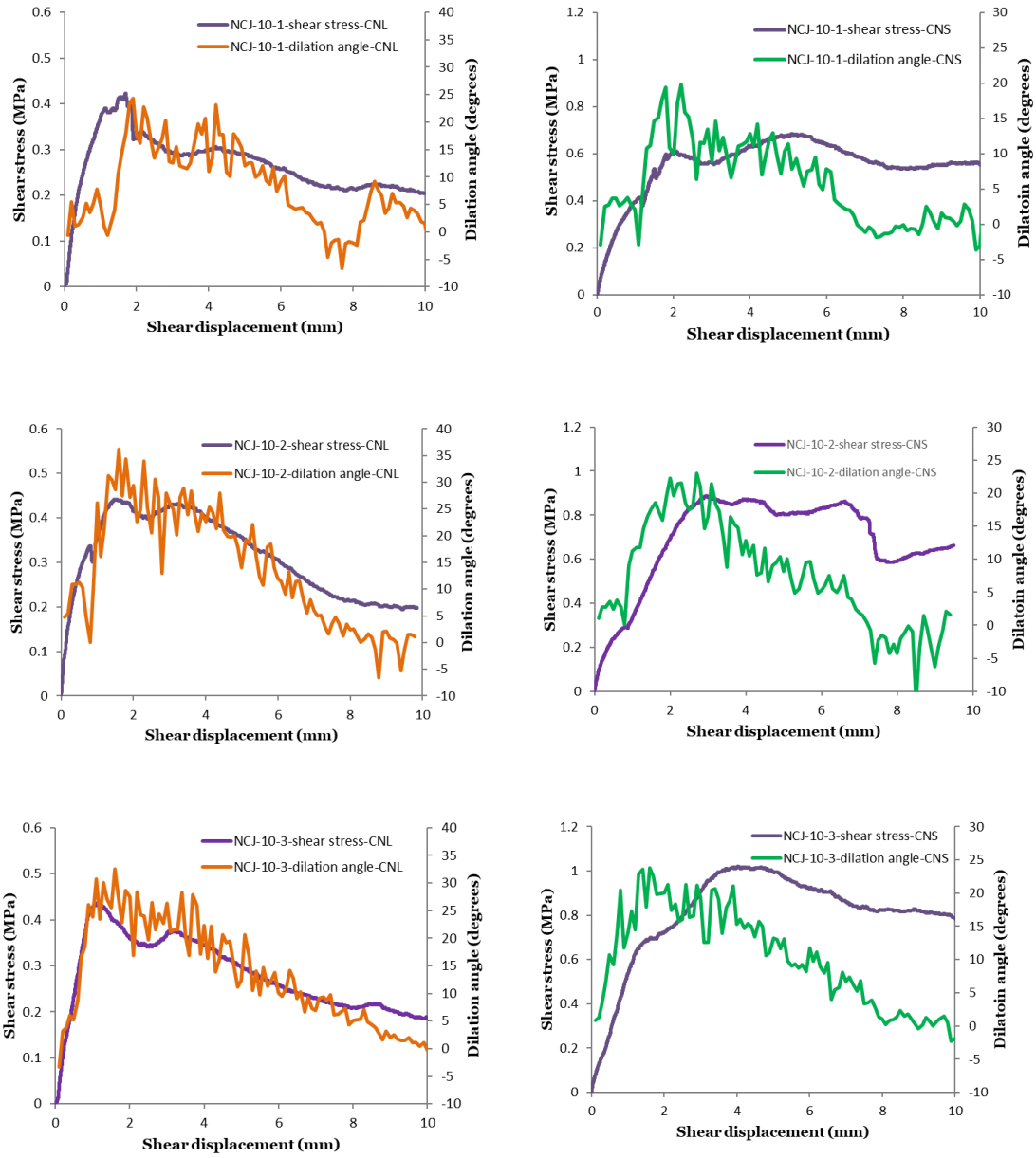

Figure 4.37. Dilation angle and shear stress vs. shear displacement for NCJ-10-1 to NCJ-10-3 in CNL and CNS conditions.

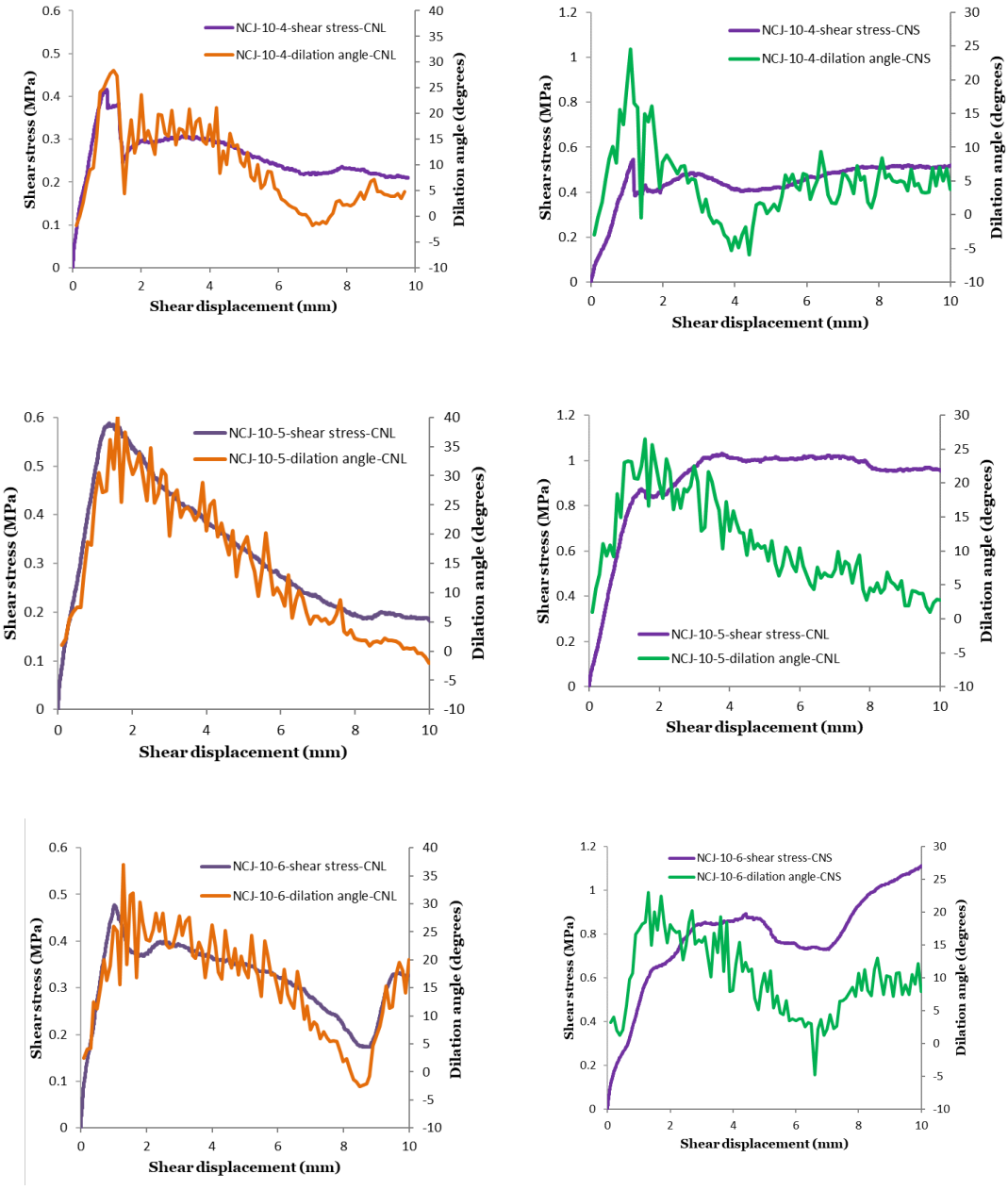

Figure 4.38. Dilation angle and shear stress vs. shear displacement for NCJ-10-4 to NCJ-10-6 in CNL and CNS conditions.

In CNS conditions, however, the incremental dilation angle curve diverged from the shear stress curve and instead generally followed the dilation angle curve in CNL conditions. Jiang et al. (2004a) also saw a decrease in dilation angle with the advent of shear displacement in both CNL and CNS boundary condition for a synthetic joint with UCS = 89.5 MPa and JRC=12-14. The CNS tests were carried out under normal stresses of 3 GPa/m and 7 GPa/m. In their study the CNL and CNS curves followed each other.

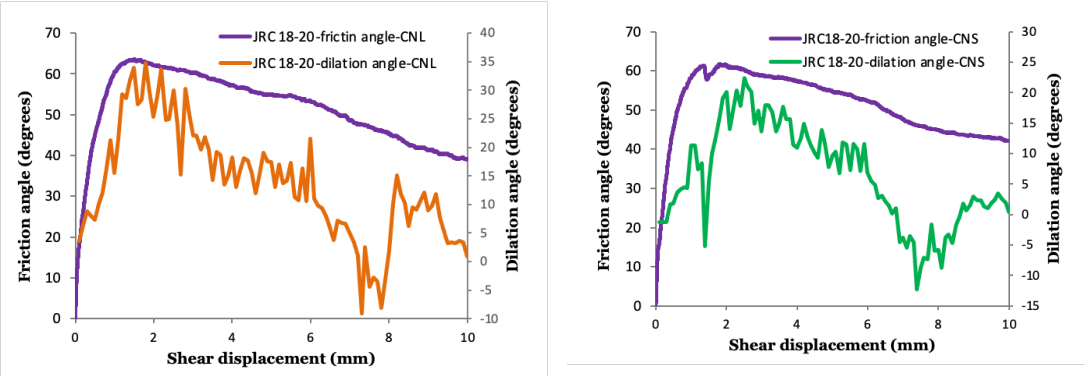

Figure 4.39. Dilation angle and friction angle vs. shear displacement for the original joint with JRC=18-20 in CNL and CNS conditions.

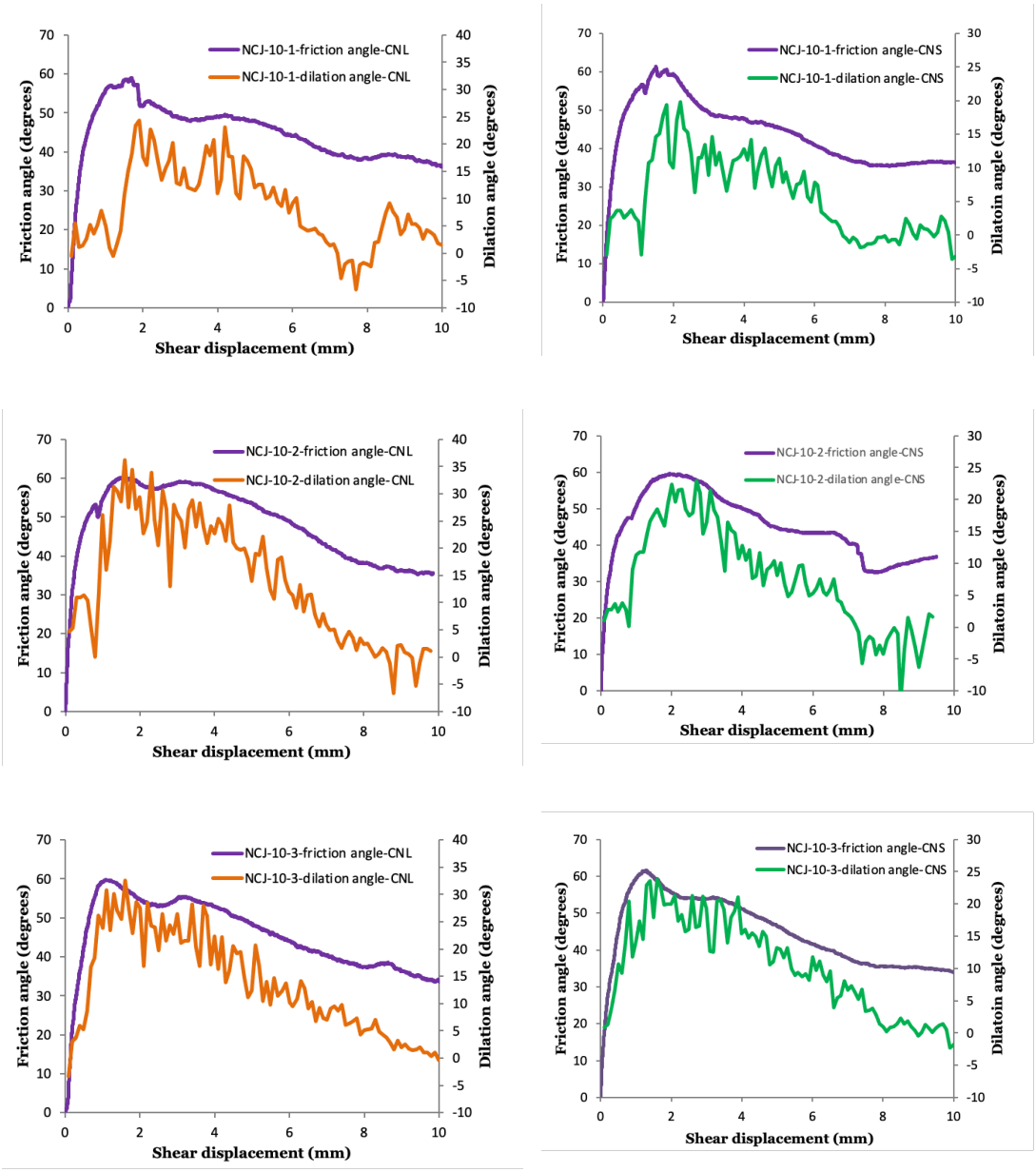

Figure 4.40. Dilation angle and friction angle vs. shear displacement for NCJ-10-1 to NCJ-10-3 in CNL and CNS conditions.

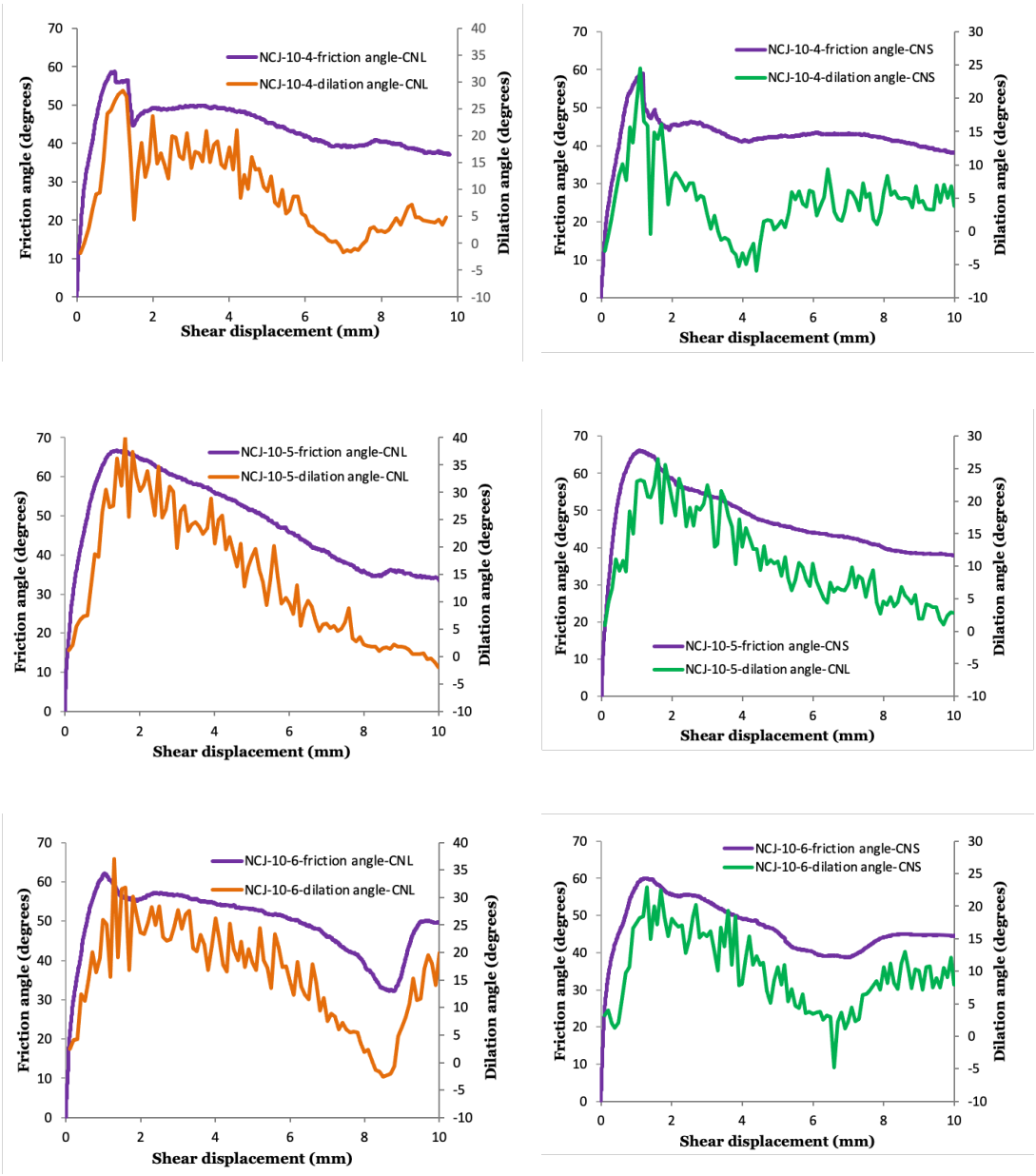

Figure 4.41. Dilation angle and friction angle vs. shear displacement for NCJ-10-4 to NCJ-10-6 in CNL and CNS conditions.

5 Numerical simulations

In a discrete element method (DEM) model using a program such as Particle Flow Code (PFC), to get the micromechanical response of a rock analogue, it would be favourable to insert the micro-properties of the intact rock directly from laboratory results. In fact, one of the motivations behind using 3D printed material to replicate rock is to obtain this goal, however this is not a straightforward task and requires more research. In this chapter, as an initial step, the micro mechanical mechanisms of failure of the 3D printed joint asperities in direct shear are investigated. For the calibration of the BPM, the traditional method of iterating the micro-properties of the particles and bonds to achieve the laboratory macro-properties is used. For this purpose, direct shear tests on three standard joint profiles presented in chapter 3, i.e., JRC 6-8, JRC 12-14 and JRC 18-20 are chosen and their shear stress- shear displacement and vertical displacement- shear displacement are numerically modeled. For the simulations, first the intact sample was generated, then the joint geometry was incorporated in the sample. After, the sample was inserted in the direct shear setup and direct shear tests were run. In this study only the constant normal load (CNL) boundary condition is investigated. All models are run in two dimensions.

5.1 Particle Flow Code – PFC

Based on Itasca (2008), Particle Flow Code (PFC) is a particle-flow model that simulates the behavior of a group of particles known as the synthetic material. These particles are rigid bodies, they slide and rotate independently and interact with each other at contact points. In PFC2D, the bodies are circular particles (disks of unit thickness) and two force components and one moment component can be applied. The PFC model also includes walls, which allows the application of boundary conditions such as velocity to the particles.

In DEM, the particles interact as a dynamic process represented by a timestep, where velocity and acceleration are constant during each timestep. In PFC an explicit finite difference method is used, and the particles follow Newton's second law and the force-displacement law is applied at the contacts (Itasca, 2008). The calculation cycle in PFC consists of a time-stepping algorithm where at each timestep, at first, from known wall and ball positions, the contacts are updated. Then, force – displacement laws are applied to the contacts to update the contact forces. This is done based on the relative displacement between the entities at contacts and the governing constitutive model. After, the velocity and position of the particles are updated based on the law of motion applied. Furthermore, based on the defined wall velocities, the wall positions are updated (Itasca, 2008).

Moreover, in the PFC model, particles may be bonded at contacts. The bonded material can be contact-bonded, parallel-bonded or flat-jointed (Potyondy, 2015). The parallel bond contact model simulates the behavior of cement like material lying between the particles. They can transmit both force and moment, while the contact bond only transmits a force. The parallel bonds are proposed as a set of elastic springs that are distributed over the contact plane. They are active over a finite rectangular section on the contact plane and centered at the contact point. Parallel bonds possess both constant normal and shear stiffnesses (Itasca, 2008). When there is relative movement at the contact between the two particles, due to the parallel-bond stiffness, a force and moment is developed on the bonded particles. When the maximum normal or shear stresses within the parallel bond exceeds the strength limit of the bonded parallel bond, the bond breaks and becomes unbonded and no longer resists rotation (Itasca, 2008).

Initially joints were simulated by removing the bond between the particles that represent the joint (Cundall, 2000). However, the interface surfaces in PFC models have an inherent roughness resulting from circular particles that created undesired roughness in the geometry. To solve this problem, the smooth-joint contact model can be incorporated to simulate a

discontinuity in the material assembly (Pierce et al., 2007). The smooth-joints are applied on the contacts of the balls that lie on either side of the joint. This model allows particles to slide past each other without riding on top of each other (Figure 5.1). The alignment of sliding is consistent with the joint, regardless of the orientation of the contacts along the joint. Smooth-joints can simulate the behavior of frictional or bonded joints (Itasca, 2008).

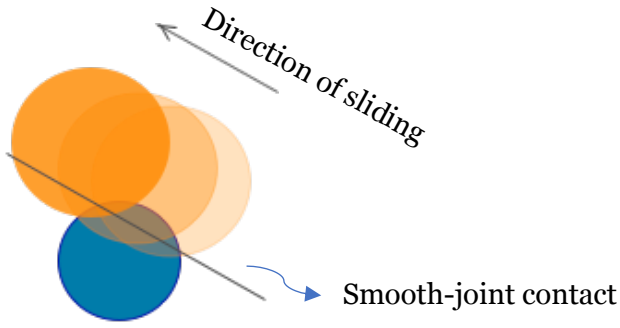

Figure 5.1. Sliding of two balls (particles) on opposite side of a smooth-joint contact.

5.2 Material genesis and calibration

First, the intact material was created and calibrated. In this study, based on literature available on direct shear tests in PFC (e.g., Bahaaddini et al., 2013, Lambert and Coll, 2014, Lazzari et al., 2014, Bayona et al., 2018) and to limit the number of properties that needed to be assigned for calibration, parallel bonds were used. The bonded particle model (BPM) was created using the material genesis functions available in PFC. The material generation process is summarized below (Itasca, 2008):

1- A material vessel is constructed and filled with randomly placed particles. The particle diameters are chosen such that they satisfy a uniform particle size distribution. The particles rearrange and the system reaches static equilibrium with zero particle friction. In this section a compact initial assembly is created.

2- The diameter of the particles is changed uniformly to attain a specified isotropic stress (which is usually less than one percent of uniaxial compressive strength). The objective is to reduce the magnitude of locked-in stresses.
3- The “floating” particles, which are particles in the assembly that have less than 3 contacts are eliminated. This is done to obtain a denser packed material.
4- Parallel bonds are instated between the particles that are in near proximity of each other and particle friction coefficient is assigned. The specimen is removed from the material vessel and allowed to reach static equilibrium.

The micro-properties of the particles and contact bonds were adjusted in an iterative process such that the macro-properties (deformability and strength) of the BPM were in accordance with the laboratory experiments conducted on the 3D printed rock proxies. In this study the intact rock was calibrated to the uniaxial compressive strength of the rock proxies (Bahaaddini et al., 2013, Lazzari et al., 2014, Bahaaddini et al., 2016, Mehranpour and Kulatilake, 2017). Thus, a synthetic specimen with the size of approximately 135 mm x 54 mm was generated, representing the size of the specimen tested in laboratory experiments. Based on an iterative process the micro-properties were adjusted, and macro-properties achieved. Table 5.1 shows the micro-parameters used for the particles and parallel bonds in the synthetic material. UCS = 39.8 MPa and E = 3.29 GPa was obtained which is close to the laboratory values (chapter 3).

Table 5.1. Micro-scale properties of particle and bonds of the BPM

Particle properties	
Ball Density (kg/m^3)	2650
Particle contact modulus (GPa)	2.25
Coefficient of friction	0.5
Normal to shear stiffness ratio	1.8
Parallel bond properties	
Parallel bond modulus (GPa)	2.25
Normal to shear stiffness ratio	1.8
Normal strength, mean (MPa)	28
Normal strength, SD (MPa)	5.6
Shear strength, mean (MPa)	28
Shear strength, SD (MPa)	5.6

5.3 Direct shear tests

After calibrating the intact material, direct shear tests for three standard geometries under CNL conditions were simulated. The functions for the direct shear tests in the PFC program were based on Bewick (2013), but further modified to accommodate the specific test functions and requirements in this study. The sample generation and test setup and comparison with laboratory experiments are discussed below.

5.3.1 Direct shear setup

The shear box specimen with height of 40 mm and length of approximately 100 mm (the actual length differs slightly for each joint geometry) was constructed. The shear setup is presented in Figure 5.2. The top block is kept stationary during the test and a constant horizontal velocity is applied to the bottom block, shearing the specimen. The shear displacement is determined by measuring the horizontal displacement of the bottom block. The applied shear velocity is 0.1 m/s, so that the specimen maintains quasi-static equilibrium (Cho, 2008, Bahaaddini et al., 2013). The normal stress is applied to the specimen using the top wall (wall 2) and during the test, this stress is kept constant using a servo mechanism. The shear stress is

calculated by dividing the reaction force on wall 4 by specimen length. Normal displacement is measured by the normal displacement of wall 2.

Three standard joint profiles from Barton and Choubey (1977) were used in the direct shear simulations. They included joint profiles with JRC=6-8, JRC=12-14 and JRC=18-20. The profiles were digitized and the x- and y- coordinates were extracted. This data was taken from Tatone (2014). The joint geometry was implemented into the rock model using smooth-joints. As mentioned, the smooth-joint which is a set of springs that are distributed over a rectangular cross-section, is assigned to particle-particle contacts that lie on the opposite sides of the joint plane. The smooth-joints override the artificial roughness generated by the discrete nature of the particles in the joint surface and allows particles to slide past each other. The joints in this model are unbonded and have no cohesion.

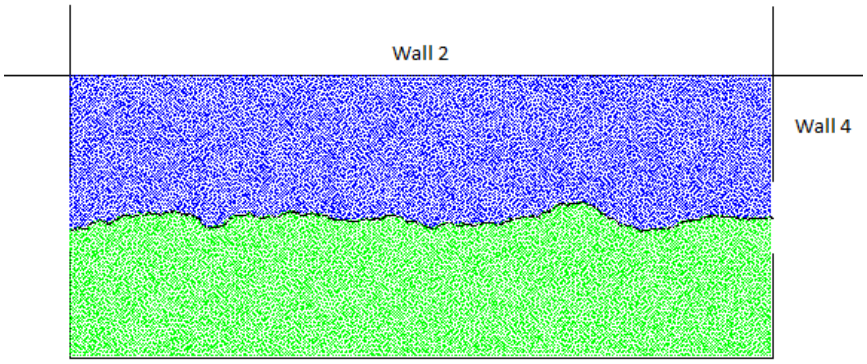

Figure 5.2. Direct shear setup in PFC.

Because smooth-joint contacts are implemented on balls that are located on opposite sides of the joint plane at the start of the test, a problem is caused that was realized by Bahaaddini et al. (2013). They mentioned that this default implementation method caused "lock up" points when for example, due to normal load applications, the two balls that were initially on opposite sides of the joint plane were placed on the same side. In this event, a smooth-joint was no longer implemented between the balls and thus, unrealistic stress concentrations occurred within the

model. To avoid this issue, they suggested a shear box genesis approach where the top and bottom blocks of the shear specimen are created separately. Therefore, during shear, whenever balls from the top and bottom blocks come into contact, a smooth-joint is implemented. In this study the same logic is used. However, to simplify the sample preparation, the specimen is created in one block, and a condition is applied for implementing smooth-joint contacts: The balls that are located on the upper joint plane are put into a group called "upper joint balls" and the particles that are generated on the bottom joint plane are grouped as "lower joint balls". Then the model is programmed to insert a smooth-joint contact whenever the balls from the "upper joint balls" and "lower joint balls" come into contact. A method similar to this was also incorporated by Mehranpour and Kulatilake (2017).

To simulate the tests, first a direct shear test for the joint profile with JRC=18-20 under 0.25 MPa applied normal stress was modeled. The smooth-joint parameters were adjusted to match the measured peak shear strength. Then the rest of the shear tests were simulated using the same parameters. The smooth-joint micro-parameters are listed in Table 5.2.

Table 5.2. Micro-scale properties of smooth-joints

Property	value
Joint normal stiffness (MPa/mm)	200
Joint shear stiffness (MPa/mm)	6
Friction coefficient	0.57

5.3.2 Results

The shear stress and vertical displacement versus shear displacement curves of the joint with JRC 18-20 under 0.25 MPa applied normal stress are illustrated in Figure 5.3. These plots found that the trend of the stress-displacement curve was similar to the laboratory curve. As shown in the stress-displacement plot in the PFC model, the shear stress increased steadily, reached its peak value at 0.497 MPa, and then gradually declined. The peak shear stress of the

simulation showed good agreement with laboratory results. For the dilation-horizontal displacement plot, the general shape of the curves for the model and laboratory was similar, although the dilation values of the simulation were higher than the experiments.

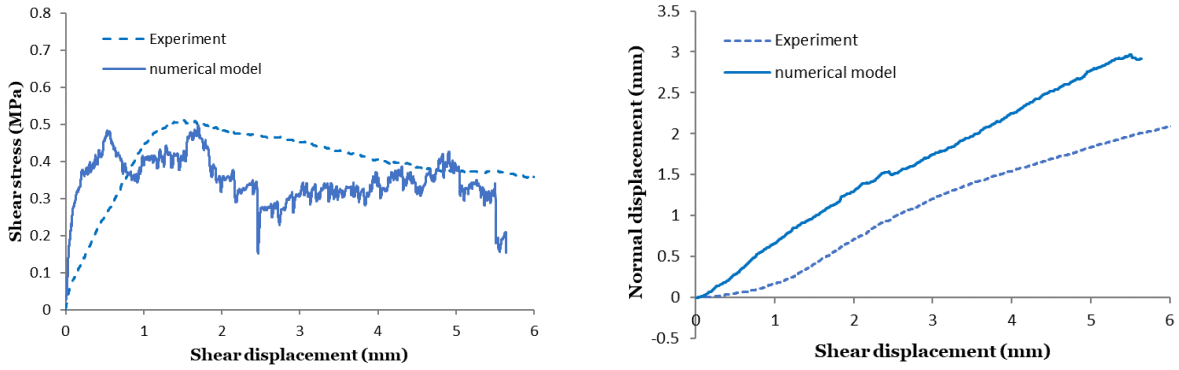

Figure 5.3. Shear stress and normal displacement versus shear displacement plots for joint with JRC 18-20 under 0.25 MPa applied normal stress: experiment vs. numerical model.

However, there were some discrepancies. For example, the shear stiffness of the simulation was less than the laboratory plot. Also, the shear stress curve, after overcoming initial friction, exhibited some "jaggedness" and was not as smooth as the laboratory plots. These drops might be the result of simulating in 2D. The laboratory samples are good candidates for 2D simulations because the geometry of the standard profiles was elongated across the width of the joint surface, forming a uniform cross-section. However, the difference between laboratory tests and simulations was that in experiments whenever an asperity failed, the applied stresses were transferred to the surrounding asperities. Yet, in PFC simulations, only the asperities along the length of the profile could carry stress which might explain the jaggedness of the curves. Similar observations were made by Tatone (2014). The shear box is illustrated in Figure 5.4 for the end of the shear test. From this figure, it is seen that the top block is sliding over the lower block and the cracks are located on the critical asperities. Also, the cracks are concentrated on the surface of the asperities. Because of the applied normal stress of 0.25 MPa, which is relatively low, this was expected and agreed with visual observations in the experiment.

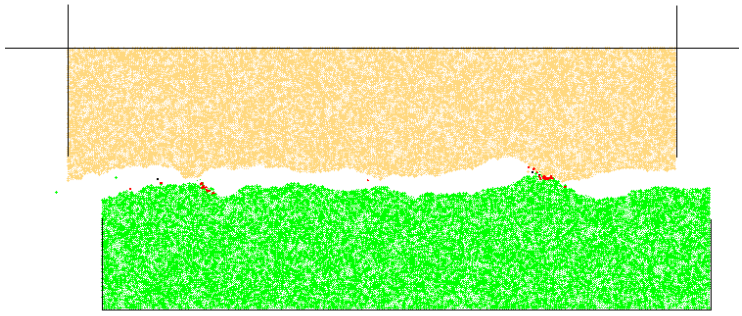

Figure 5.4. Sliding of the upper block over the lower block and concentration of cracks on critical asperities for joint with JRC 18-20 under 0.25 MPa applied normal stress.

The shear stress and dilation versus shear displacement for the joints with JRC 12-14 and JRC 6-8 under 0.25 MPa applied normal stress are plotted in Figure 5.5 and Figure 5.6. These simulations also captured the trend of shear stress vs. shear displacement behavior of laboratory tests; however, the peak shear stress is underestimated for JRC=12-14 and overestimated for JRC=6-8. The normal dilations are slightly overestimated for both profiles.

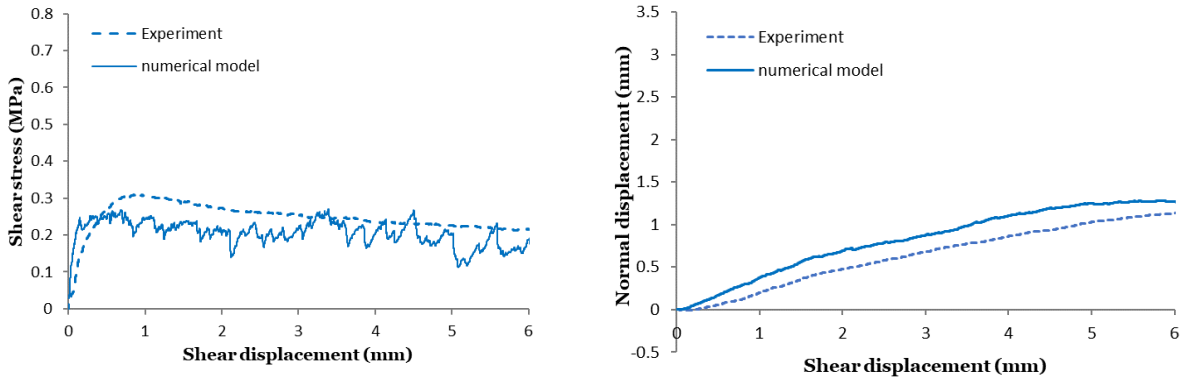

Figure 5.5. Shear stress and normal displacement versus shear displacement plots for joint with JRC =12-14 under 0.25 MPa applied normal stress: experiment vs. numerical model.

The shear stress–displacement and dilation–displacement graphs for simulated joints with JRC 6-8, JRC 12-14 and JRC 18-20 under applied normal stress of 0.25 MPa, 0.5 MPa and 1 MPa are plotted in Figure 5.7. From these graphs, the simulation results showed that, as observed in

measurements, there is a positive correlation between the increase of applied normal stress and peak shear stress. Also, under all stress magnitudes, and for all geometries, dilatancy occurred.

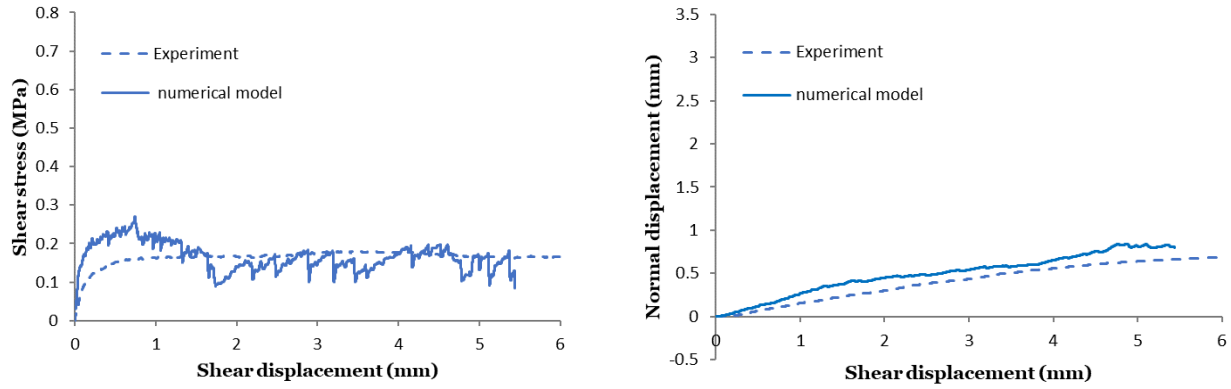

Figure 5.6. Shear stress and normal displacement versus shear displacement plots for joint with JRC=6-8 under 0.25 MPa applied normal stress: experiment vs. numerical model.

The magnitude of dilation decreased with the increase of normal stress and for joints with lower surface roughness, dilation was less prominent. The asperity failure for all the joints at the end of the direct shear tests under applied normal stress of 0.5 MPa and 1 MPa are depicted in Figure 5.8. The location of crack concentration post-shear was on critical asperities and generally mimicked those of laboratory results. The accumulation of damage in the specimen and the evolution of cracks from the surface of the asperities into the intact rock is attributed to the higher applied normal stresses. Most of the cracks were tensile cracks. This showed that PFC can simulate crack initiation and propagation in direct shear tests.

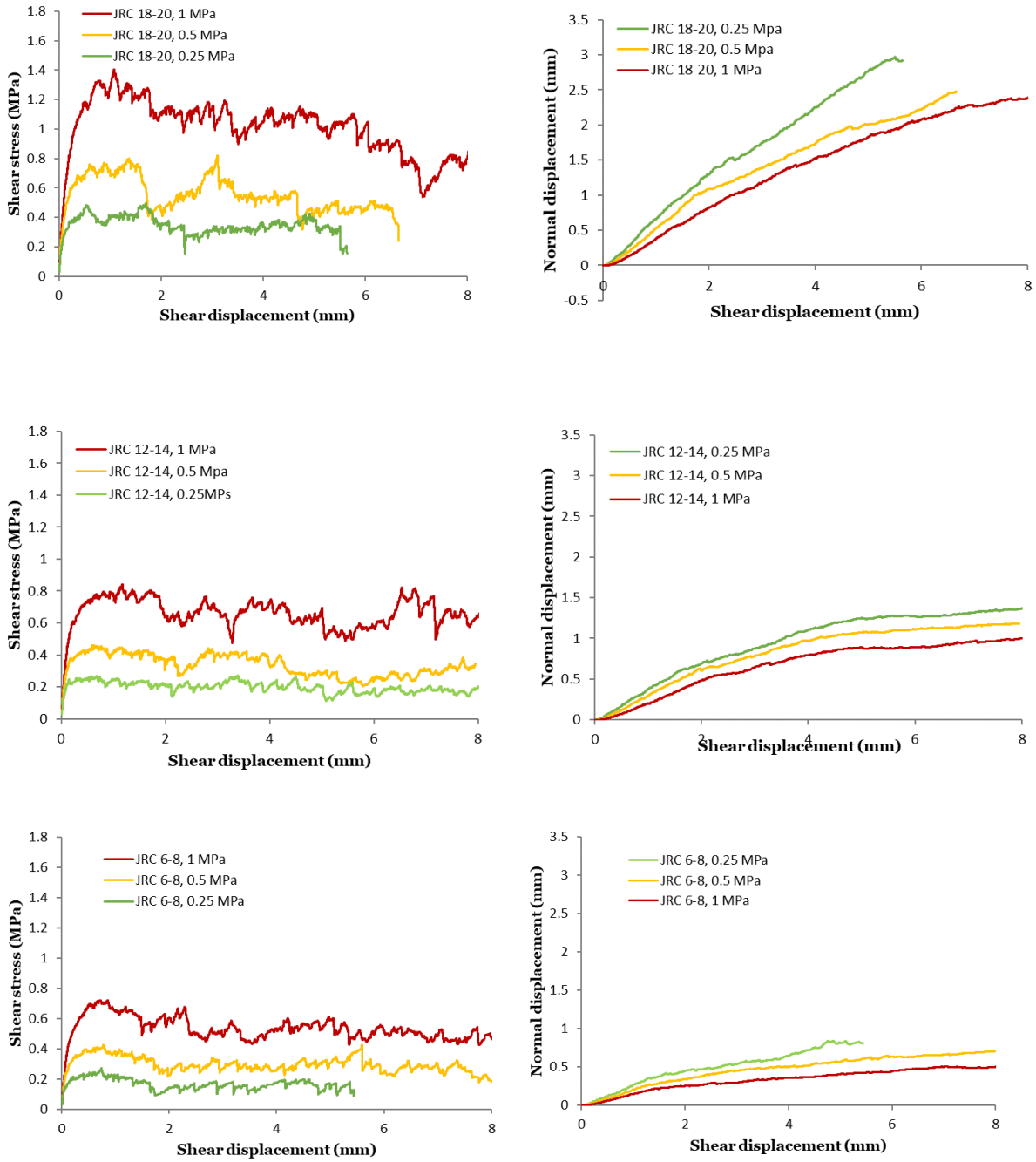

Figure 5.7. Simulations of shear stress and normal displacement versus shear displacement plots for joints with JRC 6-8, 12-14 and 18-20 under various applied normal stresses.

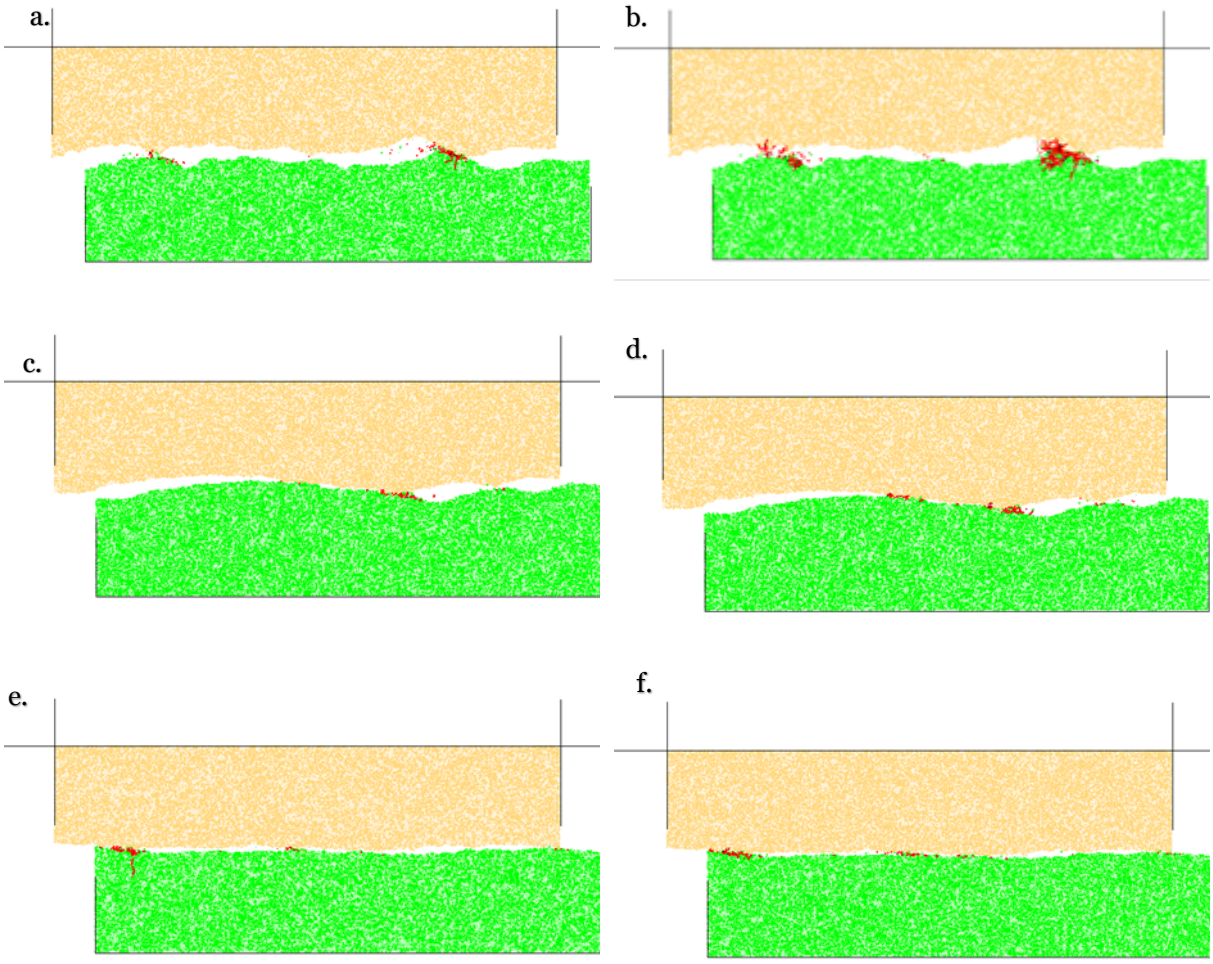

Figure 5.8. Asperity failure and formation of cracks at the end of direct shear tests: a. joint with JRC 18-20 under 0.5 MPa applied normal stress b. joint with JRC 18-20 under 1 MPa applied normal stress c. joint with JRC 12-14 under 0.5 MPa applied normal stress d. joint with JRC 12-14 under 1 MPa applied normal stress e. joint with JRC 6-8 under 0.5 MPa applied normal stress f. joint with JRC 6-8 under 1 MPa applied normal stress.

5.3.3 Analysis and discussion

The peak shear stress of the simulations is compared to the Barton-Bandis model (Barton and Choubey, 1977) in Figure 5.9. From these graphs it is seen that generally the peak shear stress is underestimated by the PFC model. Even though PFC was able to simulate the overall stress – displacement behavior of the joints, however there were considerable differences between the

laboratory results and numerical simulations. Some possible reasons for these discrepancies are discussed further:

As mentioned, one of the motivations to use 3D printed specimen to replicate rock is to input the particle and bond parameters directly into PFC to obtain the rock macro-properties and simulate macro behaviour. In this regard an attempt was made by Hodder (2017) where he simulated unconfined compression tests of 3D printed samples in PFC3D. He entered the indentation elastic modulus of the poly-furfuryl alcohol directly as a micro-property into the model. His results showed that the macro Young's modulus of the simulation was in the range of laboratory results however the UCS was greatly underestimated which was attributed to the use of spherical particles in PFC and the difference in the width of the parallel bonds in the simulations with the binder surrounding the sand particles in the printed proxies. This shows that further research is needed into inputting micro-parameters from lab into the simulations and obtaining the correct macro behaviour. In the current research, as per most studies, the micro parameters were altered on a trial and error basis to match the macro properties of the prints. It is postulated that if the micro-properties of the particles and bonds are input for the intact rock, the simulations of direct shear tests on the joints would be closer to the measured results. Moreover, due to the nature of the printing process where the sand and binder are deposited in layers, the printed specimens are anisotropic with weaker interlayer bonds. This anisotropy was not considered in the material genesis.

Furthermore, parallel bonds were used as the cementation between the particles. It is hypothesized that in real rock, the failure in the vicinity of the joint surface is dominated by the tensile strength (Grasselli and Egger, 2003). However, when parallel bonds are applied, the ratio of unconfined compressive strength to the tensile strength of the simulations differs from the actual rock and tensile strength is overestimated (Potyondy, 2012). Utilizing flat-joints may better represent the joint samples and simulate the fracture mechanism better.

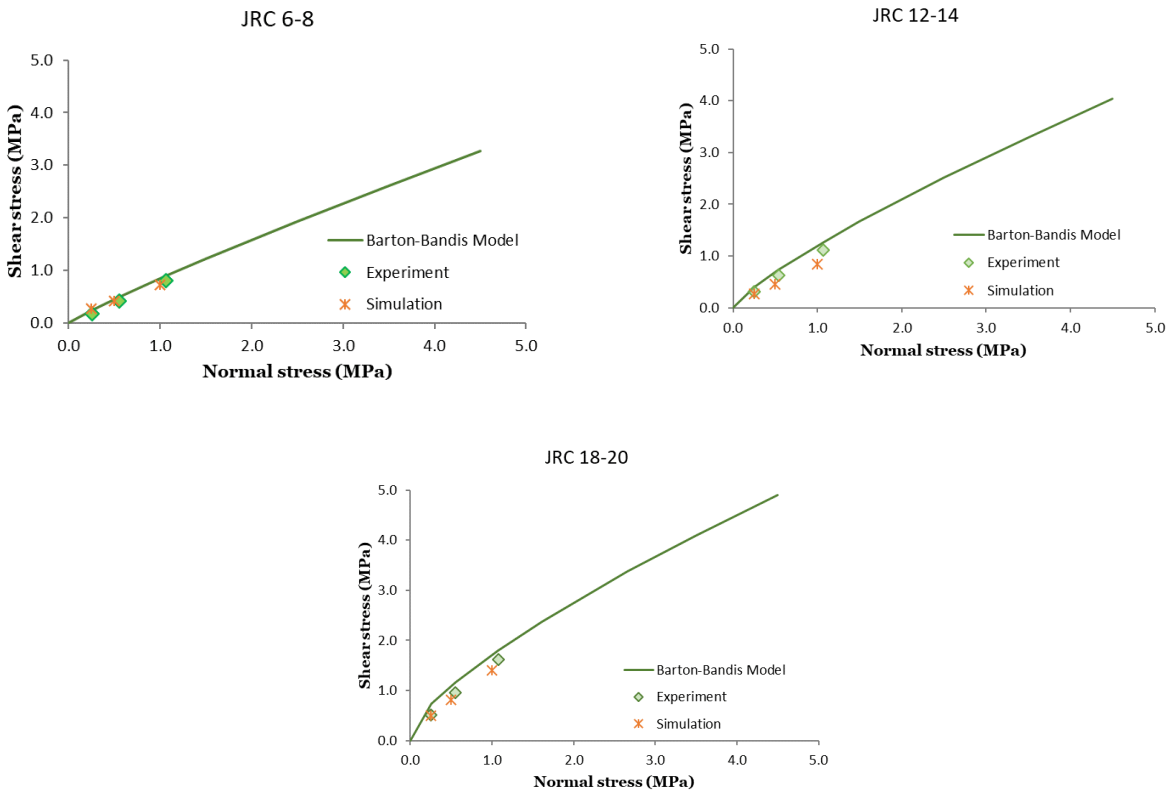

Figure 5.9. Comparison of peak shear stress of PFC simulations with Barton-Bandis model.

One other issue that was noted in the simulations is that the shear blocks were not allowed to rotate or tilt when shearing (Figure 5.8). This was different from laboratory experiments where signs of sample tilting were clear. Similar observations were made by Bayona et al. (2018).

Last and very critical is the incorporation of smooth- joints in PFC. Even though the use of smooth-joints and their use as jointed surfaces solved many issues with interlocking particles and roughness, however, the way the smooth-joints are implemented, and their properties significantly impact the shear stress and normal displacement of the direct shear test simulations. In this research, based on Bahaaddini et al. (2013) and similar to Mehranpour and Kulatilake (2017), the smooth-joint particles were grouped into upper and lower particles. This method was easier to implement compared to the Bahaaddini et al. (2013) method of creating two separate

blocks, however, there was an issue with the alignment of the smooth-joint to the actual joint geometry. As seen in Figure 5.10, for every section of the joint geometry, the smooth-joints align with the orientation of that section. But because the particles on each side of the joint are not aligned with each other, therefore the smooth-joint that is implemented between the particles will not be in one line. This problem does not exist in the Bahaaddini et al. (2013) method, because, as seen in Figure 5.10, the upper and lower sections are generated separately. However, Mehranpour and Kulatilake (2017) mentioned that in the Bahaaddini et al. (2013) method, the number of smooth-joint contacts are fewer than the previous method. In the Author's opinion, it is speculated that under higher normal stress applications, this would not be an issue, because the particles on the top layer would come into contact with the bottom layer, and thus the number of smooth-joints would increase prior to shearing. However, more investigation is needed. One other issue that exists with inserting smooth-joints between the upper group and lower group of particles, is that the value of smooth-joint normal stiffness becomes critical. Since all the balls above the joint profile are grouped into one block and the particles below the joint profile are placed into the lower block, then, potentially when any ball on the upper block reaches any ball on the lower block, a smooth-joint is inserted. In this case, if the value of smooth-joint normal stiffness is not high enough (and the applied normal stress is important because the value of normal stiffness would be evaluated relative to the applied normal stress), then, the upper block would "sink in" into the lower block and vertical dilation would be impacted, and in extreme cases the sample would compact. One potential way to solve this problem is to define an area above and below the joint profile and define particles located in that area as the ones that would participate in shear and apply the condition of smooth-joint application to those particles. Bayona et al. (2018) mentioned that they had to increase the value of smooth-joint normal stiffness in order to avoid particle interlocking. These issues grant further investigation.

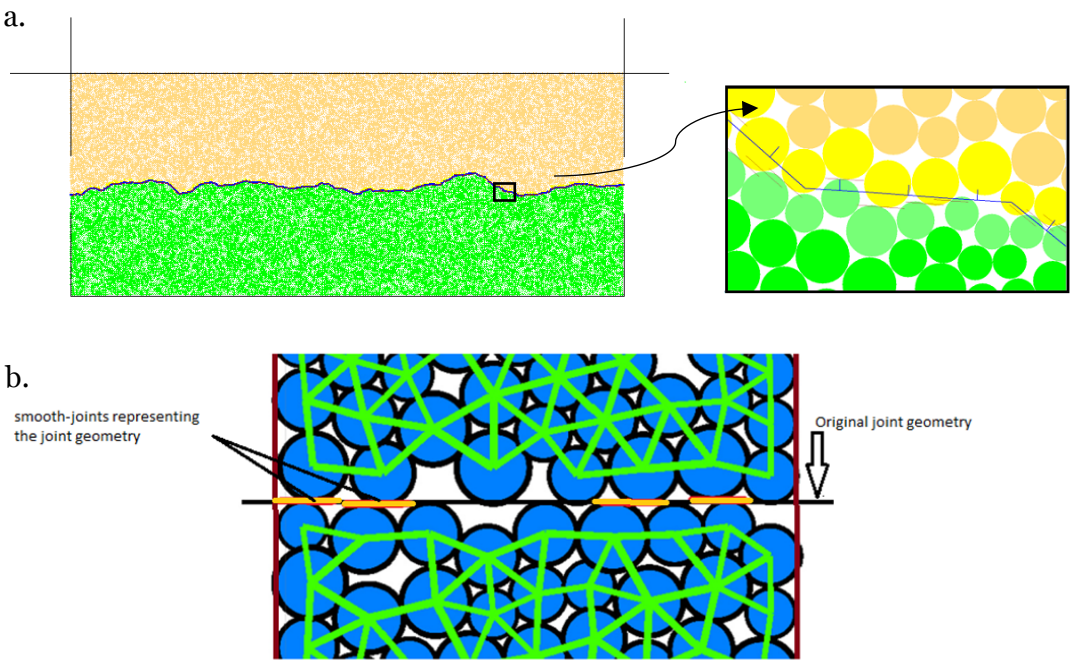

Figure 5.10. Implementation of smooth-joints in the model: a. in this research for joint with JRC=18-20, where because the balls are not aligned, the smooth-joint would not be aligned b. the Bahaaddini et al. (2013) method where the smooth-joints are completely aligned (modified from Mehranpour and Kulatilake, 2017).

6 Conclusion and future work

Through this research program the use of additive manufacturing technology, with an emphasis on the binder jetting process, in replicating rocks and rock fractures was explored. Further, the effect of surface geometry components on joint shear strength and dilation in CNL and CNS boundary conditions was studied using 3D printed sand proxies.

The use of 3D printing in creating reliable samples for rock analogues is fairly new, and the compressive strengths reported in the literature for specimen fabricated with powder-based material has been generally low. Therefore, the first objective of this thesis was to study the factors that contributed to the print properties in a powder-based printing setup using the binder jetting process, and to modify and select the print configurations and post processes to achieve higher compressive strengths. To obtain this objective, sand specimens were fabricated with a 3D printing machine that deposited activated silica sand powder and binder in layers. Parallel studies to this research showed that higher binder saturations led to higher compressive strength up to saturation levels of 20%, where the resolution of the prints decreased. Also, that heat-curing removed the excess water in the samples and increased mechanical strength. Based on these factors and findings, the printed samples were fabricated with 20% saturation and heat-cured during the printing process, then cured in the oven at 80^{o}C for 65 hours. Strength tests were performed on the printed specimens and results showed that the stress-strain plots exhibited behaviour similar to natural rock. The obtained strength parameters were UCS= 40.2 MPa, E=3.27 GPa and BTS = 7.4 MPa. This obtained UCS was higher than other powder-based printed rock analogues reported previously in literature. However, this material was classified as having low modulus ratio (E/UCS< 200) and low UCS to indirect tensile strength ratio (UCS/BTS <8). This was likely due to the large pore space present in the structure of printed specimens and the strong bonds that developed at sand grain contacts. The strength and deformation parameters

obtained for the sand analogues were close to Baerloch sandstones in Switzerland. Overall, it was concluded that the sand analogues were suitable for replicating natural rock.

To further increase the strength of the printed specimen, it was hypothesised that due to the large pore space present in the prints, infiltrating the sample with an external material would be beneficial. Thus, as a preliminary examination, the printed specimens were infiltrated with epoxy resin. The results showed that infiltration of the samples was successful, and the strength of the samples did increase, however, as expected, the specimens no longer failed in a brittle manner. It is recommended to investigate the infiltration of printed specimens with material such as cement or concrete to obtain samples that behave similar to rock.

Since the printed sand analogues were novel material that previously had not been tested in direct shear, the response of joint specimens in direct shear was explored. This was accomplished by printing rock joints with simple geometry and testing them in the direct shear apparatus under constant normal load (CNL) conditions. The printing procedure was the same as the procedure used to print intact rocks. Results showed that for triangular joints under the same applied normal stress, as expected, with the decrease of asperity angle from 45^{o} to 15^{o}, the dilation magnitude and the peak shear stress decreased. Also, by applying a higher normal stress - 0.5MPa compared to 0.125 MPa- the peak shear stress increased. The post peak response changed from brittle for the 45^{o} asperity to a more ductile response for the 15^{o} asperity, displaying different failure mechanisms. In addition, three standard roughness profiles with JRC=6-8, JRC=12-14 and JRC=18-20 were sheared under applied normal stresses ranging from 0.25 MPa to 1 MPa. Results indicated that, for a similar applied normal stress, there is a positive correlation between roughness (JRC value) and peak shear strength and dilation. Also, for each standard profile, shear displacement at peak shear stress increased for higher applied normal stresses. Moreover, the post peak response became more brittle for rougher joint surfaces. The peak shear stresses were compared with the Barton-Bandis shear model and in general, the peak shear stresses of the sand

proxies agreed with the model. From the results obtained in this section, it was demonstrated that joint surfaces printed with the binder jetting process and heat-cured can be successfully used to represent natural rock-like joint surfaces in direct shear.

For completeness, the use of 3D printing in combination with conventional methods of replicating rock was studied briefly. Molds of a rock joint surface with JRC=18-20 were printed with a printer that incorporated the FDM method, and it was observed that printing with a flexible filament resulted in a mold that was suitable for casting gypsum cement. To the best of the author's knowledge, flexible 3D printed molds have not been used to replicate rock joints prior to this study.

The verified procedure to print rock joints was then used to investigate the geometrical components that contribute to surface roughness anisotropy. This was done with a focus on two methods that are frequently adopted to quantify surface roughness, i.e., statistical parameters and the standard JRC. For this purpose, first, several simple geometries were chosen (i.e., seven triangular-tooth profiles) that differed from one another in shape, height and directionality of joint asperities and therefore could be evaluated based on their different statistical parameters. Direct shear tests were carried out in CNL conditions under 0.25 MPa applied normal stress and in CNS conditions with normal stiffness of 5 kN/mm. The software of the direct shear apparatus was modified to accommodate for CNS conditions. For one of the joint profiles (profile 1), additional tests were run which included CNL tests under 0.5 MPa and 1 MPa applied normal stress also a CNS test under k=10 kN/mm. Results revealed that in CNS conditions, all profiles exhibited a clear peak shear stress and post peak softening happened at a higher rate compared to CNL conditions. The shear strength increased significantly due to the constrained dilation and increased normal load applied to the asperities. The difference between the peak shear strength in CNL and CNS conditions was maximum for profile 2 (670% increase) and minimum for profile 5 (165% increase), because in profile 2 sliding was the main shearing mechanism and in profile 5,

shearing off of the asperities was the main mechanism. Considering the dilation rate of the profiles, it was shown that in CNL conditions, the dilation closely followed the slope of the asperities. The stress paths in CNS revealed that the normal stress continued to increase even after the joints had reached peak shear strength. The reason was localized damage at failure. For profile 1, the peak shear strengths followed Patton's shear strength model for sliding in CNL conditions. The pre-peak CNS stress paths followed the CNL failure envelope up to approximately 1.2 MPa normal stress (for k=5 kN/mm) and up to approximately 1.9 MPa normal stress (for k=10 kN/mm), affirming that up to these stresses, the dominant shear mechanism was sliding. After that they diverged. Analyzing the shear behaviour of the triangular profiles with respect to statistical parameters demonstrated that based solely on one statistical parameter, a clear correlation between that parameter and peak shear strength didn't exist. It was concluded that even though statistical parameters are good indicators for defining the anisotropy in roughness of the profiles, they are not adequate. Other factors such as contact area and edge effects that results in local stress concentrations play an important role in predicting the shear response of joints.

Next, to further understand the contributions of geometrical components on the shear response of joints, a novel approach was taken by constructing new fracture geometries. For this, two standard profiles with JRC=6-8 and JRC=18-20 -to demonstrate smoother and rougher joints of the spectrum- were chosen. The joint with JRC=6-8 was divided into 5 segments and the one with JRC=18-20 was divided into 5 and 10 segments. Then the segments were rearranged to make newly configured joint geometries (NCJs). The NCJs were tested in direct shear under CNL and CNS conditions and compared with the original joints. Results revealed that when the profile with JRC=18-20 was rearranged, the new profiles had more significant difference in terms of geometric properties compared with the original profile and thus their shear response, especially in CNS conditions differed from the original joint. This was not the case for the profile with JRC=6-8 and therefore the stress-displacement and dilation – displacement results for the NCJ-4 profiles in

both CNS and CNL conditions were not significantly different to the original profile. Furthermore, although the λ statistical parameter which considers both directional slope and height is better for describing the roughness surfaces, however factors such as the placement of the critical asperity (asperity with the highest inclinations) was observed to significantly affect the shear strength of joints such that profiles NCJ-10-1 and NCJ-10-4 where the critical asperity was located at the ends of the profiles and the normal stress was localized on these asperities, had lower dilation and shear strength than predicted. Consequently, it was concluded that the empirical method of JRC may be adequate for determining the joint roughness of smoother joints, however for rougher joints, other factors such as distribution of stress on the asperities are essential and should be considered.

Lastly, to obtain a better understanding of the limitations of the DEM approach using the PFC program for modelling direct shear tests, joints with JRC=6-8, JRC=12-14 and JRC=18-20 in CNL conditions under applied normal stresses ranging from 0.25 MPa to 1 MPa were simulated, and the results were compared with laboratory tests from previous sections. Intact material was generated and calibrated given the current state of practice, which is obtaining the macro behaviour of the rock analogue by iterating the micro-properties, then the joints were incorporated into the model using smooth-joint contacts. To implement the smooth-joints, the balls that were located on the upper joint plane were put into one group and the particles that were generated on the bottom joint plane were confined to another group. Then the model was programmed to insert a smooth-joint contact whenever the balls from the two groups came into contact. Results showed that the simulations captured the trend of shear stress vs. shear displacement and dilation vs. shear displacement behavior of laboratory tests, however there were some discrepancies. For example, for most simulated tests the peak shear stress was underestimated. These discrepancies may be because: the layered anisotropy of the printed specimens was not considered in the material genesis; parallel bonds were used for the intact material that overestimated the tensile strength; the inability of the specimen to tilt during shear;

the way the smooth-joints were implemented led to misalignment of joint sections. These findings will aid in future direct shear simulations where the micro-properties of the particles and bonds are directly inserted into PFC from printed specimen properties.

For future research, the following is recommended:

- Increase the compressive strength of the printed specimen to represent hard rock. Also, improve their modulus and strength ratios. Some options include altering the printing technique to lower the porosity of the samples or infiltrating the specimens with cement-like material.
- Study the shear response of incipient joints and the effect of joint matching coefficient on shear strength and dilation. This is feasible due to the ability of 3D printers in creating complex geometries rapidly.
- Consider scale effects especially in CNS conditions. With the advent of AM technology, it is possible to print larger joint geometries to study shear strength and deformation that is closer to field-scale behaviour.
- Develop a methodology to calibrate the simulated material fully. Some possible methods to achieve this include entering the micro-properties of the printed samples directly, calibrating the macro-properties for a wider range of strength and deformation properties and incorporating the anisotropy of the specimens in the model. Also, an investigation into the implementation of smooth-joints and the disproportionate effect they have on shear strength and deformation of the simulations is granted.

References

Amontons, G. (1699). De la resistance causee dans les machines. *Memoires de l'Academie Royale A*, 257–282.

Archambault, G., Gentier, S., Riss, J., & Flamand, R. (1997). The evolution of void spaces (permeability) in relation with rock joint shear behavior. *International Journal of Rock Mechanics and Mining Sciences*, *34*(3), paper No.014.

Ardila, N. (2018). *Hydraulic properties characterization of 3D printed sandstone analogues*. MSc. thesis, University of Alberta, Edmonton, Canada.

Asadi, M. S., Rasouli, V., & Barla, G. (2013). A laboratory shear cell used for simulation of shear strength and asperity degradation of rough rock fractures. *Rock Mechanics and Rock Engineering*, *46*(4), 683–699.

ASME B46.1. (2009). Surface Texture (Surface Roughness, Waviness, and Lay), ASME B46.1-2009 (Revision of ASME B46.1-2002). American Society of Mechanical Engineers.

ASTM F2792 - 12a. (2012). Standard Terminology for Additive Manufacturing Technologies. ASTM F2792-12a, West Conshohocken, PA, United States.

Bahaaddini, M., Hagan, P. C., Mitra, R., & Hebblewhite, B. K. (2015). Parametric study of smooth joint parameters on the shear behaviour of rock joints. *Rock Mechanics and Rock Engineering*, *48*(3), 923–940.

Bahaaddini, M., Hagan, P. C., Mitra, R., & Khosravi, M. H. (2016). Experimental and numerical study of asperity degradation in the direct shear test. *Engineering Geology*, *204*, 41–52.

Bahaaddini, M., Sharrock, G., & Hebblewhite, B. K. (2013). Numerical direct shear tests to model

the shear behaviour of rock joints. *Computers and Geotechnics*, *51*, 101–115.

Bandis, S. (1980). Experimental studies of scale effects on shear strength, and deformation of rock joints. PhD thesis. University of Leeds.

Barton, N., & Bandis, S. (1990). Review of predictive capabilities of JRC-JCS model in engineering practice. In N. Barton & O. Stephenson (Eds.), *Rock Joints, Proceedings of the International Symposium on Rock Joints* (pp. 603–610). Loen, Norway: Rotterdam: Balkema.

Barton, N., & Choubey, V. (1977). The shear strength of rock joints in theory and practice. *Rock Mechanics*, *10*(1–2), 1–54.

Barton, Nicholas. (1973). Review of a new shear-strength criterion for rock joints. *Engineering Geology*, *7*(4), 287–332.

Bayona, F. R., Stigsson, M., Johansson, F., & Ivars, D. M. (2018). Comparison between shear strength based on Barton's roughness profiles and equivalent synthetic profiles based on fractal theory. In *52nd US Rock Mechanics/Geomechanics Symposium*. American Rock Mechanics Association.

Beer, A. J., Stead, D., & Coggan, J. S. (2002). Estimation of the joint roughness coefficient (JRC) by visual comparison. *Rock Mechanics and Rock Engineering*, *35*(1), 65–74.

Benmokrane, B., & Ballivy, G. (1989). Laboratory study of shear behaviour of rock joints under constant normal stiffness conditions. In *The 30th US Symposium on Rock Mechanics (USRMS)*. American Rock Mechanics Association.

Berman, B. (2012). 3-D printing: The new industrial revolution. *Business Horizons*, *55*(2), 155–162.

Bewick, R P, Kaiser, P. K., & Bawden, W. F. (2014). DEM simulation of direct shear: 2. Grain

boundary and mineral grain strength component influence on shear rupture. *Rock Mechanics and Rock Engineering*, *47*(5), 1673–1692.

Bewick, R P, Kaiser, P. K., Bawden, W. F., & Bahrani, N. (2014). DEM simulation of direct shear: 1. Rupture under constant normal stress boundary conditions. *Rock Mechanics and Rock Engineering*, *47*(5), 1647–1671.

Bewick, Robert P. (2013). Shear rupture of massive brittle rock under constant normal stress and stiffness boundary conditions. University of Toronto, Toronto, Canada.

Brady, B. H. G., & Brown, E. T. (2013). *Rock mechanics: for underground mining*. Springer Science & Business Media.

Chen, Y., Zhou, C., & Lao, J. (2011). A layerless additive manufacturing process based on CNC accumulation. *Rapid Prototyping Journal*, *17*(3), 218–227.

Cho, N. (2008). *Discrete element modeling of rock pre-peak fracturing and dilation*. PhD thesis, University of Alberta, Edmonton, Canada.

Cundall, P. A. (2000). Numerical experiments on rough joints in shear using a bonded particle model. In F. K. Lehner & J. L. Urai (Eds.), *Aspects of tectonic faulting* (pp. 1–9). Springer, Berlin.

Deere, D. U., & Miller, R. P. (1966). *Engineering classification and index properties for intact rock*. Technical Report AFWL-TR-65-116. U.S. Air Force Weapons Laboratory. Kirtland Air Force Base, New Mexico.

El-Soudani, S. M. (1978). Profilometric analysis of fractures. *Metallography*, *11*(3), 247–336.

Fardin, N., Stephansson, O., & Jing, L. (2001). The scale dependence of rock joint surface roughness. *International Journal of Rock Mechanics and Mining Sciences*, *38*(5), 659–669.

Gao, W., Zhang, Y., Ramanujan, D., Ramani, K., Chen, Y., Williams, C. B., … Zavattieri, P. D. (2015). The status, challenges, and future of additive manufacturing in engineering. *Computer-Aided Design*, *69*, 65–89.

Gentier, S., Riss, J., Archambault, G., Flamand, R., & Hopkins, D. (2000). Influence of fracture geometry on shear behavior. *International Journal of Rock Mechanics and Mining Sciences*, *37*(1–2), 161–174.

Gomez, J. S. (2017). *Mechanical Properties Characterization of 3D Printed Reservoir Sandstone Analogues*. MSc. thesis, University of Alberta, Edmonton, Canada.

Goodman, R. E., & John, C. St. (1977). Finite element analysis for discontinuous rock. In *Numerical Methods in Geotechnical Engineering*. New York: McGraw-Hill.

Grasselli, G., & Egger, P. (2003). Constitutive law for the shear strength of rock joints based on three-dimensional surface parameters. *International Journal of Rock Mechanics and Mining Sciences*, *40*(1), 25–40.

Grasselli, G., Wirth, J., & Egger, P. (2002). Quantitative three-dimensional description of a rough surface and parameter evolution with shearing. *International Journal of Rock Mechanics and Mining Sciences*, *39*(6), 789–800.

Hammah, R. E., Yacoub, T., Corkum, B., & Curran, J. H. (2008). The practical modelling of discontinuous rock masses with finite element analysis. In *The 42nd US Rock Mechanics Symposium (USRMS)*. San Francisco, USA: American Rock Mechanics Association.

Hanaor, D. A. H., Gan, Y., Revay, M., Airey, D. W., & Einav, I. (2016). 3D printable geomaterials. *Géotechnique*, *66*(4), 323–332.

Head, D., & Vanorio, T. (2016). Effects of changes in rock microstructures on permeability: 3-D

printing investigation. *Geophysical Research Letters*, *43*(14), 7494–7502.

Hencher, S. R., & Richards, L. R. (2015). Assessing the Shear Strength of Rock Discontinuities at Laboratory and Field Scales. *Rock Mechanics and Rock Engineering*, *48*(3), 883–905.

Heuze, F. E. (1979). Dilatant effects of rock joints. In *4th ISRM Congress* (pp. 169–175). International Society for Rock Mechanics and Rock Engineering.

Hodder, K. (2017). *Fabrication, Characterization and Performance of 3D-Printed Sandstone Models*. PhD thesis, University of Alberta, Edmonton, Canada.

Hodder, K. J., Nychka, J. A., & Chalaturnyk, R. J. (2018). Process limitations of 3D printing model rock. *Progress in Additive Manufacturing*, *3*(3), 173–182.

Hoek, E. (1983). Strength of jointed rock masses. *Geotechnique*, *33*(3), 187–223.

Hong, E., Lee, J., & Lee, I. (2008). Underestimation of roughness in rough rock joints. *International Journal for Numerical and Analytical Methods in Geomechanics*, *32*(11), 1385–1403.

Huang, T. H., Chang, C. S., & Chao, C. Y. (2002). Experimental and mathematical modeling for fracture of rock joint with regular asperities. *Engineering Fracture Mechanics*, *69*(17), 1977–1996.

Indraratna, B., & Haque, A. (2000). Experimental and numerical modeling of shear behaviour of rock joints. *GeoEng 2000, An International Conference on Geotechnical & Geological Engineering*, Pennsylvania, USA.

Indraratna, B., Haque, A., & Aziz, N. (1998). Laboratory modelling of shear behaviour of soft joints under constant normal stiffness conditions. *Geotechnical & Geological Engineering*, *16*(1), 17–44.

Indraratna, B., Haque, A., & Aziz, N. (1999). Shear behaviour of idealized infilled joints under constant normal stiffness. *Geotechnique*, *49*(3), 331–355.

Indraratna, B., Oliveira, D. A. F., Brown, E. T., & De Assis, A. P. (2010). Effect of soil–infilled joints on the stability of rock wedges formed in a tunnel roof. *International Journal of Rock Mechanics and Mining Sciences*, *47*(5), 739–751.

Indraratna, B., Thirukumaran, S., Brown, E. T., & Zhu, S. P. (2015). Modelling the shear behaviour of rock joints with asperity damage under constant normal stiffness. *Rock Mechanics and Rock Engineering*, *48*(1), 179–195.

Ishutov, S., & Hasiuk, F. J. (2017). 3D printing Berea sandstone: testing a new tool for petrophysical analysis of reservoirs. *Petrophysics*, *58*(06), 592–602.

Ishutov, S., Jobe, T. D., Zhang, S., Gonzalez, M., Agar, S. M., Hasiuk, F. J., … Chalaturnyk, R. (2018). Three-dimensional printing for geoscience: Fundamental research, education, and applications for the petroleum industry. *AAPG Bulletin*, *102*(1), 1–26.

ISRM. (1978). International Society for Rock Mechanics commission on standardization of laboratory and field tests: Suggested methods for determining tensile strength of rock materials. *International Journal of Rock Mechanics and Mining Sciences & Geomechanics Abstracts*, *15*, 99–103.

Itasca. (2008). *Itasca Consulting Group Inc. PFC2D Particle Flow Code in 2 Dimensions. Online manual*. Minniapolis, Minnesota.

Jiang, C., & Zhao, G.-F. (2015). A preliminary study of 3D printing on rock mechanics. *Rock Mechanics and Rock Engineering*, *48*(3), 1041–1050.

Jiang, Q., Feng, X., Song, L., Gong, Y., Zheng, H., & Cui, J. (2016). Modeling rock specimens

through 3D printing: Tentative experiments and prospects. *Acta Mechanica Sinica*, *32*(1), 101–111.

Jiang, Y., Li, B., & Tanabashi, Y. (2006). Estimating the relation between surface roughness and mechanical properties of rock joints. *International Journal of Rock Mechanics and Mining Sciences*, *43*(6), 837–846.

Jiang, Y., Tanabashi, Y., Nagaie, K., Li, B., & Xiao, J. (2004a). Relationship between surface fractal characteristic and hydro-mechanical behavior of rock joints. In Y. Ohnishi & K. Aoki (Eds.), *Proceedings of 3rd Asian Rock Mech. Symposium* (pp. 831–836).

Jiang, Y., Xiao, J., Tanabashi, Y., & Mizokami, T. (2004b). Development of an automated servo-controlled direct shear apparatus applying a constant normal stiffness condition. *International Journal of Rock Mechanics and Mining Sciences*, *41*(2), 275–286.

Jing, L., & Hudson, J. A. (2002). Numerical methods in rock mechanics. *International Journal of Rock Mechanics and Mining Sciences*, *39*(4), 409–427.

Johansson, F. (2016). Influence of scale and matedness on the peak shear strength of fresh, unweathered rock joints. *International Journal of Rock Mechanics and Mining Sciences*, *82*, 36–47.

Kodikara, J. K., & Johnston, I. W. (1994). Shear behaviour of irregular triangular rock-concrete joints. *International Journal of Rock Mechanics and Mining Sciences & Geomechanics Abstracts*, *31*(4), 313–322.

Ladanyi, B., & Archambault, G. (1969). Simulation of shear behavior of a jointed rock mass. In *The 11th US Symposium on Rock Mechanics (USRMS)*. American Rock Mechanics Association.

Lambert, C., & Coll, C. (2014). Discrete modeling of rock joints with a smooth-joint contact model. *Journal of Rock Mechanics and Geotechnical Engineering*, *6*(1), 1–12.

Lazzari, E., Johansson, F., Mas Ivars, D., & Sánchez Juncal, A. (2014). Advances, current limitations and future requirements for a numerical shear box for rock joints using PFC 2D. In *EUROCK 2014, ISRM European Regional Symposium – in Rock Engineering and Rock Mechanics: Structures in and on Rock Masses* (pp. 763–768).

Leichnitz, W. (1985). Mechanical properties of rock joints. *International Journal of Rock Mechanics and Mining Sciences & Geomechanics Abstracts*, *22*(5), 313–321.

Li, Y., & Huang, R. (2015). Relationship between joint roughness coefficient and fractal dimension of rock fracture surfaces. *International Journal of Rock Mechanics and Mining Sciences*, *75*, 15–22.

Li, Y., Oh, J., Mitra, R., & Canbulat, I. (2017). A fractal model for the shear behaviour of large-scale opened rock joints. *Rock Mechanics and Rock Engineering*, *50*(1), 67–79.

Li, Y., Oh, J., Mitra, R., & Hebblewhite, B. (2016a). A constitutive model for a laboratory rock joint with multi-scale asperity degradation. *Computers and Geotechnics*, *72*, 143–151.

Li, Y., Oh, J., Mitra, R., & Hebblewhite, B. (2016b). Experimental studies on the mechanical behaviour of rock joints with various openings. *Rock Mechanics and Rock Engineering*, *49*(3), 837–853.

Li, Y., Wu, W., & Li, B. (2018). An analytical model for two-order asperity degradation of rock joints under constant normal stiffness conditions. *Rock Mechanics and Rock Engineering*, *51*(5), 1431–1445.

Li, Y., & Zhang, Y. (2015). Quantitative estimation of joint roughness coefficient using statistical

parameters. *International Journal of Rock Mechanics and Mining Sciences*, *100*(77), 27–35.

Lindenbach, E. J., & Bearce, R. G. (2018). Comparison of Results From CNS and CNL Testing on Simulated Rock and Concrete. In *52nd US Rock Mechanics/Geomechanics Symposium*. American Rock Mechanics Association.

Lisjak, A., & Grasselli, G. (2014). A review of discrete modeling techniques for fracturing processes in discontinuous rock masses. *Journal of Rock Mechanics and Geotechnical Engineering*, *6*(4), 301–314.

Liu, X. G., Zhu, W. C., Yu, Q. L., Chen, S. J., & Li, R. F. (2017). Estimation of the joint roughness coefficient of rock joints by consideration of two-order asperity and its application in double-joint shear tests. *Engineering Geology*, *220*, 243–255.

Maerz, N. H., Franklin, J. A., & Bennett, C. P. (1990). Joint roughness measurement using shadow profilometry. *International Journal of Rock Mechanics and Mining Sciences & Geomechanics Abstracts*, *27*(5), 329–343.

Maleksaeedi, S., Eng, H., Wiria, F. E., Ha, T. M. H., & He, Z. (2014). Property enhancement of 3D-printed alumina ceramics using vacuum infiltration. *Journal of Materials Processing Technology*, *214*(7), 1301–1306.

Mandelbrot, B. (1967). How long is the coast of Britain? Statistical self-similarity and fractional dimension. *Science*, *156*(3775), 636–638.

Mandelbrot, B. (1983). *The fractal geometry of nature* (Vol. 173). New York : W.H. Freeman.

Mandelbrot, B. (1985). Self-affine fractals and fractal dimension. *Physica Scripta*, *32*(4), 257–260.

McKillip, W. J. (1989). Chemistry of furan polymers. *Adhesives from Renewable Resources*, 408–423.

Mehranpour, M. H., & Kulatilake, P. H. S. W. (2017). Improvements for the smooth joint contact model of the particle flow code and its applications. *Computers and Geotechnics*, *87*, 163–177.

Menezes, P. L., Nosonovsky, M., Ingole, S. P., Kailas, S. V., & Lovell, M. R. (2013). *Tribology for scientists and engineers*. Springer.

Mouchaorab, K. S., & Benmokrane, B. (1994). A new combined servo-controlled loading frame/direct-shear apparatus for the study of concrete or rock joint behavior under different boundary and loading conditions. *Geotechnical Testing Journal*, *17*(2), 233–242.

Muralha, J., Grasselli, G., Tatone, B., Blümel, M., Chryssanthakis, P., & Yujing, J. (2014). ISRM suggested method for laboratory determination of the shear strength of rock joints: revised version. *Rock Mechanics and Rock Engineering*, *47*(1), 291–302.

Myers, N. O. (1962). Characterization of surface roughness. *Wear*, *5*(3), 182–189.

Oh, J., Cording, E. J., & Moon, T. (2015). A joint shear model incorporating small-scale and large-scale irregularities. *International Journal of Rock Mechanics and Mining Sciences*, *76*, 78–87.

Osinga, S., Zambrano-Narvaez, G., & Chalaturnyk, R. J. (2015). Study of geomechanical properties of 3D printed sandstone analogue. In *49th US Rock Mechanics/Geomechanics Symposium*. American Rock Mechanics Association.

Palmström, A. (2001). Measurement and characterization of rock mass jointing. In V. M. Sharma & K. R. Saxena (Eds.), *In-situ characterization of rocks* (pp. 49–97). Rotterdam: A. A.

Balkema.

Park, J.-W., & Song, J.-J. (2009). Numerical simulation of a direct shear test on a rock joint using a bonded-particle model. *International Journal of Rock Mechanics and Mining Sciences*, *46*(8), 1315–1328.

Patton, F. D. (1966). Multiple modes of shear failure in rock. In *1st ISRM Congress*. International Society for Rock Mechanics and Rock Engineering.

Perras, M. A., & Diederichs, M. S. (2014). A review of the tensile strength of rock: concepts and testing. *Geotechnical and Geological Engineering*, *32*(2), 525–546.

Perras, M. A., & Vogler, D. (2019). Compressive and Tensile Behavior of 3D-Printed and Natural Sandstones. *Transport in Porous Media*, *129*(2), 559–581.

Pierce, M., Mas Ivars, D., Cundall, P. A., & Potyondy, D. (2007). A synthetic rock mass model for jointed rock. In *Rock Mechanics: Meeting Society's Challenges and Demands, 1st Canada-US Rock Mechanics Symposium, Vancouver*.

Porcino, D., Fioravante, V., Ghionna, V. N., & Pedroni, S. (2003). Interface behavior of sands from constant normal stiffness direct shear tests. *Geotechnical Testing Journal*, *26*(3), 289–301.

Poturovic, S., Schubert, W., & Blümel, M. (2015). Comparison of constant normal load (CNL) and constant normal stiffness (CNS) direct shear tests. In *ISRM Regional Symposium-EUROCK 2015*. International Society for Rock Mechanics and Rock Engineering.

Potyondy, D.O., & Cundall, P. A. (2004). A bonded-particle model for rock. *International Journal of Rock Mechanics and Mining Sciences*, *41*(8), 1329–1364.

Potyondy, D. (2012). A flat-jointed bonded-particle material for hard rock. In *46th US rock mechanics/geomechanics symposium*. American Rock Mechanics Association.

Potyondy, D. (2015). Material-Modeling Support in PFC. In *Technical Memorandum ICG7766-L*. Minneapolis, MN: Itasca Consulting Group.

Primkulov, B., Chalaturnyk, J., Chalaturnyk, R., & Zambrano Narvaez, G. (2017). 3D printed sandstone strength: curing of furfuryl alcohol resin-based sandstones. *3D Printing and Additive Manufacturing*, *4*(3), 149–156.

Rasouli, V., & Harrison, J. P. (2010). Assessment of rock fracture surface roughness using Riemannian statistics of linear profiles. *International Journal of Rock Mechanics and Mining Sciences*, *47*(6), 940–948.

Rim, H. R., Choi, H. J., Son, B.-K., Lee, C.-I., & Song, J.-J. (2005). Experimental study for shear behaviour of pseudo rock joint under constant normal stiffness condition. In *Proceedings of the 31st ITA-AITES world tunnel congress on underground space use, Istanbul* (pp. 175–181).

Saeb, S., & Amadei, B. (1990). Modelling joint response under constant or variable normal stiffness boundary conditions. *International Journal of Rock Mechanics and Mining Sciences & Geomechanics Abstracts*, *27*(3), 213–217.

Saeb, S., & Amadei, B. (1992). Modelling rock joints under shear and normal loading. *International Journal of Rock Mechanics and Mining Sciences & Geomechanics Abstracts*, *29*(3), 267–278.

Scholz, C. H. (2002). *The mechanics of earthquakes and faulting*. Cambridge university press.

Seidel, J. P., & Haberfield, C. M. (1995). Towards an understanding of joint roughness. *Rock Mechanics and Rock Engineering*, *28*(2), 69–92.

Seidel, J. P., & Haberfield, C. M. (2002). Laboratory testing of concrete-rock joints in constant

normal stiffness direct shear. *Geotechnical Testing Journal*, *25*(4), 391–404.

Shang, J., Zhao, Z., & Ma, S. (2018). On the shear failure of incipient rock discontinuities under CNL and CNS boundary conditions: insights from DEM modelling. *Engineering Geology*, *234*, 153–166.

Skinas, C. A., Bandis, S. C., & Demiris, C. A. (1990). Experimental investigations and modelling of rock joint behaviour under constant stiffness. In *Proceedings of the International Conference on Rock Joints. Loen, Norway* (pp. 301–308).

Suzuki, A., Watanabe, N., Li, K., & Horne, R. N. (2017). Fracture network created by 3-D printer and its validation using CT images. *Water Resources Research*, *53*(7), 6330–6339.

Tatone, B. S. A. (2009). Quantitative characterization of natural rock discontinuity roughness in-situ and in the laboratory: MASc. thesis, University of Toronto, Toronto, Canada.

Tatone, B. S. A. (2014). Investigating the evolution of rock discontinuity asperity degradation and void space morphology under direct shear. PhD thesis, University of Toronto, Toronto, Canada.

Tatone, B. S. A., & Grasselli, G. (2010). A new 2D discontinuity roughness parameter and its correlation with JRC. *International Journal of Rock Mechanics and Mining Sciences*, *47*(8), 1391–1400.

Tatone, B. S. A., & Grasselli, G. (2012). Modeling direct shear tests with FEM/DEM: Investigation of discontinuity shear strength scale effect as an emergent characteristic. In *46th US Rock Mechanics/Geomechanics Symposium*. American Rock Mechanics Association.

Thirukumaran, S., & Indraratna, B. (2016). A review of shear strength models for rock joints subjected to constant normal stiffness. *Journal of Rock Mechanics and Geotechnical*

Engineering, *8*(3), 405–414.

Tian, Y., Liu, Q., Liu, D., Kang, Y., Deng, P., & He, F. (2018). Updates to Grasselli's Peak Shear Strength Model. *Rock Mechanics and Rock Engineering*, *51*(7), 2115–2133.

Tse, R., & Cruden, D. M. (1979). Estimating joint roughness coefficients. *International Journal of Rock Mechanics and Mining Sciences & Geomechanics Abstracts*, *16*(5), 303–307.

Ueng, T.-S., Jou, Y.-J., & Peng, I.-H. (2010). Scale effect on shear strength of computer-aided-manufactured joints. *Journal of GeoEngineering*, *5*(2), 29–37.

Wang, G., Zhang, X. P., Jiang, Y. J., Li, B., Wu, X. Z., & Huang, N. (2015). Meso-mechanism research on shear failure of rock joint based on particle discrete element method. *Journal of Central South University*, *46*(4), 1442–1453.

Wang, S., Guo, M., Sun, G., & Liu, S. (2018). Modeling the shear behavior of rock joints under various normal conditions. GeoEdmonton 2018, Edmonton, Canada.

Xia, C.-C., Tang, Z.-C., Xiao, W.-M., & Song, Y.-L. (2014). New peak shear strength criterion of rock joints based on quantified surface description. *Rock Mechanics and Rock Engineering*, *47*(2), 387–400.

Yang, J., Rong, G., Hou, D., Peng, J., & Zhou, C. (2016). Experimental study on peak shear strength criterion for rock joints. *Rock Mechanics and Rock Engineering*, *49*(3), 821–835.

Yang, Z.-Y., Taghichian, A., & Li, W.-C. (2010). Effect of asperity order on the shear response of three-dimensional joints by focusing on damage area. *International Journal of Rock Mechanics and Mining Sciences*, *6*(47), 1012–1026.

Yang, Z. Y., Lo, S. C., & Di, C. C. (2001). Reassessing the joint roughness coefficient (JRC) estimation using Z2. *Rock Mechanics and Rock Engineering*, *34*(3), 243–251.

Yu, X., & Vayssade, B. (1991). Joint profiles and their roughness parameters. *International Journal of Rock Mechanics and Mining Sciences & Geomechanics Abstracts*, *28*(4), 333–336.

Zhang, G., Karakus, M., Tang, H., Ge, Y., & Zhang, L. (2014). A new method estimating the 2D joint roughness coefficient for discontinuity surfaces in rock masses. *International Journal of Rock Mechanics and Mining Sciences*, *72*, 191–198.

Zhao, J. (1997). Joint surface matching and shear strength part A: joint matching coefficient (JMC). *International Journal of Rock Mechanics and Mining Sciences*, *34*(2), 173–178.

Zhou, T., & Zhu, J. B. (2018). Identification of a suitable 3D printing material for mimicking brittle and hard rocks and its brittleness enhancements. *Rock Mechanics and Rock Engineering*, *51*(3), 765–777.

Zhu, J. B., Zhou, T., Liao, Z. Y., Sun, L., Li, X. B., & Chen, R. (2018). Replication of internal defects and investigation of mechanical and fracture behaviour of rock using 3D printing and 3D numerical methods in combination with X-ray computerized tomography. *International Journal of Rock Mechanics and Mining Sciences*, *106*, 198–212.

Zongqi, S., & Ming, X. F. (1990). Study of rock joint surface feature and it's classification. In N. Barton & O. Stephansson (Eds.), *Rock Joints: Proceedings of the international symposium on rock joints* (pp. 101–107). Rotterdam: A. A. Balkema.

Appendix

This appendix contains images of the failed specimens for the New Configured Joint (NCJ) profiles corresponding to Chapter 4.

a.

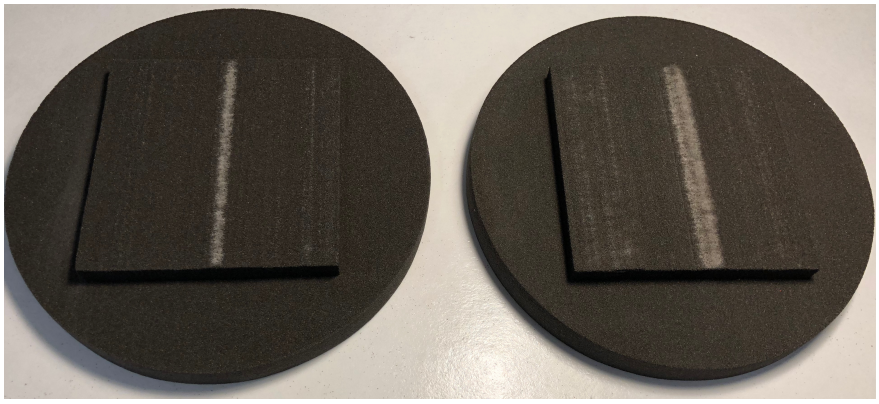

b.

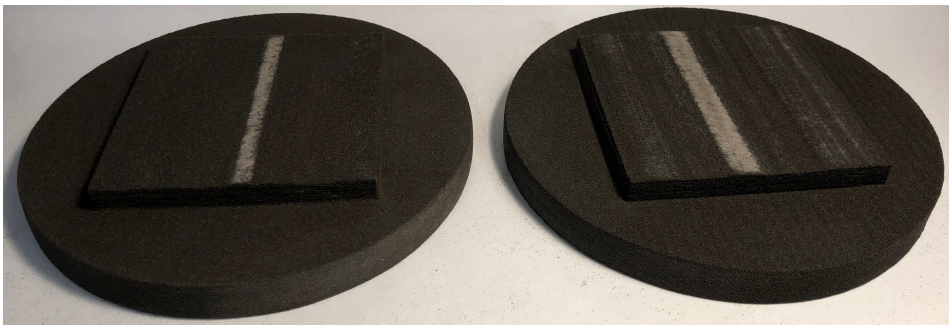

Figure A.1. Failure patterns after shear in NCJ-4-1: a. CNL conditions b. CNS conditions.

a.

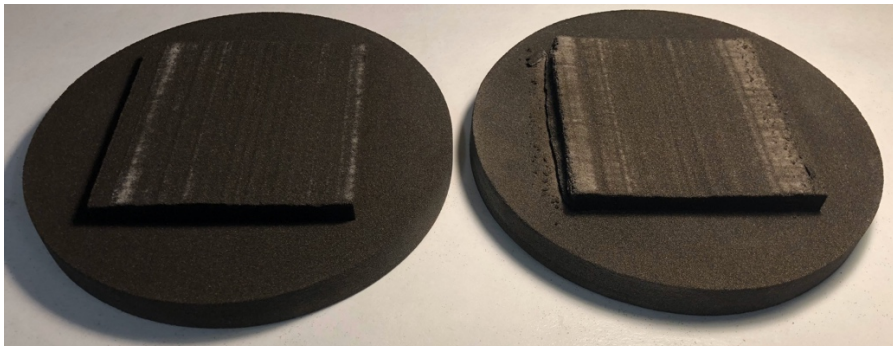

b.

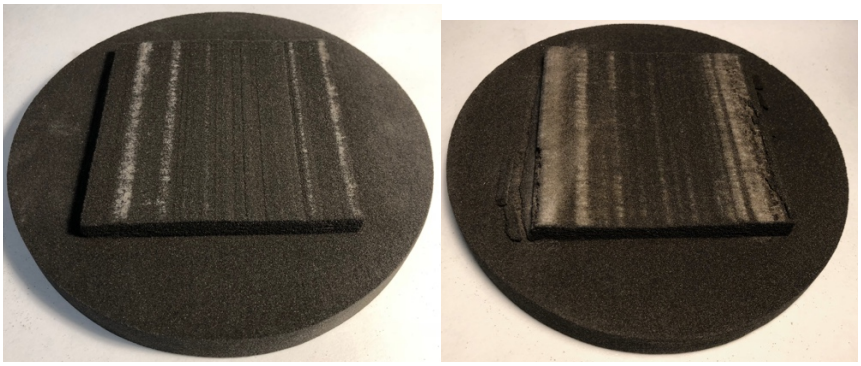

Figure A.2. Failure patterns after shear in NCJ-4-2: a. CNL conditions b. CNS conditions.

a.

b.

Figure A.3. Failure patterns after shear in NCJ-4-3: a. CNL conditions b. CNS conditions.

a.

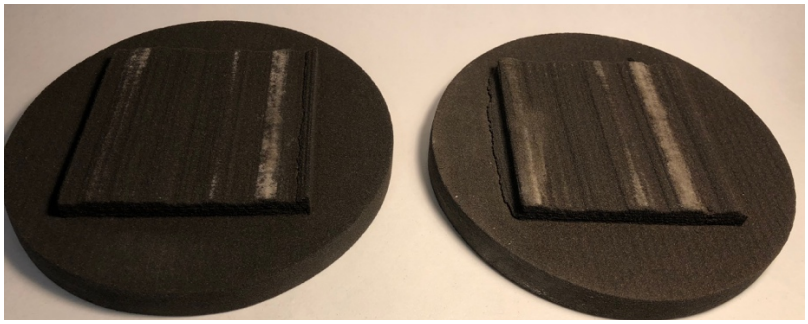

b.

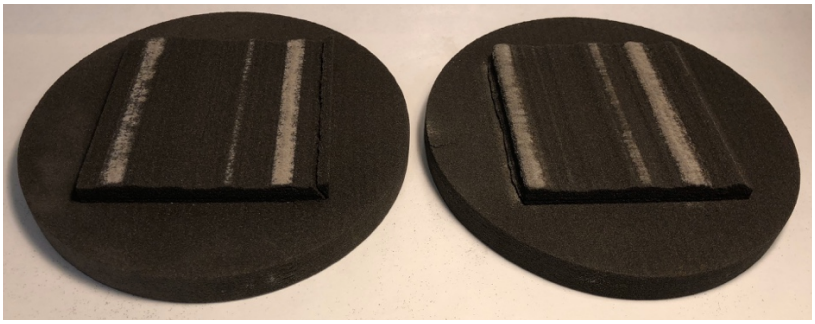

Figure A.4. Failure patterns after shear in NCJ-10-1: a. CNL conditions b. CNS conditions.

a.

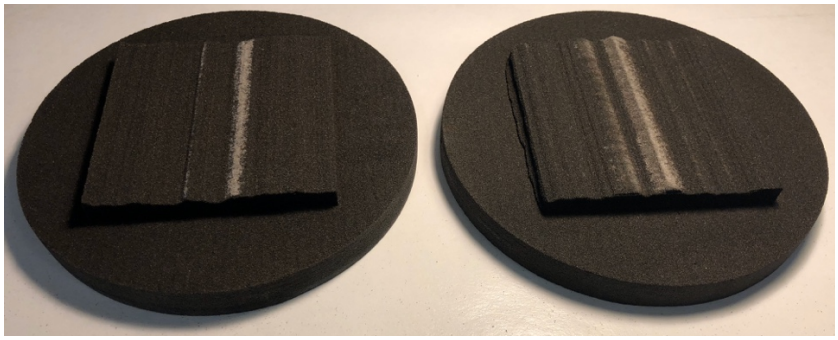

b.

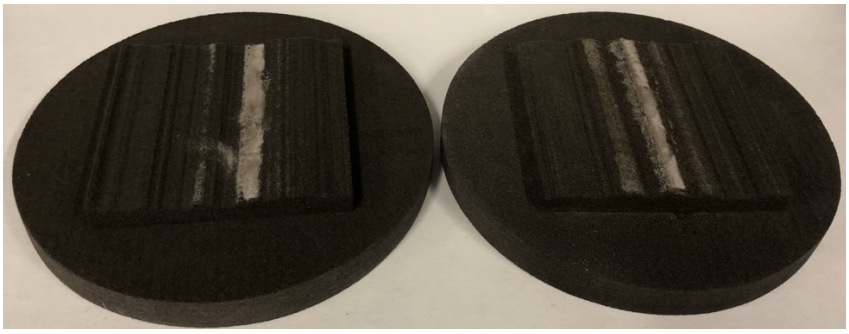

Figure A.5. Failure patterns after shear in NCJ-10-2: a. CNL conditions b. CNS conditions.

a.

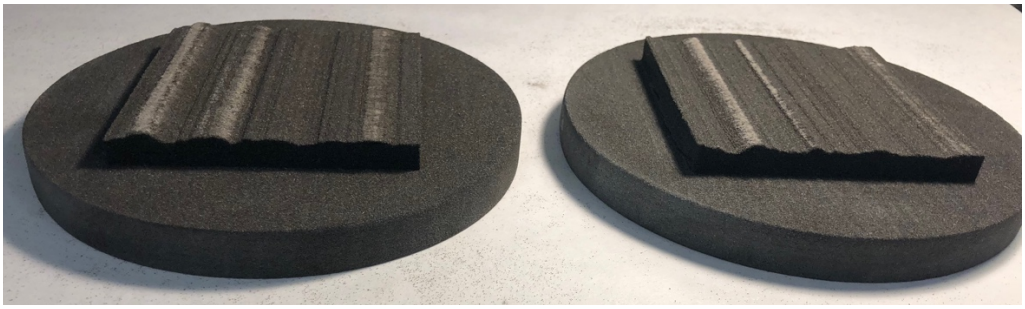

b.

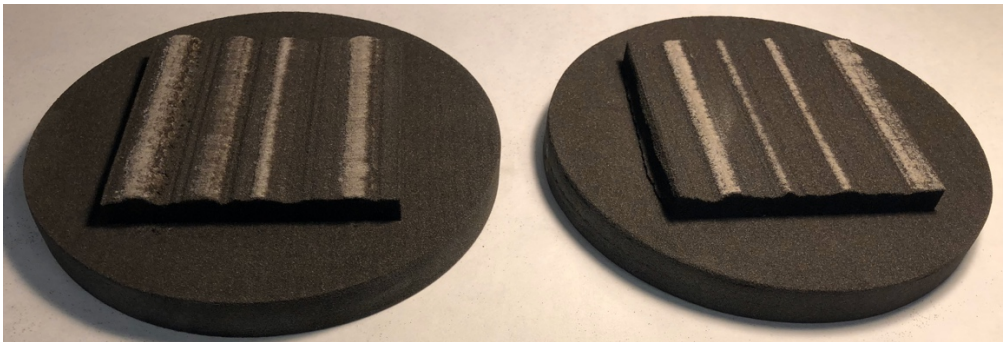

Figure A.6. Failure patterns after shear in NCJ-10-3: a. CNL conditions b. CNS conditions.

a.

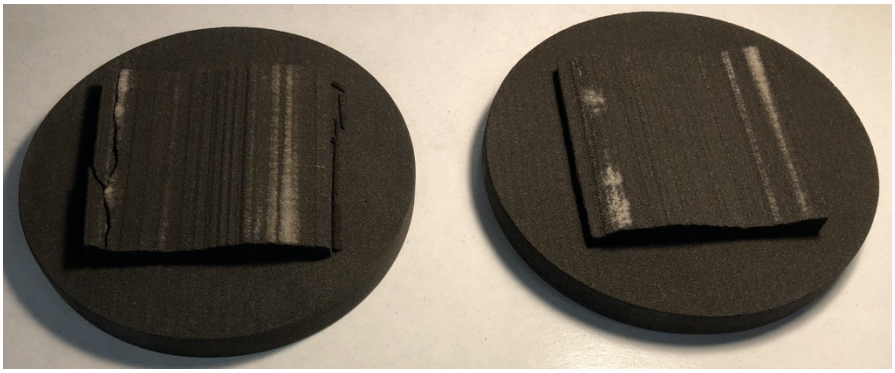

b.

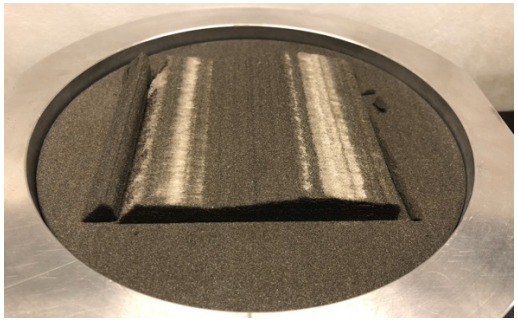

Figure A.7. Failure patterns after shear in NCJ-10-4: a. CNL conditions b. CNS conditions.

a.

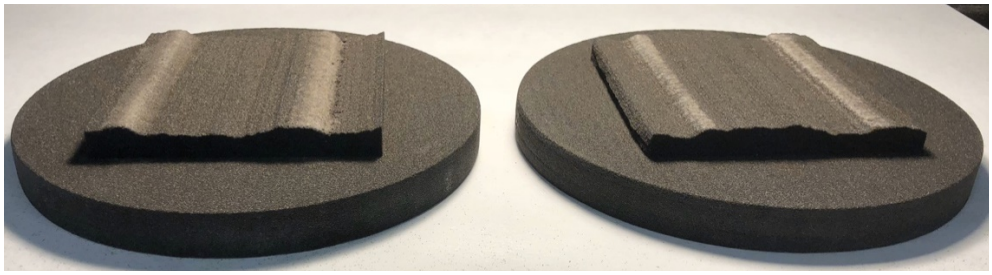

b.

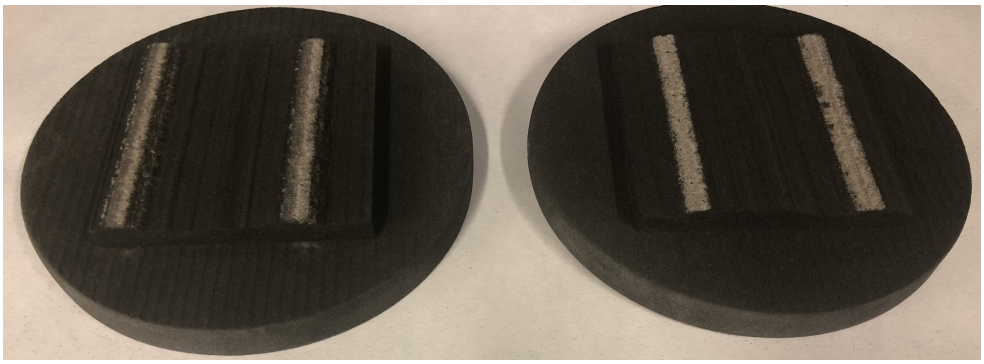

Figure A.8. Failure patterns after shear in NCJ-10-5: a. CNL conditions b. CNS conditions.

a.

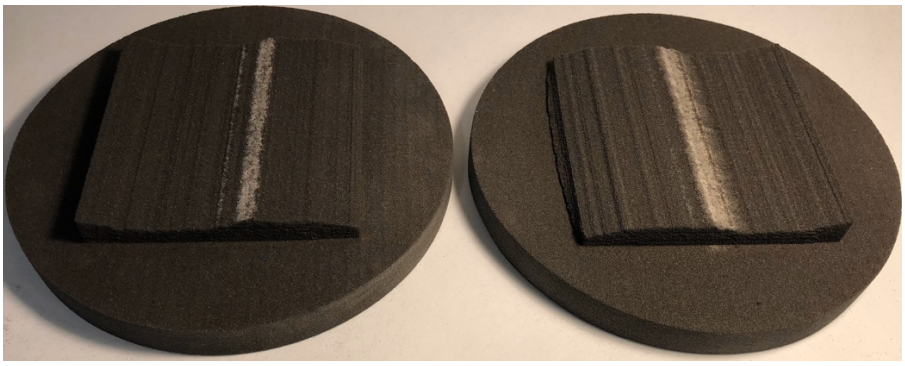

b.

Figure A.9. Failure patterns after shear in NCJ-10-6: a. CNL conditions b. CNS conditions.